UNIVERSITY OF SOUTHAMPTON

FACULTY OF NATURAL AND ENVIRONMENTAL SCIENCES

OCEAN AND EARTH SCIENCES

Global Seismic Imaging of Lithospheric Discontinuities using SS Precursors

By

Saikiran Tharimena

April 2017

Thesis for the degree of Doctor of Philosophy

Nothing is so dangerous to the progress of the human mind than to assume that our views of science are ultimate; that there are no mysteries in nature; that our triumphs are complete, and that there are no new worlds to conquer.

– Sir Humphry Davy

I lovingly dedicate this thesis to my parents, Sunder and Anuradha.
Their sacrifice, support, encouragement, and constant love have
sustained me throughout my life.

ABSTRACT

Global Seismic Imaging of Lithospheric Discontinuities Using SS Precursors

by

Saikiran Tharimena

Seismic imaging of the lithospheric discontinuities, primarily the base of the lithosphere can provide valuable constraints on the nature of the lithosphere–asthenosphere system, which is vital to our understanding of plate tectonics and mantle dynamics. However, self-consistently imaging, characterizing and relating the lithospheric discontinuities beneath different tectonic environments has been challenging. Understanding the characteristics and defining mechanism(s) of the lithospheric discontinuities can shed light on the formation mechanism and possibly the origin of these discontinuities. This study focuses on seismically imaging the discontinuity structure using SS precursors beneath three unique tectonic environments; the Ontong Java Plateau (OJP), the Pacific Ocean and the continents. SS precursors resolve discontinuities at 28 ± 4 km, consistent with a Moho, a mid-lithospheric discontinuity (MLD) at 80 ± 5 km, and a deeper negative discontinuity at 282 ± 7 km depth beneath the Ontong Java Plateau. The Pacific Ocean is characterized by a sharp, pervasive velocity discontinuity at 30 – 80 km depth with a 3 – 15% shear velocity drop over < 21 km depth. The discontinuity increases in depth with age from the ridge to 36 ± 9 My along the 1100 °C conductive cooling isotherm. Beneath older seafloor, the discontinuity is at a mean depth of 60 ± 1.5 km. Finally, SS precursors resolve a discontinuity at 80 – 121 km depth beneath some continents, consistent with observations of an MLD. In addition, all continental interiors, except India, are characterized by a sharp discontinuity at 130 – 190 km depth, well–correlated with the depth extent of the lithosphere from diamond thermobarometry and also the transition from coarse-to-deformed xenolith textures. The amplitude and sharpness of the discontinuities imaged beneath the OJP, the Pacific Ocean and the continents suggest that causative mechanisms such as composition, anisotropy and/or melt may be required along with temperature to explain their origin.

Page intentionally left blank.

Contents

Abstract -- v
Contents --- vii
List of Figures -- xi
List of Tables --- xxv
Declaration of Authorship --- xxvii
Acknowledgements --- xxix

1. **Chapter 1: Introduction** -- 1
    1.1. Background -- 1
    1.2. Oceanic and Continental Lithosphere ---------------------------- 2
        1.2.1. The Seismic Lithosphere ------------------------------------ 8
    1.3. Outline of Data and Methods --------------------------------------- 12
        1.3.1. The Data --- 12
        1.3.2. SS Precursors -- 14
    1.4. Outline of Thesis -- 20
    1.5. Candidate's Contribution --- 21
2. **Chapter 2: Imaging the Ontong Java Plateau** ---------------------- 23
    2.1. Abstract --- 25
    2.2. Introduction --- 26
    2.3. Methods --- 29
        2.3.1. Stacking --- 30
        2.3.2. Discontinuity Modeling -------------------------------------- 30
        2.3.3. Thermal Modeling --- 35
        2.3.4. Fresnel Zone Testing -- 36
        2.3.5. Moveout Testing -- 38
    2.4. Results -- 38

2.5. Discussion -- 40
2.5.1. Anisotropy --- 43
2.5.2. Active Tectonics -- 44
2.5.3. Elastically Accommodated Grain Boundary Sliding (EAGBS) -- 45
2.5.4. Compositional Origin, Possibly in a Viscous Root ------ 46
2.6. Conclusions --- 49
3. Chapter 3: Imaging the Pacific Lithosphere ------------------------ 51
3.1. Abstract -- 53
3.2. Introduction --- 54
3.3. Methods -- 57
3.3.1. Data and Stacking --- 59
3.3.2. Pacific Binning -- 61
3.3.3. Pacific Bin Attributes -- 62
3.3.4. Reference Phase --- 62
3.3.5. Modeling --- 64
3.3.5.1. Optimization -- 66
3.4. Results -- 70
3.4.1. Shallow, Positive Discontinuity ---------------------------- 72
3.4.2. Pervasive Negative Discontinuity -------------------------- 75
3.4.3. Resolution of the Shape of the Velocity Discontinuity - 81
3.4.4. No Discontinuity and Failed Bins ------------------------- 86
3.5. Discussion -- 88
3.5.1. Shallow, Positive Discontinuity ---------------------------- 88
3.5.2. Pervasive Negative Discontinuity -------------------------- 90
3.5.2.1. Comparison to Previous Studies ------------------- 90
3.5.2.2. Comparison to Previous Transects Studies ------- 94
3.5.2.3. Comparison to a Thermal Model ------------------ 97

3.5.2.4. Causative Processes for the Shallow, Pervasive Negative Discontinuity ---------------------------------- 99
3.6. Conclusions -- 103
4. Chapter 4: Imaging the Cratons --------------------------------------- 105
4.1. Abstract -- 107
4.2. Introduction -- 108
4.3. Data and Methods -- 112
4.3.1. SS Precursor Modeling --------------------------------------- 113
4.3.2. Error Analysis -- 116
4.4. Results --- 116
4.4.1. Shape of the Velocity Gradient ------------------------------ 121
4.5. Comparison to Previous Results ------------------------------------ 123
4.5.1. The Moho --- 123
4.5.2. Shallow Negative Discontinuity (80 – 121 km) ---------- 124
4.5.3. Deep Negative Discontinuity (> 130 km) ----------------- 126
4.6. Discussion -- 128
4.7. Conclusions -- 132
Supplementary Information
S1. SS Modeling of Siberia -- 133
S2. Geotherms --- 134
S3. Xenolith Data Sources --- 135
5. Chapter 5: Conclusion -- 137
5.1. Summary of Observations -- 137
5.2. Future Work -- 141
6. Appendix 1: Adaptive Difference Engine --------------------------- 143
7. References --- 149

Page intentionally left blank.

List of Figures

Figure 1.1: Common proxies used to define the lithosphere and estimate its thickness (adapted from Eaton et al, 2009). **4**

Figure 1.2: Displacement produced by a P-wave (top) and an S-wave polarized in the vertical direction (bottom). Figure adapted from Introduction to Seismology (Shearer, 2009). **13**

Figure 1.3: Global travel time curves generated using iasp91 reference earth model (Kennett and Engdahl, 1991). **15**

Figure 1.4: Transverse component of a magnitude 6.6 earthquake recorded at station WCI in Wyandotte Cave, Indiana, USA. The SS bouncepoint, depicted on the globe, is in the Pacific Ocean at 5.82° S and 135.49° W. Source, bouncepoint and receiver are represented by star, circle and inverted triangle respectively. (a) Transverse component seismogram. (b) Hilbert transformed and filtered seismogram. (c) Amplitude and time normalized to SS phase. **16**

Figure 1.5: Raypaths of the SS waveform (bold), the SS precursor (bottom-side reflection), and reverberation (top-side reflection) are shown for (a) a velocity increase with depth at the Moho and (b) a velocity decrease with depth at the lithosphere – asthenosphere boundary (LAB). Delta function are used to define the nature of discontinuities; (c) Moho and (d) LAB. The delta functions are exaggerated in the figure. **18**

Figure 1.6: Examples demonstrating the effect of (a) crustal operator (positive) and (b) negative delta function on the character of a reference wavelet. The reflection coefficient used in (a) & (b) is 0.2. **19**

Figure 2.1: Bathymetry map of the western Pacific with Ontong – Java Plateau (OJP) marked by 4000m isobath. Colored circles show bouncepoints beneath OJP (red), Nauru basin (yellow) and normal oceanic lithosphere (orange) (Korenaga and Korenaga, 2008). Colored overlays labelled SI and IB show subducted slabs (Hayes et al., 2012) along the Solomon Islands (SI) and the Izu-Bonin-Mariana trench (IB). Background colors show bathymetry and contours represent the age of seafloor in My (Müller et al., 2013). Black arrow shows the present plate motion direction. Overlay global map shows the study region (red box) and event (red star) – station (green inverted triangle) pairs that have bouncepoints beneath OJP. **28**

Figure 2.2: Schematic of a lithospheric operator (e.g. Moho and mid-lithospheric discontinuity) convolved with a reference waveform to generate a synthetic model (top). Bottom panel shows models within only a Moho (orange), only mid-lithospheric discontinuity (green), and best-fitting model that requires both Moho and mid-lithospheric discontinuity (red). Solid black line shows SS stack beneath OJP and solid grey line is the reference waveform. Error surface is represented by 95% confidence bounds. **31**

Figure 2.3: Thermal modelling of a massive melting event due to a plume on a 30 My oceanic plate. Model setup approximates the Ontong Java Plateau with thermal structure at (a) 0 My and (b) 47 My. (c) Thermal structure at the center of the original thermal anomaly at 0 My and 47 My. **34**

Figure 2.4: Fresnel zone for SS reflected off a discontinuity at 282 km depth. Panel on left shows contour of travel time difference for lateral perturbations to the SS bouncepoint. The Fresnel zone is defined by a ±T/4 contour. The top panel shows the effective Fresnel zone which is computed by summation of travel time **36**

differences for different event – station offsets. Arrows indicate the direction of propagation of the wave from event to receiver. Contours on the map show sensitivity of the Fresnel zone at intervals of 1s. The sensitivity of Fresnel zone reduces from the center, indicated by the dark red hue, towards the periphery. Colored overlays show the SI and IB slabs (Figure 2.1).

Figure 2.5: Effect of moveout in seconds for SS wave with different source – receiver offsets. (a) moveout in seconds for SS and (b) differential travel time prior to the SS phase at various reflection depths and epicentral distances (labelled on curves). Reference distance of 115° is used to calculate moveout. The moveout at 280 km is ~4s, which is less than 1/4th of the dominant period of our data, 20s. (c) SS stacks using waveforms within 90° – 140° (black) and 90° – 120° (dashed grey) epicentral distance ranges. **37**

Figure 2.6: Waveform fit and discontinuity structure beneath OJP. (a) best-fit model (red dashed) compared to the OJP data (dark grey) and reference waveform (grey). Green shaded area shows 95% confidence limits. (b) OJP data stack compared to SS stacks beneath Nauru basin (yellow), normal oceanic lithosphere (orange), and 10° bouncepoint bins in the Pacific with > 500 waveforms (blue). The shallow part of waveforms in the center panel has been greyed out to highlight the deeper discontinuity at 282 km which is not observed elsewhere in the Pacific. (c) interpretive schematic of the root structure beneath OJP. **39**

Figure 2.7: Discontinuity structure and velocity model beneath OJP compared to surface wave studies. (a) velocity models beneath the study area on northern OJP. Surface wave velocity models beneath northern OJP (red), Nauru (yellow) and the Pacific ocean north of OJP (green) from (b) SEMum2 (French et al., 2013) and (c) Covellone et al. (2015). **42**

Figure 2.8: Map of seismicity from 1964 – 2014 color coded by depth (top). Focal mechanisms of April 2014 major earthquakes shown. Bottom panels show profiles of earthquakes depth within 100 km of profile line (A-A′, B-B′, C-C′ indicated on map, x′s indicate 100 km ticks). Interpreted slab interfaces drawn on for reference (White = Australian, Red = Pacific). Red triangle is GSN station HNR. **45**

Figure 3.1: (a) Schematic of an SS bounce point. Raypaths of the SS waveform (bold), the SS precursor and reverberation are shown for (b) a velocity increase with depth (c) a velocity decrease with depth. (d, e) Lithospheric operators corresponding to velocity structures shown in (b) and (c) respectively. **58**

Figure 3.2: Event – station (epicentral distance) and back-azimuth distribution of the data used in the present study. **60**

Figure 3.3: SS bounce points used in the 10° Pacific bins. Colors represent seafloor age (Muller et al., 2013). Grey dots are bounce points with no age estimate. Solid black lines represent plate boundaries (Bird, 2003). **60**

Figure 3.4: Noise degrades quality of the stacks that have < 150 waveforms. Solid grey line is a global SS oceanic stack. The colored wiggles show stacks from 3 bins in the South Pacific where there is poor bouncepoint coverage. **61**

Figure 3.5: Visualization of effect of parameters on the models, adapted from Rychert and Shearer, 2011. (a) Forward model showing convolution of lithospheric operators with a reference waveform to generate a synthetic waveform. (b) Effect of attenuation operator (t*) on the reference S waveform. Panels (c – **63**

e) show the Earth structure that correspond to lithospheric operators in panels (f – h). Panels (i – k) show the effect of changing the depth (f), amplitude (g), and Gaussian width (h) of a lithospheric operator on the reference waveform.

Figure 3.6: Visualization of tradeoff between different parameters of a lithospheric operator for an example bin 164. (a) tradeoff between depth of discontinuity and sharpness. (b) tradeoff between depth of discontinuity and percent velocity change. The red line demarcates the region of the best-fit solutions. (c) Histogram of discontinuity depths for models that are statistically significant as determined by F-test (Fv > 6.6 for bin 164). **66**

Figure 3.7: Effect of moveout in seconds for SS waveform at different source – receiver offsets. (a) Moveout in seconds for SS. (b) Differential travel time prior to SS phase for various depth and epicentral distances (labeled on curves). Reference distance of 135° was used to calculate moveout. The moveout for a discontinuity at 120 km is < 3s, which is less than dominant period of our data, 20s. **69**

Figure 3.8: Pacific 10° SS bounce point bins with discontinuity depths. Numbers within the symbols indicate Pacific bin numbers. Colored circles and squares correspond to discontinuity depths for normal and anomalous lithosphere respectively for (a) single discontinuity (b) double discontinuity (c) positive discontinuity. Overlapping circles and squares in (b) correspond to double discontinuity with the outer color showing depth of deeper discontinuity and inner circle showing depth of shallow discontinuity. Six bins encircled by black stars indicate explicit double discontinuity. (d) white bins require only attenuation to fit the data. Black bins could not be resolved. Depth scales are different for maps (a, b and c). Background colors show seafloor **71**

age with age contours (thin black lines) at an interval of 30 My (Müller et al., 2013). Thick black lines represent plate boundaries (Bird, 2003).

Figure 3.9: Waveforms showing fit of best-fitting model (dashed red) with the data (solid grey) for positive discontinuity. Solid blue line is the weighted reference S wave corresponding to each bin and dashed green line is the attenuated S wave. Shaded region indicates 2 standard deviation error in the data. The header for each plot shows the bin numbers from figure 3.8, normal or anomalous lithosphere (N/A), age in My, depth of discontinuity in km and attenuation in seconds. **73**

Figure 3.10: Discontinuity depth versus square root of seafloor age for (a) single discontinuity and (b) double discontinuity. Circles and crosses represent normal and anomalous lithosphere respectively. Darker circles and crosses in (b) show depths of deeper discontinuity. Symbols with filled colors indicate bins with explicit double discontinuity. The remaining 20 bins could be equally well fit with a skewed Gaussian operator. The solid black lines show plate model (PM) [Stein and Stein, 1992], assuming a potential temperature of 1350°C and a plate velocity of 60 mm/yr, isotherms from 300°C to 1300°C at an interval of 200 °C. Dashed grey lines show half-space cooling (HSC) model isotherms from 300°C to 1300°C. Horizontal error bars in (a) and (b) represent the age of seafloor to one standard deviation in each bounce point bin. Vertical error bars indicate 95% confidence bounds on depth range. **74**

Figure 3.11: Waveforms showing fit of best-fitting model (red-dashed) with the data (solid grey) for single discontinuity. Solid blue line is the weighted reference S wave corresponding to each bin and dashed green line is the attenuated S wave. Shaded region **77**

indicates 2 standard deviation error in the data. The header for each plot shows the Pacific bin identifier from figure 3.8, normal or anomalous lithosphere (N/A), age in My, depth of discontinuity in km and attenuation in seconds.

Figure 3.12: Waveforms showing fit of best-fitting model using both Gaussian (dashed red) and skewed Gaussian (dashed yellow) operators with the data (solid grey) for bins with double discontinuity. Solid blue line is the weighted reference S wave corresponding to each bin and dashed green line is the attenuated S wave. Shaded region indicates 2 standard deviation error in the data. The header for each plot shows the bin numbers from figure 3.8, normal or anomalous lithosphere (N/A), age in My, depth of shallow - deep discontinuity in km and attenuation in seconds. **80**

Figure 3.13: Discontinuity depth results for bins with double discontinuity modeled using a skewed Gaussian operator. The SG depths are plotted in (a) and CDF depths in (b). The bottom panels show bins that could be equally well fit by a skewed Gaussian operator (dashed red) or a double discontinuity (two Gaussian) operator (solid grey). The black circle shows the delay time at which SG depths are calculated. The red shaded area is used to calculate the CDF depths. "Normal" and "Anomal" refers to normal and anomalous bins (Table 3.3). "G" represents a Gaussian and "G*" represents a skewed Gaussian operator. Numbers "1" and "2" represents the number of operators used. **83**

Figure 3.14: Examples of velocity – depth profiles corresponding to Gaussian (solid black) and skewed Gaussian (dashed red) discontinuity operators from figure 3.13. **84**

Figure 3.15: Discontinuity depths (bins with single discontinuity, Table 3.2) modeled using Gaussian functions compared to CDF **84**

depths from skewed Gaussian operators. Panels on the right show 4 examples of a Gaussian (grey) and skewed Gaussian (dashed red) operators that were used to model bins with a single discontinuity.

Figure 3.16: Comparison of misfit between discontinuities modeled using Gaussian (G) and skewed Gaussian (G*) operators, for bins with both single (Figure 3.8a) and double discontinuity (Figure 3.8b). The misfit function is calculated as the normalized root mean squared error in the time window 0 to 150s prior to the SS phase. **85**

Figure 3.17: Bins marked "N" represent predominantly normal oceanic crust and those marked "A" represent predominantly anomalous oceanic crust (Korenaga and Korenaga, 2008). Bins that have no depth value require no additional discontinuity and can be fit with attenuation alone. Bins marked "Fail" are noisy and have insufficient waveforms. **87**

Figure 3.18: Pacific 10° SS bouncepoint bins with discontinuity depths allowing for higher attenuation. Numbers within the symbols correspond to Pacific bin identifiers. Bins 212, 283, 308, 363 and 364 in Figure 3.8c require no additional positive discontinuity if higher attenuation (>= 6.8 s) is allowed. Circles and squares show normal and anomalous lithosphere respectively. Colors in (a) show depth of positive discontinuity. (b) White bins require only attenuation to fit the data. Black bins could not be resolved. Background colors show seafloor age with age contours (thin black lines) at an interval of 30 My (Müller et al., 2013)). Thick black lines represent plate boundaries (Bird, 2003). **89**

Figure 3.19: The shallow discontinuity at ~60 km is pervasive across most of the Pacific. Bins with no black outline show single **90**

negative discontinuity (Figure 3.8a). Bins with a thick black outline show shallow discontinuity from double discontinuity bins (Figure 3.8b). Background colors show seafloor age with age contours (thin black lines) at an interval of 30 My (Müller et al., 2013)). Thick black lines represent plate boundaries (Bird, 2003).

Figure 3.20: Depth of the shallow pervasive discontinuity compared to seafloor age and plate model (PM) / half – space cooling (HSC) isotherms. The present study is referred to as TRH. Circles (O) and crosses (X) correspond to normal (TRH - N) and anomalous lithosphere (TRH – A) respectively. Blue "O"/"X" shows results of single discontinuity and red "O"/"X" shows results of shallow discontinuity in bins with a deeper negative discontinuity (not shown). Diamonds show SS precursor results for normal (RS11-N) and anomalous (RS11-A) lithosphere from RS11 (Rychert and Shearer, 2011). Squares and pluses show LAB depths from receiver function studies of K9 (Kawakatsu et al., 2009) and KK11 (Kumar and Kawakatsu, 2011). Stars (S12) show discontinuity from previous SS precursor study (Schmerr, 2012). Colored boxes show results from TH7 (Tan and Helmberger, 2007) and GAH99 (Gaherty et al., 1999). Solid grey lines show melting region for a mantle melting model with varying amounts of water (ppm) (Katz et al., 2003). Solid black lines show isotherms for plate model (Stein and Stein, 1992) and dashed grey lines show isotherms for half space cooling model. **91**

Figure 3.21: (a) Shallow discontinuity depths compared to depth of the negative gradient in Voigt average shear velocity in a global surface wave model, SEMum2 (French et al., 2013). TRH refers to the present study. Circles (O) and crosses (X) correspond to normal (TRH – N) and anomalous lithosphere (TRH - A). (b) Discontinuity depths from present study and depths estimated from SEMum2 plotted against square root of seafloor age. **92**

Figure 3.22: Bouncepoints included in the stacks that approximate the Pacific transects, PA5 (blue) (Gaherty et al., 1999) and PAC06 (red) (Tan and Helmberger, 2007). The background colors show seafloor age (Müller et al., 2013). Waveform fits for the two transects are shown on the right. Solid grey line is the data, dashed blue is the attenuated reference S wave, dashed red is the best-fit model and dashed green in the upper panel is best-fit model using a single discontinuity. **95**

Figure 3.23: Our shallow pervasive discontinuity depths (TRH) compared to experimentally predicted depths for thermal models, JF10 (Jackson and Faul, 2010). Predicted seismic velocities assuming grain size of 20 mm, appropriate for typical mantle temperatures 1300 – 1450 °C and water content 50 – 2000 H/106Si at 150 km depth (Behn et al., 2009) for (a) half – space cooling (HSC) and (d) plate model (PM) (Stein and Stein, 1992). TRH discontinuity depths compared to predicted depths from (b) HSC and (e) PM. Predicted depth is the center of the negative velocity gradient in both HSC and PM indicated by black markers in (a) and (b). TRH discontinuity and predicted depths compared with age of bins for (c) HSC and (f) PM. Circles and crosses correspond to normal (TRH - N) and anomalous lithosphere (TRH – A) respectively. Blue color shows results of single discontinuity and red color shows results of shallow discontinuity in bins with double negative discontinuity. **96**

Figure 3.24: Discontinuity sharpness compared to thermal model. TRH refers to the present study. Gaussian width, i.e. ±2σ, of the discontinuity compared to total depth range of negative velocity gradient in JF10 for (a) HSC and (b) PM. TRH discontinuity sharpness, i.e. % change in velocity over total depth range, compared to JF10 discontinuity sharpness for (b) HSC and (e) PM. **98**

Logarithm of discontinuity sharpness (Log10 Sharpness) compared to seafloor age for (c) HSC and (f) PM. Solid grey line in (c) and (f) show logarithm of sharpness from JF10. Circles and crosses correspond to normal (TRH - N) and anomalous lithosphere (TRH – A) respectively. Blue shows results of single discontinuity and red shows results of shallow discontinuity in bins with double negative discontinuity.

Figure 3.25: TRH velocity model for Bin 129 with seafloor age of 90 My compared to JF10 velocity model for HSC (blue) and PM (green). Depth is in relation to seafloor. **99**

Figure 3.26: Schematic of a model that explain the shallow and deep discontinuity in our results. Solid and dashed grey lines show 1100 °C isotherm for PM and HSC respectively. White lines demarcate melting region for a mantle melting model with varying amounts of water (ppm) (Katz et al., 2003). **102**

Figure 4.1: How thick are the continents? A schematic showing the discrepancy between seismic and petrological continental thickness estimates. **110**

Figure 4.2: Event – station (epicentral distance) and back-azimuth distribution of the data used in the present study. **113**

Figure 4.3: Visualization o the modelling process. Discontinuities are systematically introduced and the model parameters are tested for statistical significance. **114**

Figure 4.4: Visualization of migration of waveform stack from time to depth domain using IASP91 reference Earth model. **115**

Figure 4.5: SS bouncepoints (colored circles) beneath cratons binned using 3SMAC classification (Nataf and Ricard, 1996). Pastel colors **117**

indicate lithosphere – asthenosphere boundary (LAB) depths beneath cratons, NA – North America, EUR – Europe, SIB – Siberia, SA – South America, WAF – West Africa, SAF – South Africa, IND – India, AUS – Australia, and ANT – Antarctica. Numbers in parentheses indicate number of bouncepoints. Colored triangles indicate mid – lithospheric discontinuity (MLD) depths. The black line defines region used for Hudson Bay – NA regional stack. The MLD phase beneath NA craton is only resolved in Hudson Bay – NA stack.

Figure 4.6: Waveform fits of the cratons modeled using a global oceanic SS stack as a reference waveform and simple Gaussian operators (G). The colored arrows show the location of discontinuities - red is Moho, yellow is mid – lithospheric discontinuity (MLD) and blue is the lithosphere – asthenosphere boundary (LAB). EUR, SIB and ANT could be equally well fit by skewed Gaussian operator (G*). The length of yellow and blue arrows indicate % velocity drop. The horizontal bars indicate Gaussian widths over which the velocity drop occurs. **119**

Figure 4.7: Cratons modeled using a skewed Gaussian operator. The NA, SA and SAF cratons could be equally well fit by both simple Gaussian (solid grey) and skewed Gaussian operator (dashed red). The red shaded area shows half the total velocity drop. The WAF, AUS and IND cratons could not be fit by a skewed Gaussian operator. **121**

Figure 4.8: Cratons modeled using a skewed Gaussian operator. The double discontinuity (solid grey) beneath EUR, SIB and ANT cratons could be replaced by a single skewed Gaussian operator (dashed red). Velocity - depth structures corresponding to the Gaussian (grey) and skewed Gaussian (dashed red) functions for **122**

EUR, SIB and ANT are shown in right three panels. The red shaded area shows half the total velocity drop.

Figure 4.9: (a) Moho depths resolved using SS precursors compared to average crustal thickness of cratons from CRUST1.0 (Laske et al., 2012) (b) Our MLD depths compared to receiver function studies (see text for references) (c) Our LAB depths compared to depth of the maximum negative gradient in Voigt average shear velocity in SEMum2 (French et al., 2013) (d) Our LAB depths compared to receiver function studies (see text for references) (e) Our LAB depths compared to depths estimated from diamond thermobarometry. The grey rectangular bars in (b, d) show the depth range of discontinuities observed using receiver functions. **124**

Figure 4.10: Depth – Temperature relations for xenoliths from NA, SAF and SIB. Continental conductive geotherm (dashed grey line), after Rudnick et al., 1998. Geotherms terminate in a mantle adiabat from 1200 – 1300 ˚C (shaded grey region). The graphite (G) – diamond (D) equilibrium (solid black line) is that of Kennedy and Kennedy, 1976. The carbonate – silicate solidus (solid red line) is that of Thompson et al, 2016. SS LAB results are indicated by dashed green and dashed magenta lines. **131**

Figure 4.11: Waveform fits for SS Siberia stack (solid grey) modeled with an additional deeper discontinuity at 187 km. (a) Discontinuities at 83 km and 123 km modeled using two symmetric Gaussian operators. (b) Discontinuities at 83 km and 123 km modeled using a single skewed Gaussian operator centered at 115 km depth. **133**

Figure A1: Graphical representation of the Differential Evolution Algorithm. Elliptical contours represent the function f(x,y) (a) population is generated from a bounded parameter space (b) two **145**

randomly selected population vectors (z_1, z_2) are used to generate a weighted difference vector, $F.(z_1 - z_2)$ (c) a trial or mutant vector (u_1) is created by adding the weighted difference vector to a third randomly selected population vector, z_3 (d) the mutant vector competes with the population vector of same index to achieve the lower objective function value. The survivors become parents for the next generation of the evolutionary cycle.

List of Tables

Table 3.1: Positive discontinuity results for individual SS bounce point bins. **74**

Table 3.2: Single discontinuity results for individual SS bounce point bins. **76**

Table 3.3: Double discontinuity results for individual SS bounce point bins. **79**

Table 3.4: Bins with no discontinuity and failed bins. **86**

Table 4.1: SS discontinuity structure beneath cratons. **120**

Page intentionally left blank.

Academic Thesis: Declaration of Authorship

I, **Saikiran Tharimena**, declare that this thesis and the work presented in it are my own and has been generated by me as the result of my own original research:

Global Seismic Imaging of Lithospheric Discontinuities using SS Precursors

I confirm that:

1. This work was done wholly or mainly while in candidature for a research degree at this university under the supervision of
    a. **Dr. Catherine A. Rychert** (Primary Advisor, *Ocean and Earth Science*)
    b. **Dr. Nicholas Harmon** (Co- Advisor, *Ocean and Earth Science*)
    c. **Prof. Paul White** (Co- Advisor, *Institute of Sound and Vibration Research*)
    d. **Prof. Jonathan Bull** (Chair of Advisory Panel, *Ocean and Earth Science*)
2. Where any part of this thesis has previously been submitted for a degree or any other qualification at this university or any other institution, this has been clearly stated;
3. Where I have consulted the published work of others, this is always clearly attributed;
4. Where I have quoted from the work of others, the source is always given. With the exception of such quotations, this thesis is entirely my own work;
5. I have acknowledged all main sources of help;

6. Where the thesis is based on work done by myself jointly with others, I have made clear exactly what was done by others and what I have contributed myself;
7. Either none of this work has been published before submission, or parts of this work have been published as:
    a. **Chapter 2:** Tharimena, S., Rychert, C. A., Harmon, N., 2016. Seismic imaging of a mid-lithospheric discontinuity beneath Ontong Java Plateau. *Earth and Planetary Science Letters,* 450, 62 – 70, DOI: 10.1016/j.epsl.2016.06.026

    b. **Chapter 3:** Tharimena, S., Rychert, C. A., Harmon, N., White, P. R., 2017. Imaging Pacific lithosphere seismic discontinuities – Insights from SS Precursor Modeling. *Journal of Geophysical Research: Solid Earth,* 122(3), 2131 – 2152, DOI: 10.1002/2016/JB013526

    c. **Chapter 4:** Tharimena, S., Rychert, C. A., Harmon, N., 2017. A unified continental thickness from seismology and diamonds suggests a melt defined plate. *Science,* 357 (6351), 580 – 583, DOI: 10.1126/science.aan0741
8. Experimental design, data collection / analysis was done and manuscripts were written / revised by myself with input from and discussions with the co-authors.

Saikiran Tharimena

April, 2017

Acknowledgements

Undertaking this PhD has been a truly life-changing experience for me. It would not have been possible to do without the guidance and support that I received from many people.

First and foremost, I would like to express my heartfelt appreciation and gratitude to Kate Rychert for all the support and encouragement she gave me over the past few years at Southampton. She has been nothing short of an amazing mentor. Without her scientific insight, guidance and constant feedback this PhD would not have been achievable. It has been an honor to be Kate's first PhD student.

I extend my deepest thanks to my co-advisors Nick Harmon and Paul White, and my thesis committee chair, Jon Bull, for their constant support and encouragement. I have very fond memories of a scientific expedition in Papua New Guinea; probably the best field work I have ever done till date. I am indebted to Nick for giving me this amazing opportunity and believing in me to single-handedly carry out a service run. I greatly appreciate the numerous discussions we had about science and life. I am grateful to Paul for his thought provoking ideas that pushed me to develop some amazing algorithms that not only improved my ability to model complex structures but also significantly improve my knowledge of signal processing and optimization.

My experience at the University of Southampton and National Oceanography Centre, which has become a second home, has been wonderful. I have everyone to thank at the National Oceanography Centre for making these past few years enjoyable and memorable. I am grateful to Jon Bull, Justin Dix, Bob Marsh, Damon Teagle and Steve Hawking for their unfailing support. I would also like to thank Jane Stephenson and Pete Martin who supported me during my stint at the National Oceanographic Library. I also extend my thanks to the administration, technical and finance team – Mary Smith, Terry Prince, Lou Wells, Clare Bonugli, Jonathan Wilkinson, Steve Hayward, Gary Fisher, John Davies, Kate Davis and Nikki Farrow, for supporting me at various stages of my PhD.

Discussions with Tom Gernon (Uni. Southampton), Shun Karato (Yale Uni.), Marc Hirschmann (Uni. Minnesota), Ulrich Faul (MIT), Nick Schmerr (Uni. Maryland), Stéphane Rondenay (Uni. Bergen), and Mike Kendall (Uni. Bristol) during the course of this work has been stimulating and helpful.

To my friends and colleagues, thank you for listening, offering me advice, and supporting me through this remarkable journey. Special thanks to Ryan Gallacher, Amani Alshatti, Hachem Kassem, Matthew Agius, Savas Ceylan, and Louise Dabeuliou.

No work of mine would be complete without expressing my gratitude to Yashwant Katpatal, who was not only my undergraduate advisor but also a mentor, a philosopher and a dear friend. His constant and unwavering support and encouragement pushed me to pursue Earth sciences.

Last but never the least I extend my deepest love, affection and gratitude to my parents – Sunder Tharimena and Anuradha Tharimena, and my sister Saipriya Tharimena. Nothing would ever have been possible without their unflagging love, support and encouragement throughout many years. I am ever indebted to them.

Saikiran Tharimena
April, 2017

Page intentionally left blank.

Page intentionally left blank.

Chapter 1

Introduction

1.1 Background

From the deepest ocean trench to the tallest mountain, plate tectonics explain the dynamics of Earth's surface in the present and the past (Condie, 1997; Frisch et al., 2010). The theory of plate tectonics was developed from the earlier theory of continental drift, proposed by Alfred Wegener in 1915 (Frisch et al., 2010). Conceptually, the theory of plate tectonics treats the Earth's surface as made up of rigid plates that move relative to each other at speeds of a few centimeter per year (Condie, 1997; Fischer et al., 2010). These rigid plates form the Earth's lithosphere, and move over the weaker asthenosphere below (White, 1988). The lithosphere, which includes the crust and part of the upper mantle and asthenosphere, is generally defined by its rheology – mechanical strength and the way it deforms (Fischer et al., 2010). The physical and chemical properties that create the rheological differences between the lithosphere and the asthenosphere are still debated. Tight constraints on observables that could distinguish the defining mechanism such as the depth and seismic velocity gradient of the base of the tectonic plate, the lithosphere–asthenosphere boundary (LAB), have proven challenging (Fischer et al., 2010). Various techniques have been used to study the lithospheric structure, particularly the LAB beneath oceans (Revenaugh and Jordan, 1991; Gaherty et al., 1999; Schmerr and Garnero, 2006; Tan and Helmberger, 2007; Bagley and Revenaugh, 2008; Rychert and Shearer, 2009, 2011; Rychert et al., 2012; Schmerr, 2012; Rychert et al., 2013; Beghein et al., 2014; Rychert et al., 2014; Auer et al., 2015; Rychert, 2015; Harmon et al., 2016; Rychert and Harmon, 2017) and continents (Debayle and Kennett, 2000; Artemieva and Mooney, 2001; Debayle et al., 2005; Kumar et al., 2006; Heit et al., 2007; Rychert et al., 2007; Hansen et al., 2009; Abt et al., 2010; Ford et al., 2010; Heit et al., 2010; Rychert and Shearer, 2010; Kumar et al., 2013; Rychert et al., 2014; Selway et al., 2015). With the advancement in seismic imaging, various discontinuities within the lithosphere, termed mid-lithospheric discontinuities (MLDs), are beginning to emerge (Ford et al., 2010; Selway et al., 2015; Tharimena et al., 2016). But information regarding its nature and the defining mechanism of the MLDs are still subject of debate. Overall, characterizing these lithospheric discontinuities globally beneath oceans and continents is essential for a better understanding of the formation and evolution of oceans and continents.

1.2 Oceanic and Continental Lithosphere

The concept of lithosphere was first introduced by Barrell based on the observations of strong gravity anomalies over continental crust (Barrell, 1914) and was later developed by Daly (Daly, 1940). The lithosphere is generally defined as a rheologically strong layer that sits on top of a weaker flowing asthenosphere (White, 1988; Eaton et al., 2009).

To first order, both oceanic and continental lithosphere are similar in that they form the rigid outermost layer of the Earth. Oceanic lithosphere provides an ideal location to understand the nature of the lithosphere–asthenosphere system. New oceanic lithosphere forms at seafloor spreading centers. As the plate / new lithosphere moves away from the ridge, it cools and thickens progressively with age. In this thermal regime, the heat from the mantle underlying the crust is lost upwards through the crust by conductive cooling. As the mantle cools, its density increases, leading to seafloor subsidence (White, 1988; Korenaga and Korenaga, 2008). A simple half-space cooling model explains subsidence for seafloor < 70 My (Korenaga, 2015; Korenaga and Korenaga, 2008; Nishimura and Forsyth, 1989; Parsons and Sclater, 1977; Stein and Stein, 1992; Watts, 1978). Yet, this simple thermal model fails to explain the shallower than predicted subsidence of old oceanic lithosphere (> 70 My). The subsidence pattern observed at older ages can be explained by plate model (Parsons and Sclater, 1977), where this apparent deviation from the half-space cooling model has been attributed to additional heat source (Parsons and Sclater, 1977; Smith and Sandwell, 1997) possibly caused due to small scale convection (Dumoulin et al., 2001; Huang and Zhong, 2005; Parsons and Mckenzie, 1978) and/or hot spot alteration (Korenaga and Korenaga, 2008). However, this simple visualization provides an intuitive measure of the thickness of the lithosphere. The thermal lithospheric thickness is classically associated with the depth at which the conductive geotherm intersects with the mantle adiabat (Figure 1.1) (Jaupart and Mareschal, 2015) – classically associated with the depth of the 1300 ºC isotherm (Artemieva, 2006). However, determining the plate thickness from a thermal model is subject to some ambiguity because it depends on assumed boundary conditions (not discussed here) (Jaupart and Mareschal, 2015). On the contrary, continental lithosphere is much thicker, colder, older, and more stable (King, 2005; Jaupart and Mareschal, 2015). A wide range of continental geotherms exist based on the values adopted for crustal and lithospheric mantle heat production (Rudnick et al., 1998), as continental heat flow is sensitive to local geology and crustal structure (Jaupart and Mareschal, 2015). In addition, pressure–temperature (*PT*) data for continental mantle xenoliths have been used to constrain the geotherms. On that assumption, if the xenolith *PT* data reflects equilibration to a conductive geotherm, its intersection with mantle adiabat results in a continental lithosphere thickness of 150 – 200 km (Rudnick et al., 1998).

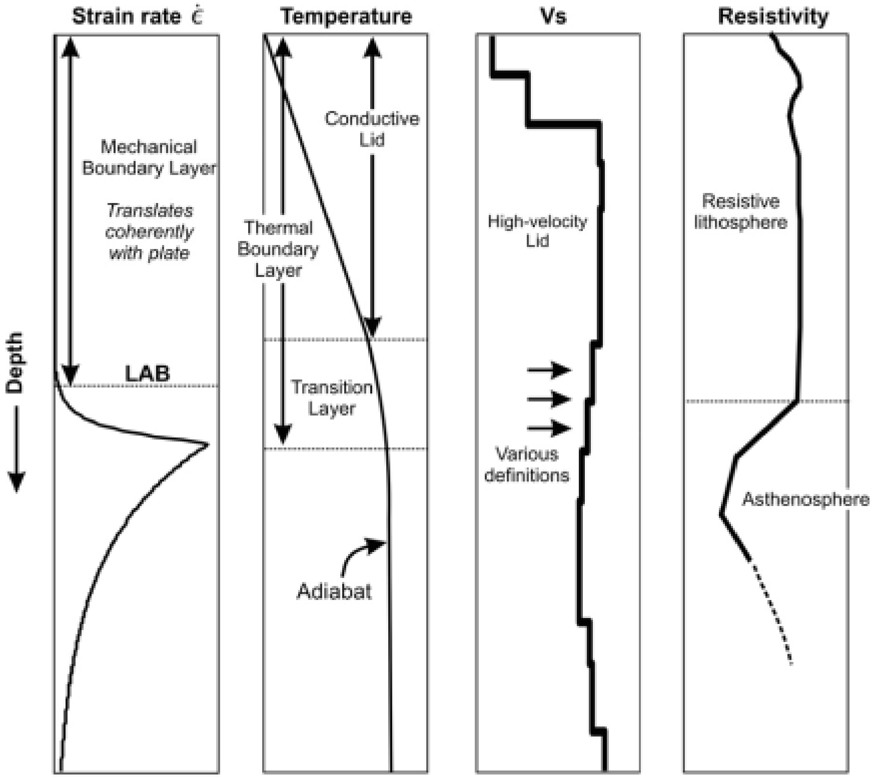

Figure 1.1: Common proxies used to define the lithosphere and estimate its thickness. (adapted from Eaton et al, 2009).

The rigid oceanic lithospheric thickness can also be measured in terms of effective elastic thickness. As the lithosphere is rigid, there is an immediate flexural response when a large load such as a seamount is added to the crust

(White, 1988). The amount of flexure supported by the rigid lithosphere can be used to calculate the effective elastic thickness, which is a function of the composition and temperature at the time of loading, and increases from 2 – 54 km as the plate ages (Watts, 1978; Watts et al., 1980). The base of the oceanic lithosphere that responds elastically is at a depth where the temperature reaches 500 ± 100 ˚C (McNutt, 1984; Jordan, 1988; Burov, 2011), at a depth of ~70 km (Burov, 2011). However, the physical meaning and significance of the effective elastic thickness for continents are still enigmatic, because effective elastic thickness for continental lithosphere bear little relation to specific geological or physical boundaries (Burov and Diament, 1995). Although the maximum effective elastic thickness in the oldest parts of the continents is 110 – 150 km, the distribution of effective elastic thicknesses is more complex, exhibiting a large scatter ranging from 0 to 70 km (Burov and Diament, 1995; Burov, 2011). Further, the elastic plate models for continents are self-inconsistent in that they mostly predict stresses high enough to lead to inelastic deformation, based on data from rock mechanics (Burov and Diament, 1995).

Since the lithosphere is generally understood to refer to the rigid plate, a mechanical lithosphere thickness is also defined. In this regime, the lithosphere is characterized by essentially no deformation, underlain by a region of high shear (Schubert et al., 1976). In other words, the strength of the lithosphere increases with increasing depth until the temperature is high enough that plastic flow occurs at a lower stress (Kohlstedt et al., 1995). The mechanical boundary layer thus defines the base of the lithosphere that translates coherently with the plate, and below which the mantle deforms. The finite measurable strength of the lithosphere has been demonstrated from observations and models of regional isostatic compensation of large topographic loads. In this mechanical regime, the uppermost layer of the earth is characterized by slow viscoelastic relaxation, in contrast to the underlying, relatively low-viscosity asthenosphere (Burov, 2011). The differential motion between the lithosphere and the asthenosphere is accommodated by either diffusion creep at the molecular level between grain boundaries or by dislocation creep at large grain size, high stress level or both (Karato and Wu, 1993; Eaton et al., 2009). Under any given conditions of temperature, pressure, grain size, stress and water content, the dominant mechanism of deformation is the one that produces the highest strain rate (Eaton et al., 2009). However, detecting this boundary may not be straightforward. While Dislocation creep results in the development of lattice–preferred orientation of mantle minerals, diffusion creep does not (Karato and Wu, 1993). Lattice-preferred orientation of mantle minerals, primarily olivine, leads to anisotropy of seismic-wave velocities (Karato, 1987; Nicolas and Christensen, 1987), which may be detected using seismic or magnetotelluric methods. Since flow laws that govern rheological behavior of polycrystalline mantle rocks are poorly know, it is generally assumed that mantle deformation is controlled by the rheological properties of olivine, which is the most abundant mineral in the upper mantle as well as the weakest component under a wide range of conditions (Kohlstedt et al., 1995; Eaton et al., 2009). Based on the rheological properties of mantle rocks, the long-term mechanical base of the lithosphere is suggested to be limited by the depth defined by 500 – 600 ˚C isotherm in the oceans, and 700 – 800 ˚C isotherm in the continents compared to almost twice as deep 1300 ˚C isotherm delimiting the thermal lithosphere (Burov, 2011).

The lithosphere has also been visualized in terms of electrical conductivity (or resistivity) which provides additional constrains on the oceanic and continental lithospheric structure. In magnetotellurics (MT) studies, the lithosphere is characterized by high resistivity or low conductivity compared to a more conductive asthenosphere. Studies of the oceanic lithosphere suggest a 60 km thick highly resistive layer over a more conductive layer (Evans et al., 1999; Baba et al., 2006). While MT studies beneath the Kaapvaal and Slave cratons (Jones, 1999; Jones et al., 2001) suggest an increase in electrical conductivity at depths of >200 km, the apparent change in resistivity/conductivity provides independent constraints on the hydration state of the lithosphere and the asthenosphere (Hirth et al., 2000; Baba et al., 2006), which in turn affect its rheological properties. However, the causes of reduction in electrical resistivity beneath the lithosphere have long been debated. For example, beneath continents partial melt provides a viable mechanism because it increases electrical conductivity (Eaton et al., 2009). Alternatively, volatiles, particularly water in the form of dissolved hydrogen has been invoked to explain elevated conductivities in the oceanic mantle (Lizarralde et al., 1995; Evans et al., 2005) and in the asthenosphere beneath continents (Hirth et al., 2000).

One of the most important feature of the continents and oceans is that they are underlain by a chemically distinct mantle, compared to a buoyant, dehydrated, melt depleted lithosphere (Lee et al., 2005). The oldest parts of the continents, cratons, are underlain by thick, highly depleted mantle keels (Jordan, 1975; Jordan, 1978; Pollack, 1986; Jordan, 1988). The convecting mantle is more fertile, characterized by Mg numbers of ~0.88 – 0.89, while the cratonic mantle is characterized by Mg numbers of ~0.92 – 0.93 (Lee et al., 2005). High degree of melt extraction produces intrinsically less dense residue due to exhaustion of dense minerals, garnet and clinopyroxene (Boyd, 1989; Lee, 2003). The positive chemical buoyancy, as a result of high melt extraction, has been suggested to counter the negative thermal buoyancy due to increase in the density of mantle keel owing to thermal contraction associated with cooler thermal conditions in the cratons (Jordan, 1988). High degrees of melt extraction also causes large degrees of dehydration that significantly increases viscosity (Hirth and Kohlstedt, 1996). Although xenolith thermobarometric data provides independent constraints on the thickness of the chemical boundary layer, the precise thickness of the chemical boundary layer beneath the cratons is debated (Lee et al., 2005). On the contrary, characterizing the chemical boundary layer beneath the oceanic lithosphere is difficult due to unavailability of xenolith samples of oceanic mantle. However, observation of ophiolites and abyssal peridotites provides a window to the oceanic mantle. Unlike cratonic mantle, there is no discontinuity in Mg number or intrinsic density in the mantle underlying oceanic crust. This leads to the entire oceanic mantle becoming negatively buoyant within 20 Ma, i.e. subductable (Lee et al., 2005). However, there is a sharp transition in viscosity at the base of the chemical boundary layer (Hirth and Kohlstedt, 1996). The mantle is suggested to be completely dehydrated at the depth of intersection of the mantle adiabat and the mantle solidus, i.e. the depth of dry melting (Karato and Jung, 1998). Experimental constraints suggest that the depth of dry melting initiates at 50 km depth for a mantle potential temperature of 1300 ˚C (Hirschmann, 2000; Lee et al., 2005).

1.2.1 The Seismic Lithosphere

The most common seismic definition of the lithosphere is that of a layer characterized by high seismic velocities, the base of which transitions to a low velocity layer (Figure 1.1). The discussion presented here focuses on passive source seismic imaging of the lithosphere, its associated discontinuities and velocity gradients. Results from previous studies, using the seismic techniques presented here, are discussed in detail in later chapters.

Seismic Surface-wave studies provide a comprehensive view of the lithospheric velocities. They suggest a systematic variation in lithospheric thickness between oceans and continents in both global and regional studies (Nishimura and Forsyth, 1989; Ritzwoller et al., 2004; Maggi et al., 2006; Cammarano and Romanowicz, 2007; Nettles and Dziewonski, 2008). Oceans are characterized by a high velocity lid that progressively thickens with age (Nishimura and Forsyth, 1989), in agreement with thermal models, while continents are characterized by fast seismic velocities extending to depths > 200 km beneath the cratons (Nettles and Dziewonski, 2008). Although all surface-wave studies image a high velocity lid, the exact depth of the base of the lithosphere often varies between these studies. Some have reported it as the depth of the strongest negative velocity gradient at the base of the high – velocity lid (Debayle and Kennett, 2000), or the depth to the center of this negative gradient (Weeraratne et al., 2003). Others reported the base of the lithosphere as the depth at which there is a change in the orientation and/or intensity of seismic anisotropy (Gaherty and Jordan, 1995), or the depth at which there is a certain % velocity anomaly with respect to a global reference model (Frederiksen et al., 2001; Gung et al., 2003) or the depth to a certain absolute velocity (Li and Burke, 2006). However, due to the difference in parameterization of the surface wave velocity models, directly comparing these base of lithosphere proxies is a challenge (Eaton et al., 2009).

Vertical variations in both radial anisotropy (seismic velocity along horizontal axis faster than vertical) and azimuthal anisotropy (fast seismic velocity only in a specific direction) from surface-wave studies have also been used to define the base of the lithosphere. For example, the base of the lithosphere has been interpreted as the depth at which the amplitude and direction of azimuthal anisotropy changes from a frozen-in fabric to alignment along current mantle flow direction (Debayle et al., 2005; Sebai et al., 2006). Reduction in radial anisotropy with depth or vertical variation from radial anisotropy in the lithosphere to azimuthal anisotropy in the asthenosphere has also been used to define the base of the lithosphere (Gaherty and Jordan, 1995; Debayle and Kennett, 2000; Gaherty, 2004; Sebai et al., 2006; Yuan and Romanowicz, 2010).

Seismic body-wave imaging techniques such as ScS reflectivity, receiver functions, and SS / PP precursors are commonly used to probe the lithospheric structure. ScS reverberations are waves that reflect between the Earth's free surface and the core–mantle boundary. The interaction of ScS phases with discontinuities produce scattered waves which are processed to yield shear impedance profiles of the mantle (Revenaugh and Jordan, 1991). ScS reflectivity has been used to image sharp negative (velocity drop) discontinuities in the LAB depth range, 72 – 112 km depth, beneath oceans (Bagley and Revenaugh, 2008). Beneath continents, an ScS study (Revenaugh and Jordan, 1991) suggested two lithospheric discontinuities, termed "H" at ~60 km (Hales, 1969) and "L" at ~220 km depth (Lehmann, 1955). The exact connection between these discontinuities and the base of the lithosphere has not been established.

Receiver functions offer a powerful tool for constraining the crust and upper mantle seismic discontinuity structure. *P*-to-*S* (*Ps*) receiver functions are more commonly used to constrain the Moho depths (Assumpcao et al., 2002; Dugda et al., 2005; Nair et al., 2006) and *S*-to-*P* (*Sp*) receiver functions are used to image the upper mantle discontinuities (Li et al., 2004; Rychert et al., 2007; Ford et al., 2010). Advancements in receiver function techniques has enabled the use of both *P-to-S* and *S-to-P* conversions for imaging the lithosphere and upper mantle discontinuities (Rychert et al., 2007; Rychert et al., 2010; Rychert and Harmon, 2016). Receiver functions have been used to image discontinuities beneath oceans and continents (Bostock, 1998; Rychert et al., 2005; Heit et al., 2007; Rychert et al., 2007; Wittlinger and Farra, 2007; Savage and Silver, 2008; Snyder, 2008; Kawakatsu et al., 2009; Rychert and Shearer, 2009; Abt et al., 2010; Ford et al., 2010; Kumar and Kawakatsu, 2011; Kumar et al., 2012a; Kumar et al., 2012b; Wolbern et al., 2012; Rychert et al., 2014). They provide better depth resolution and tighter constraints on the velocity gradients of discontinuity structures. However, receiver functions are sensitive to the Earth's structure just beneath the seismic station, and therefore have limited lateral coverage.

SS precursors have also been used to image lithospheric discontinuities beneath the oceans and continents. The SS seismic phase is an S wave that reflects once at the surface of the Earth before arriving at a station. SS precursors are underside reflections from velocity discontinuities (eg. Moho, LAB) that arrive before the main SS phase. They are valuable because of their sensitivity to the discontinuity structure beneath the bouncepoint, which is roughly halfway between the source and the receiver. SS precursors offer a powerful technique to image discontinuities at locations with sparse station coverage. They have been traditionally used to image deeper discontinuities such as the 410-, 520- and 660- km discontinuities in the mantle transition zone (Shearer, 1991; Shearer and Masters, 1992; Shearer, 1993, 1996; Flanagan and Shearer, 1998; Gu and Dziewonski, 2002; Chambers et al., 2005; Houser et al., 2008; Lawrence and Shearer, 2008; Deuss, 2009), but recent studies have used this technique to image the Pacific lithospheric discontinuities (Rychert and Shearer, 2011; Schmerr, 2012), and also constrain the Moho depths across Asia (Heit et al., 2010; Rychert and Shearer, 2010).

1.3 Outline of Data and Methods

The research presented in this thesis focuses on seismically imaging the lithosphere globally using the SS precursor method of Rychert and Shearer, 2011. A brief description of the method is presented here. Specific details of using SS precursor method to image oceanic and continental lithospheric discontinuity structures are presented in later chapters.

1.3.1 The Data

The data used in this study was obtained from the Incorporated Research Institutions for Seismology (IRIS) – Data Management Center (DMC) using the Standing Order for Data (SOD) toolkit (Owens et al., 2004). The local archive is a global dataset of earthquake seismograms of magnitude > 5.5 Mw. The data was downloaded as a three-component seismogram, two orthogonal horizontals (North (N), East (E)) and one vertical (Z) in SAC format that fully characterizes the vector nature of ground motion. Seismic Analysis Code (SAC) is a general-purpose interactive program developed by IRIS, designed for the study of sequential signal, especially time-series data. The data was preprocessed during download, using SOD, to remove instrument response. The resulting seismograms were segregated based on the events from 1990 to 2014.

The ground motion or displacement due to an earthquake is caused by two fundamental modes of wave propagation. These are termed P and S waves. For P waves, the displacement occurs in the direction of wave propagation and causes volume change, hence termed as compressional waves. For S waves, the displacement occurs perpendicular to the direction of propagation. The particle motion of an S wave is composed of two components, SV- and SH- waves. The motion within a vertical plane through the propagating vector is the SV- component and the horizontal motion in the plane perpendicular to the vertical plane is the SH- component. Since there is no volume change, this is termed shear wave. Particle motion for a harmonic P-wave and shear wave polarized in the vertical plane (SV-wave) is shown in figure 1.2.

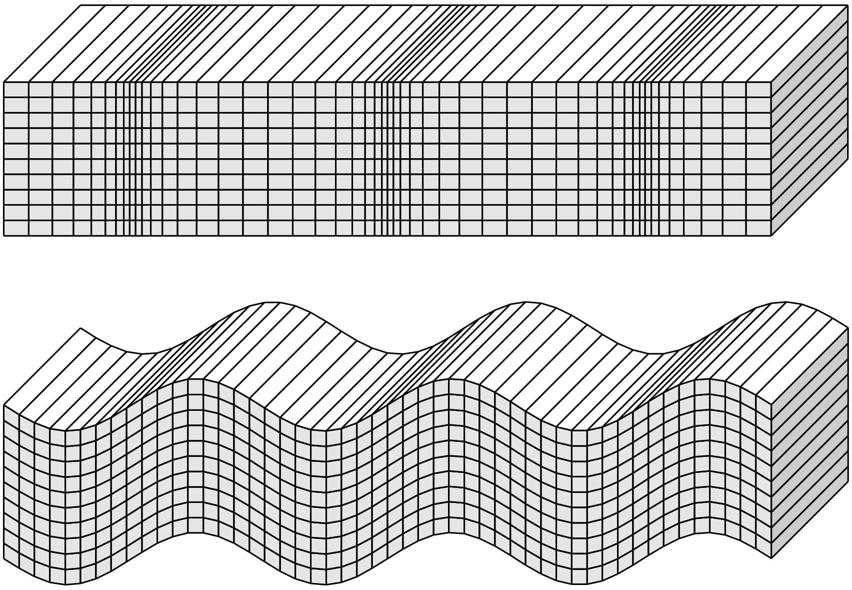

Figure 1.2: Displacement produced by a P-wave (top) and an S-wave polarized in the vertical direction (bottom). Figure adapted from Introduction to Seismology (Shearer, 2009).

The two orthogonal components (N and E) rarely correspond exactly to the SH- and SV- polarizations. A more convenient way of analyzing the seismic energy is to rotate the horizontal components from their geographic coordinates, used to align the seismometer, to the radial – tangential system. Rotation was done using matrix multiplication of a vector consisting of the north and east components with a rotation matrix:

$$\begin{bmatrix} R \\ T \end{bmatrix} = \begin{bmatrix} \cos \emptyset & \sin \emptyset \\ -\sin \emptyset & \cos \emptyset \end{bmatrix} \cdot \begin{bmatrix} N \\ E \end{bmatrix}$$

In this equation, N, E, R, T are the north, east, radial and transverse components and $\emptyset$ is the angle of rotation. Radial corresponds to the SV-polarization and is the direction along the great circle connecting the epicenter and the seismometer, and is positive in a direction away from the source. Transverse component corresponds to the SH- polarization and is orthogonal to the radial component. As SS precursors are shear waves, transverse component data was used throughout this study.

1.3.2 SS Precursors

As previously discussed, the SS seismic phase is an S wave that bounces or reflects once at the surface of the Earth before arriving at a station. The timing of the precursory phase is sensitive to the discontinuity structure below the SS surface bouncepoint (Shearer et al., 1999; Rychert and Shearer, 2010, 2011). Further, SS precursors are generally weak and cannot be consistently identified on individual seismograms. However, multiple seismograms can be stacked to bring these features above the noise. The event – station (epicentral) distance range of the data also plays an important factor as the SS seismic phase can be contaminated by other arrivals such as ScS_n (Figure 1.3). An epicentral distance range of 90° – 180° is generally used for SS precursor studies (Shearer et al., 1999; Rychert and Shearer, 2011). At epicentral distances of > 140°, the SS phase is generally contaminated by ScS_2 that arrives close in time to the SS phase. Therefore, for imaging lithospheric structure of regions with thick crust, the data is restricted to < 140° epicentral distance (Rychert and Shearer, 2010). Further, the data is restricted to events < 75 km to avoid complication from depth phases (Rychert and Shearer, 2010, 2011).

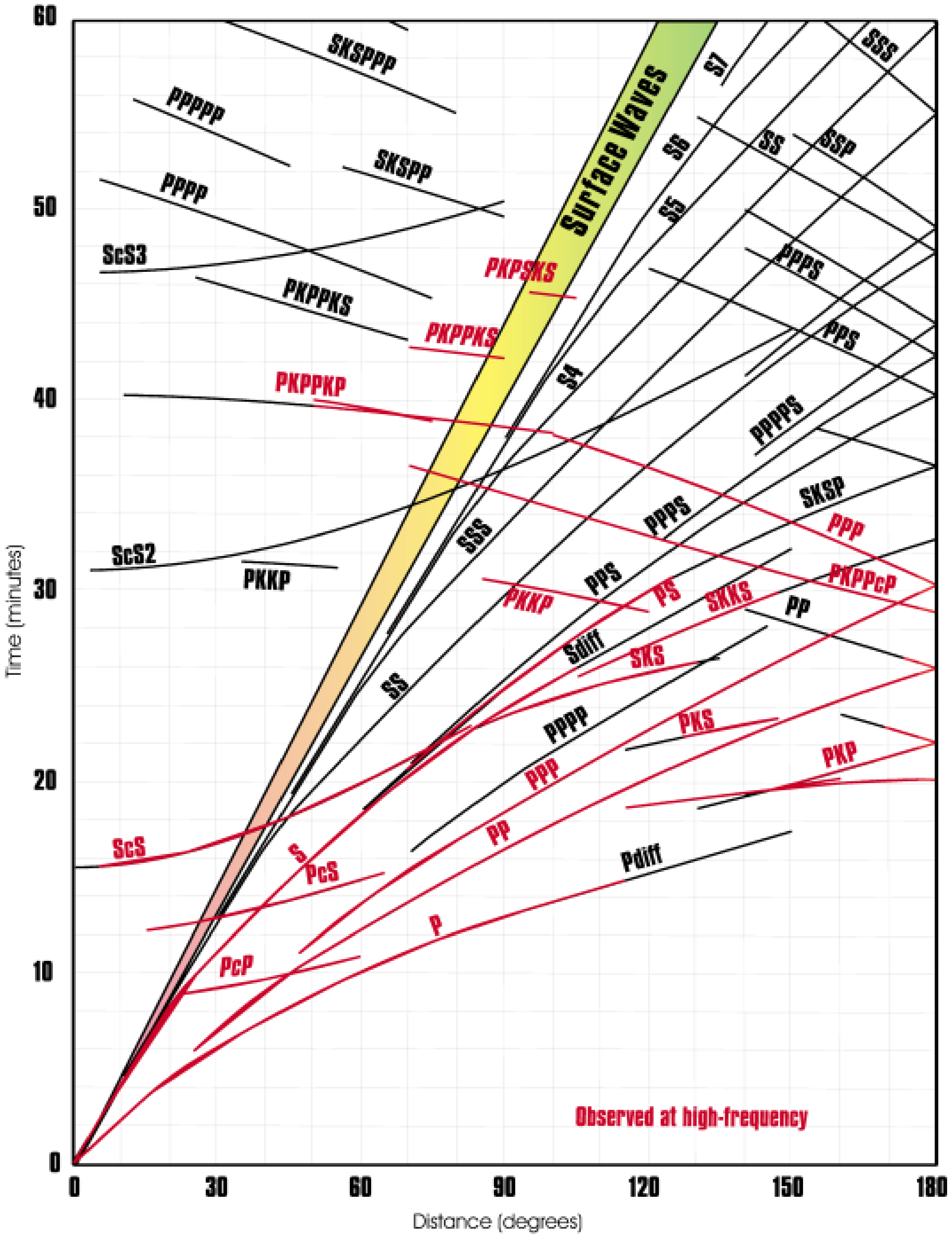

Figure 1.3: Global travel time curves generated using IASP91 reference earth model (Kennett and Engdahl, 1991; Frisch et al., 2010). Downloaded from USGS at http://neic.usgs.gov/neis/travel_times/index.html

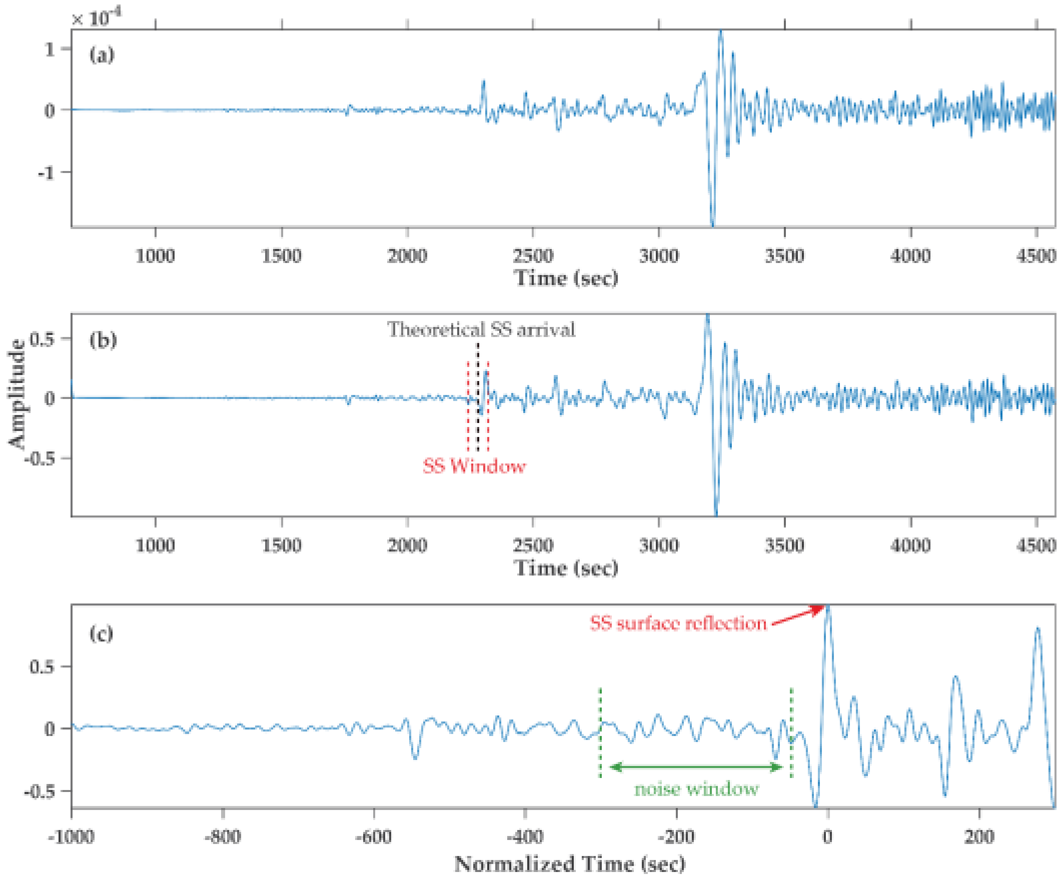

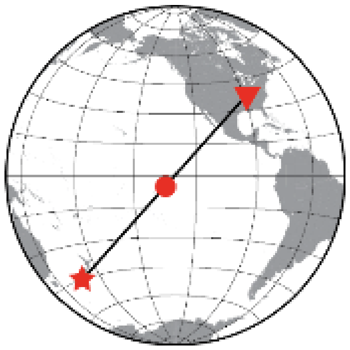

Figure 1.4: Transverse component of a magnitude 6.6 earthquake recorded at station WCI in Wyandotte Cave, Indiana, USA. The SS bouncepoint, depicted on the globe, is in the Pacific Ocean at 5.82° S and 135.49° W. Source, bouncepoint and receiver are represented by star, circle and inverted triangle, respectively. (a) Transverse component seismogram. (b) Hilbert transformed and filtered seismogram. (c) Amplitude and time normalized to SS phase.

The pre-processed transverse components are Hilbert transformed to produce symmetric pulses. The Hilbert transform does not change the amplitude spectrum of a time series; only the phase of different frequency components is affected (Shearer, 2009). The data is low-pass filtered at 0.1 Hz.

Seismograms are then inspected to eliminate records with incomplete time series. The seismogram is inspected for an SS phase which is a maximum positive or negative amplitude phase within a time window of ± 40s of the theoretical SS arrival time (Figure 1.4), based on the travel time curve in figure 1.3. Records lacking a clear SS arrival within this time window are eliminated. The amplitude and start time of each seismogram is then normalized to the picked SS phase. Records with negative SS phase are flipped to align with the maximum positive amplitude. Each record is then weighted to its apparent signal-to-noise ratio, which is calculated as the ratio of the maximum SS amplitude to the standard deviation in a 250s window preceding the SS pulse (Figure 1.4). Waveforms with signal-to-noise ratio (SNR) < 4 are rejected. Additionally, waveforms with long period noise and complicated SS arrivals are also rejected. A study region is chosen and seismograms with bouncepoints within this region are weighted to their SNR ratio and stacked. The stacked waveform is again normalized to the maximum amplitude of the SS pulse. There are 4,649,421 seismograms in the dataset of which 1,741,278 seismograms satisfy source parameters described above.

The stacked data waveform is modeled by convolving a reference waveform (see chapters 2 – 4 for details) with a lithospheric discontinuity operator to generate a synthetic waveform. A velocity discontinuity such as the Moho marks a change in composition and is characterized by a velocity jump. The sharpness of the discontinuity is related to how rapidly the change occurs with depth. Ray geometry for SS precursors relating to a velocity increase and a velocity decrease is shown in figure 1.5. Velocity discontinuities produce two first-order reflections, one arriving before the SS phase (SS precursor) and one after the SS phase (reverberation) (Figure 1.5). Higher-order reverberations are small in amplitude and usually ignored. As discussed earlier, stacking a large number of waveforms is required to bring the precursor signal above the noise.

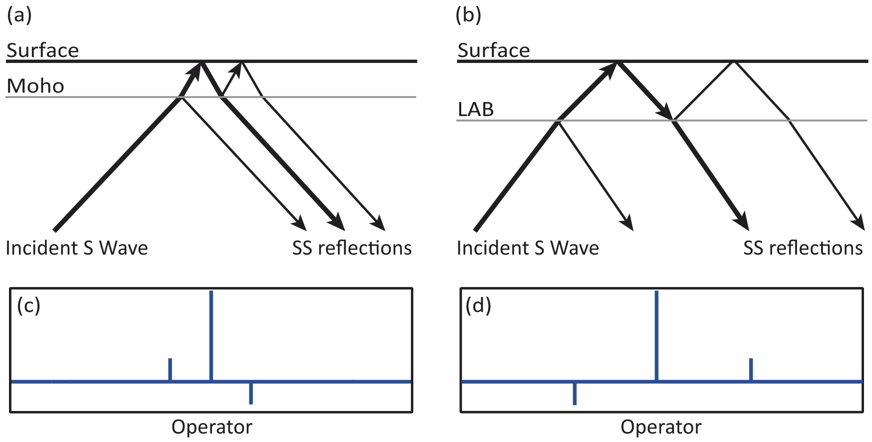

Figure 1.5: Raypaths of the SS waveform (bold), the SS precursor (bottom-side reflection), and reverberation (top-side reflection) are shown for (a) a velocity increase with depth at the Moho and (b) a velocity decrease with depth at the lithosphere – asthenosphere boundary (LAB). Delta functions are used to define the nature of discontinuities; (c) Moho and (d) LAB. The delta functions are exaggerated in the figure.

For an incident wave the underside reflection from the Moho is positively polarized arriving as a precursor and the reverberation is opposite in polarity and arrives after the main pulse. This can be defined by a delta function (Figure 1.5c) whose nature (depth and amplitude) is defined by the impedance contrast, the thickness and average velocity of the crust. The effect of crustal operators on a surface-reflected waveform using a Moho reflection coefficient of 0.2 is shown in figure 1.6 for various crustal thicknesses. For this demonstration, a reference waveform is generated by stacking thousands of long period SS waveforms.

Crustal thickness of < 10 km (oceanic) has little to no effect on the character of the reference wavelet. However, a thick crust, > 20 km (continents), significantly distorts the reference wavelet with the crustal operator increasing the amplitude of the precursory sidelobe and the sidelobe following the main SS pulse (Figure 1.6a). Similar observations can be made for a negative discontinuity, defined by a delta function (reflection coefficient of 0.2). At shallow discontinuity depths, the negative phase is obscured by the strong SS sidelobe. At deeper discontinuity depths, the delta function significantly distorts the reference wavelet producing clear phases before and after the main SS phase (Figure 1.6b).

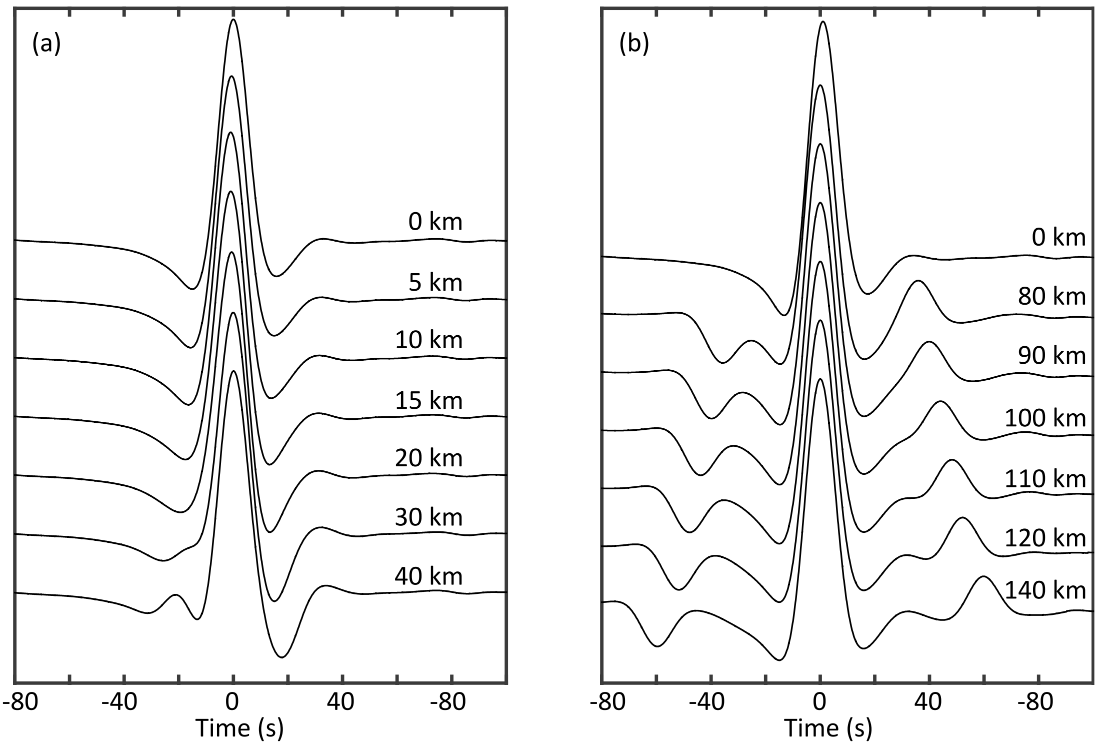

Figure 1.6: Examples demonstrating the effect of (a) crustal operator (positive) and (b) negative delta function on the character of a reference wavelet. The reflection coefficient used in (a) and (b) is 0.2.

These synthetic waveforms are checked for their goodness-of-fit with the stacked data waveform. A search algorithm is used to determine the operator(s) that gives the best-fit synthetic waveform. An operator is a Gaussian function that tests a range of discontinuity sharpnesses, i.e. step-functions to gradual velocity gradients. The best-fitting operators (model parameters) are used to determine the depth, sharpness and amplitude of the velocity discontinuity. The choice of discontinuity operators and the determination of the depth, sharpness and amplitude of velocity discontinuities is discussed in detail in later chapters.

Errors are estimated using bootstrap resampling with replacement. The error in the model parameters corresponds to the range of model parameters within the bootstrapped limits of the data. For the different studies presented in this thesis, the well resolved data stacks correspond to those where the best-fitting synthetic waveform fits the stacked SS waveform better than the reference waveform without a discontinuity operator. This is determined by the F-test for significance of regression (Hosmer et al., 1997; Draper and Smith, 1998). The number of degrees of freedom in the data waveform is determined using autocorrelation of an SS waveform. For a time-series data, the number of degrees of freedom is given by: $DoF = N\Delta t / 2T$. In this equation, N is the number of data points in the time series, Δt is the time interval between data points and T is the time interval over which the autocorrelation drops to 1/e. In other words, the more autocorrelated the data is in time, the fewer degrees of freedom there are. In the F-test, each Gaussian operator corresponds to 3 model parameters, i.e. depth, amplitude and sharpness.

1.4 Outline of Thesis

The focus of this thesis is to self-consistently image and investigate the lithospheric discontinuity structure beneath three unique tectonic environments; the Pacific Ocean, a large igneous province (proto craton), and the cratons. Understanding the nature of the lithosphere beneath these tectonic environments could possibly give us an insight into the formation and evolution of the oceans and the continents.

This work is presented as a "three – paper thesis", organized into three main chapters. The seismic structure of the Ontong Java Platea (OJP), the largest of the large igneous provinces, is investigated in chapter 2. The seismic discontinuities that define the Pacific lithosphere is investigated in chapter 3. Finally, the seismic structure of the thick cratonic roots is investigated in chapter 4.

1.5 Candidate's Contribution

The research presented in this thesis was done wholly or mainly by the author while in candidature for a research degree at the University of Southampton.

Data Acquisition: Three component seismic data from 1990 – 2009 was available on a local archive, previously acquired by the author's advisors, Dr. Catherine Rychert and Dr. Nicholas Harmon. Seismic data from 2010 – 2014 was acquired by the author. The xenolith pressure – temperature data used in chapter 4 and other data from published work was collated from literature by the author.

Data Processing: Data pre-processing and rotation from 1990 – 2009 was done by the author's advisors, Dr. Catherine Rychert and Dr. Nicholas Harmon, and from 2010 – 2014 was done by the author.

Data Analysis: Data analysis and SS precursor modeling presented in all chapters was done by the author. The scripts required for analysis were written by the author within the MATLAB® programming and modelling environment. The model setup for the thermal modelling presented in chapter 2, section 2.3.3 was provided by the author's advisor, Dr. Nicholas Harmon.

Graphics: Figures and plots presented in this thesis were generated by the author using Generic Mapping Tool (GMT) and MATLAB®. Schematics were developed by the author using Adobe Illustrator®. Figures adapted from literature have been appropriately referenced when used.

Manuscripts: The manuscripts presented in this thesis were written by the author with input from and discussions with the supervisory team, primarily, Dr. Catherine Rychert and Dr. Nicholas Harmon. The manuscripts presented in chapters 2 – 3 were further improved keeping in view the recommendations suggested by anonymous journal reviewers. Suggestions from the internal and external examiners were also incorporated in chapters 1 – 5.

Chapter 2

Imaging the Ontong Java Plateau

This chapter forms a paper published in Earth and Planetary Science Letters as a research article:

Tharimena S., Rychert C. A., Harmon N., 2016. Seismic imaging of a mid-lithospheric discontinuity beneath Ontong Java Plateau. *Earth and Planetary Science Letters,* 450, 62 – 70.

Page intentionally left blank.

2.1 Abstract

Ontong Java Plateau (OJP) is a huge, completely submerged volcanic edifice that is hypothesized to have formed during large plume melting events ~90 and 120 My ago. It is currently resisting subduction into the North Solomon trench. The size and buoyancy of the plateau along with its history of plume melting and current interaction with a subduction zone are all similar to the characteristics and hypothesized mechanisms of continent formation. However, the plateau is remote, and enigmatic, and its proto-continent potential is debated. We use SS precursors to image seismic discontinuity structure beneath Ontong Java Plateau. We image a velocity increase with depth at 28 ± 4 km consistent with the Moho. In addition, we image velocity decreases at 80 ± 5 km and 282 ± 7 km depth. Discontinuities at 60 – 100 km depth are frequently observed both beneath the oceans and the continents. However, the discontinuity at 282 km is anomalous in comparison to surrounding oceanic regions; in the context of previous results it may suggest a thick viscous root beneath OJP. If such a root exists, then the discontinuity at 80 km bears some similarity to the mid-lithospheric discontinuities (MLDs) observed beneath continents. One possibility is that plume melting events, similar to that which formed OJP, may cause discontinuities in the MLD depth range. Plume-plate interaction could be a mechanism for MLD formation in some continents in the Archean prior to the onset of subduction.

2.2 Introduction

Several hypotheses have been put forward to explain continent formation. It has been suggested that cratons were formed by large mantle plume-related melting events that led to compositional depletion (Boyd, 1989), stacking of young ocean lithosphere (Calvert et al., 1995), or island arc accretion with orogenic thickening at subduction zones (Taylor and Mclennan, 1995; Lee et al., 2011), although no consensus has been reached (Lee et al., 2011). New constraints on the structure of continental cratons from seismic imaging techniques offer promising insights to the original formation mechanism of the cratons. For instance, discontinuities have recently been imaged in the 60 – 110 km depth range beneath the continents (Rychert and Shearer, 2009; Rychert et al., 2010; Selway et al., 2015), termed mid-lithospheric discontinuities (MLD). These features are enigmatic in that the physical and chemical properties that define them are not well-understood. Observations of strong sharp seismic velocity gradients suggest mechanisms besides temperature, such as melt or hydration are required (Rychert et al., 2005), although continental cratons are not likely stable in the presence of water or melt at the quantities required by seismic data (Hirth and Kohlstedt, 1995, 1996; Faul, 1997). Furthermore, although MLDs are likely related to the formation and/or the evolution of the continents, the exact connection has not been established. For instance, they may represent relict stacked slab structures (Bostock, 1999), metasomatic fronts (Tommasi and Ishikawa, 2014; Selway et al., 2015), elastically accommodated grain boundary sliding (Karato et al., 2015), or frozen-in compositional interfaces, possibly related to a previous plume melting event.

Here we focus on the seismic velocity structure of Ontong Java Plateau (OJP), a huge, completely submerged, ~120 My old volcanic edifice, more than half the size of Australia that likely formed by plume volcanism (Coffin and Eldholm, 1994). Its surface area (including Nauru, eastern Mariana and Pigafetta basins), 4.11×10^6 km^2, covers 0.8% of the Earth (Coffin and Eldholm, 1994) and may be part of a much larger super-plateau that also included Manihiki and Hikurangi plateaus (Chandler et al., 2013). The separation of the plateaus likely occurred via interaction with a nearby triple junction around the time of formation (isochrons in Figure 2.1). OJP now lies at the junction between the Pacific and Australian plates due to collision along the southern and southwestern boundaries with the Solomon Islands arc (Mann and Taira, 2004). OJP shares common elements to all of the suggested models of continent formation described above, i.e. it was formed by a large melting event which generated buoyancy — it is now resisting subduction (Mann and Taira, 2004; Miura et al., 2004), and it may eventually cause slabs to stack and/or terranes to be accreted to form a new continent. OJP's remarkable stability, low subsidence (Ito and Clift, 1998) and resistance to subduction supports comparisons to continents, leading some to suggest it represents a modern-day proto-craton (Lee et al., 2011), and an ideal place to test hypotheses for the formation of continents.

Seismic refraction and gravity studies have constrained the thick crustal structure of the OJP, an average crustal thickness of 32 km (Furumoto et al., 1976; Mann and Taira, 2004; Miura et al., 2004) and a high velocity lower crust, characteristic of large igneous provinces (Coffin and Eldholm, 1994). It has been suggested that the lower crust beneath OJP is composed of granulite facies that formed due to recrystallization of ponded and fractionated picritic melts that were emplaced during a plume event in an oceanic, plate boundary setting (Gladczenko et al., 1997; Miura et al., 2004). The free air gravity anomaly of the plateau suggests that OJP is isostatically compensated

(Gladczenko et al., 1997). However, in addition to the crust, a mantle component is thought to be required to support its topography (Gladczenko et al., 1997; Ito and Taira, 2000). Previous constraints on OJP mantle structure suggest that it is different than surrounding regions. Analysis of multiple-ScS waves suggests low shear attenuation (QScS = 253 – 366) beneath OJP in comparison to surrounding regions (Gomer and Okal, 2003), which was interpreted as a viscous mantle lithospheric root (Klosko et al., 2001).

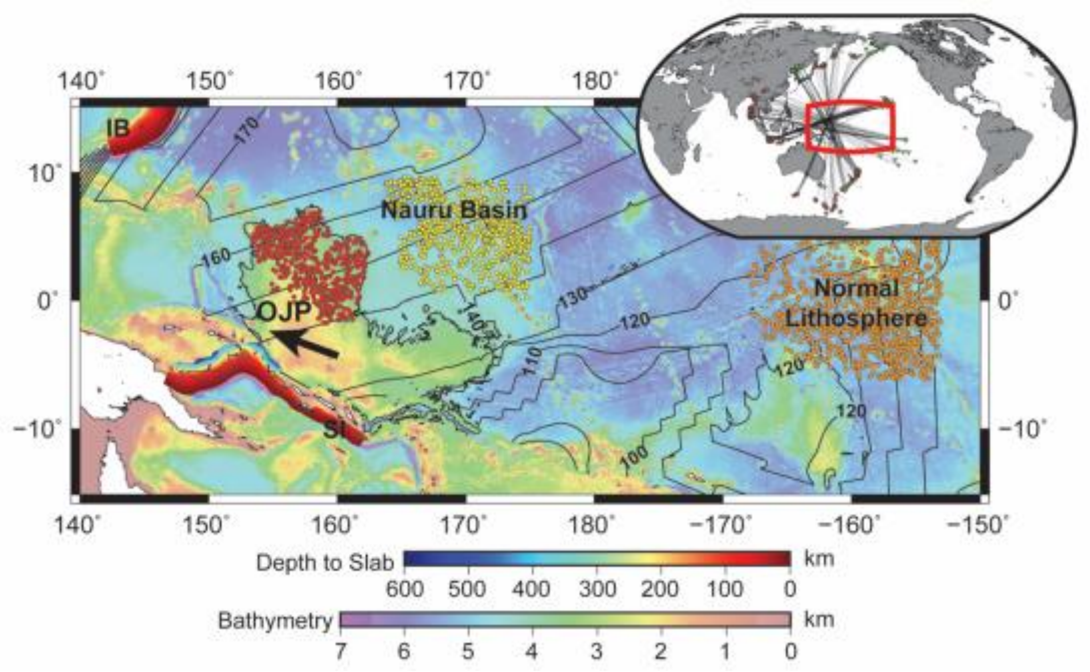

Figure 2.1: Bathymetry map of the western Pacific with Ontong – Java Plateau (OJP) marked by 4000m isobath. Colored circles show bouncepoints beneath OJP (red), Nauru basin (yellow) and normal oceanic lithosphere (orange) (Korenaga and Korenaga, 2008). Colored overlays labelled SI and IB show subducted slabs (Hayes et al., 2012) along the Solomon Islands (SI) and the Izu-Bonin-Mariana trench (IB). Background colors show bathymetry and contours represent the age of seafloor in My (Müller et al., 2013). Black arrow shows the present plate motion direction. Overlay global map shows the study region (red box) and event (red star) – station (green inverted triangle) pairs that have bouncepoints beneath OJP.

Similarly, variations in shear wave splitting measurements on and off the plateau suggest that asthenospheric flow is perturbed around a root-like structure that is chemically distinct and rheologically strong (Klosko et al., 2001). Regional surface wave tomography similarly suggests an anomalous mantle lithosphere beneath OJP (Richardson et al., 2000; Covellone et al., 2015). Richardson *et al*., (2000) found shear velocities 5% slower than surrounding regions, i.e., the opposite sense of typical expectations for a viscous, rigid root. Although Covellone *et al*. (2015) suggests fast shear velocities on an average across the whole plateau, the mantle lithosphere beneath northern OJP, the focus of this study, is relatively slow compared to surrounding regions (French et al., 2013; Covellone et al., 2015). These seemingly contradictory and intriguing results add to the enigma of the remote, yet massive plateau region, where in-situ measurements are scarce and seismic imaging has proven challenging.

Here we use SS precursors to image velocity discontinuities beneath the remote OJP. SS precursors are powerful in that they have sensitivity in locations where station coverage is sparse (Rychert and Shearer, 2011).

2.3 Methods

We use SS precursors method of Rychert and Shearer (2010, 2011) to image lithospheric structure beneath the plateau. SS precursors are underside reflections from velocity discontinuities that arrive before the main SS phase due to shorter paths through the upper mantle (Rychert and Shearer, 2011). SS precursors are sensitive to the discontinuity structure near the bouncepoint, which is halfway between the source and the receiver. We focus on imaging the northern part of OJP to avoid complications from subduction zone structures on the southern margin of the plateau (Figure 2.1).

2.3.1 Stacking

We used the Incorporated Research Institutions for Seismology (IRIS) earthquake dataset from 1990 to 2009 with event to station (epicentral) distances of 90° to 140°. The waveforms are pre-processed to remove instrument response. We use events with magnitude > 5.5 Mw and restrict source depth to < 75 km depth to minimize complications arising from depth phases (Rychert and Shearer, 2011). The horizontal components are rotated to radial and transverse components. We consider the transverse components, Hilbert transforming them to produce symmetric pulses. The waveforms are then low-pass filtered at 0.1 Hz. We then align the waveforms, centered on the maximum amplitude (positive or negative), in a window 40 seconds before and after the theoretical SS arrival time. The centered waveforms are normalized and the polarity of negative pulses flipped to align with the maximum positive pulse. Signal–to–noise ratio (SNR) of each waveform is calculated using standard deviation in a window 250s to 25s before the SS peak and, we reject waveforms with SNR less than four. Waveforms with long period noise were also rejected by discarding those waveforms whose SS precursor side lobe has a zero crossing of >20 seconds. We obtain 3,450 waveforms that fit the source parameters described above, 540 of which also fit the SNR criteria. The waveforms are weighted according to their SNR before stacking and the final stack is normalized to unit amplitude.

2.3.2 Discontinuity Modeling

Owing to the long period of the SS precursors (10 – 20 seconds), the underside reflections from the crust and the lithosphere do not appear as a distinct phase, but they affect the character of the SS stack (Rychert and Shearer, 2010). This variation in the character of SS stack is exploited to constrain the depth and velocity structure of the plateau using velocity discontinuity operators.

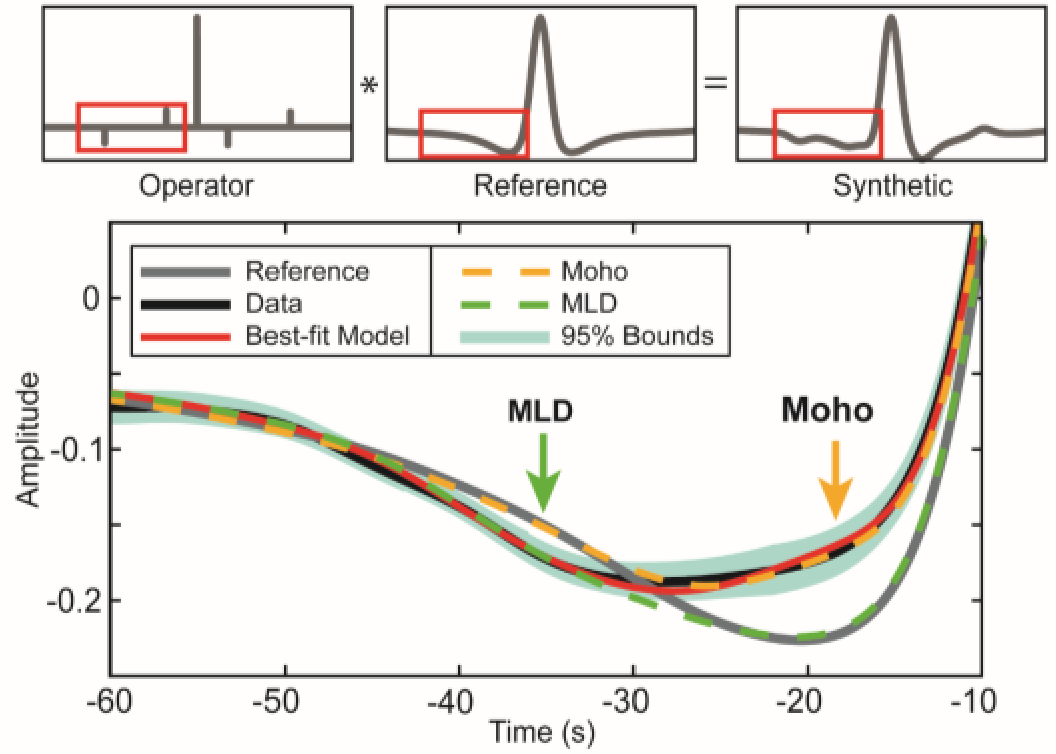

Figure 2.1: Schematic of a lithospheric operator (e.g. Moho and mid-lithospheric discontinuity) convolved with a reference waveform to generate a synthetic model (top). Bottom panel shows models within only a Moho (orange), only mid-lithospheric discontinuity (green), and best-fitting model that requires both Moho and mid-lithospheric discontinuity (red). Solid black line shows SS stack beneath OJP and solid grey line is the reference waveform. Error surface is represented by 95% confidence bounds.

We model discontinuity structure beneath the plateau using the method of Rychert & Shearer, (2011). Synthetic waveforms were produced by convolving velocity discontinuity operators with a reference waveform (Figure 2.2). A Grid-search was used to determine the best–fitting model with the lowest sum of absolute residuals. We used an F-test to determine statistical significance of the model parameters. The number of degrees of freedom in the data waveform was determined using autocorrelation of SS waveform. We estimated 11 degrees of freedom in the data in the time window used in the inversions. Our final result resolves 7 total model parameters, 3 for each of the 2 deeper negative discontinuities (amplitude, depth, and Gaussian width) and 1 for the Moho (depth). We model only SS precursors i.e. the time series preceding the SS phase. We allow both positive (velocity increase with depth such as at Moho) and negative (velocity decrease with depth such as the lithosphere – asthenosphere boundary) discontinuities in our models. We use a Gaussian function to investigate a range of discontinuity sharpnesses, i.e., step functions to gradual velocity changes (Rychert and Shearer, 2011). The sharpness of discontinuities reported in the text represents four times the Gaussian half-width, or ± 2σ. The model that yields the best-fit synthetic and is statistically significant is inverted to determine the depth, sharpness and amplitude of velocity discontinuities.

The 1-D shear velocity – depth profile is calculated from our constraints on seismic discontinuities. Operator amplitudes are scaled to velocity variation using the equation for SS reflection coefficients (Aki and Richards, 2009). We assume densities from PREM (Dziewonski and Anderson, 1981) noting that SS is affected by both density and velocity, and we do not have the ability to distinguish between the two. We construct the 1-D profile starting at the base of the root where we assume PREM velocity at 300 km depth, implementing the constrained velocity variations one by one, moving towards the surface of the Earth. Similarly, depth is scaled from the delay time of the operator, assuming the velocities of the profile. Depth is a function of the two-way travel time between the discontinuity and the free surface. The depth of discontinuity, assuming a plane wave approximation, is given by:

$$h = \sum_{0}^{i} \frac{\partial \tau_i}{2\sqrt{\beta_i^{-2} - p^2}} \qquad Equation\ 2.1$$

where $\boldsymbol{h}$ is the depth, $\boldsymbol{\partial\tau}$ is the delay time, $\boldsymbol{\beta}$ is the shear velocity, and subscript $\boldsymbol{i}$ is the step interval. We assume an average horizontal slowness, $\boldsymbol{p} = \mathbf{0.12}\ \boldsymbol{s\ km^{-1}}$. We also include a gradual, linear velocity gradient between 80 – 280 km for consistency with other work (Richardson et al., 2000; French et al., 2013), although our waveforms do not provide constraints on such gradual features.

The reference waveform is generated using a similar procedure to that of OJP stack. We used 55,200 waveforms that have SS bouncepoints beneath the Pacific to generate the reference stack. We exclude waveforms that have bouncepoints beneath the region 10° around the OJP to avoid contamination of the reference waveform.

In our modeling procedure, we systematically increased the number of operators to determine the number of statistically significant discontinuities required to explain the observations. We used an F-test for significance of regression to establish the significance of additional discontinuities. The polarity of discontinuities was also allowed to vary (positive or negative) to test for the bias in depth estimates due to contamination from sidelobes of nearby discontinuities. Error estimation for model parameters is based on bootstrap resampling with replacement and grid-search estimation. For bootstrap resampling we stack the same number of SS waveforms in the original data stack, randomly resampling waveforms included in the original stack allowing repetition of waveforms. We perform 100 bootstraps and use an automated grid search procedure to determine the best – fitting model parameters for each bootstrap. The error in the model parameters corresponds to the range of model parameters within the bootstrapped limits of the data. An F-test was also performed on the bootstraps to validate the significance of the discontinuities. The error is determined by 95% confidence limits, which corresponds to two standard deviations of the mean of the resulting variability in the bootstraps. We test for the simplest yet robust model that fits the data and explains the observations.

We investigated the effects of data filtering on sidelobes and our final results. However, there is no discernable difference in the waveform when frequencies above the low-pass used here (0.1 Hz) are included, well within the error bounds on the data. We do not apply a high-pass filter to the data in our processing. Our discontinuity results are robustly resolved. Indeed, the method used here has been shown to accurately recover Moho depths across Asia, as evidenced by high correlation with CRUST2.0, as determined by independent constraints (Rychert and Shearer, 2010).

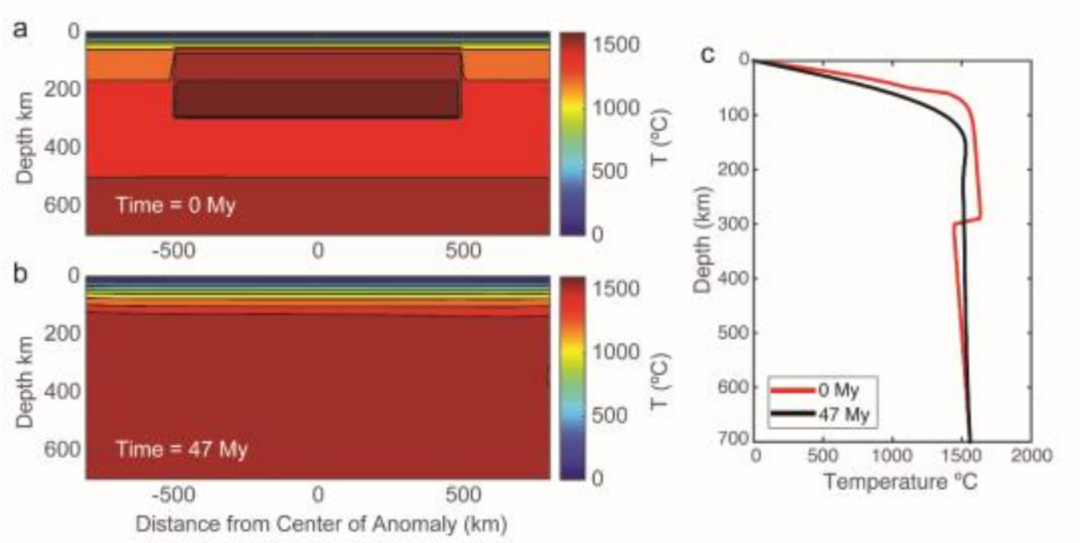

Figure 2.2: Thermal modelling of a massive melting event due to a plume on a 30 My oceanic plate. Model setup approximates the Ontong Java Plateau with thermal structure at (a) 0 My and (b) 47 My. (c) Thermal structure at the center of the original thermal anomaly at 0 My and 47 My.

2.3.3 Thermal Modeling

Since OJP is suggested to have formed due to a massive melting event, we tested how long a thermal anomaly could persist after an initial plume head arrival using a 2-D numerical model of mantle convection. We model mantle flow, mantle temperature, melting and depletion in a 2D vertical cross section approximating the Ontong Java Plateau using the method of Jha *et. al.* (Jha et al., 1994), and Harmon and Blackman (Harmon and Blackman, 2010). This method uses a finite element solver for mantle flow and a finite difference scheme for the heat equation (Smolarkiewicz, 1984; Jha et al., 1994). In the model we allow mantle melting due to the excess temperature and depletion, using the melting model of Katz *et al.* (Katz et al., 2003). We allow thermally driven convection in addition to melt and depletion buoyancy effects.

The mesh of our finite element model was made up of irregularly sized rectangular elements with 201 x 71 nodes, representing a 2000 km wide by 700 km deep box (Figure 2.3). The sides and bottom of the model are stress free, allowing inflow and outflow as necessary to accommodate the plate kinematics. We assign a zero plate velocity along the top boundary to simulate ridge perpendicular motion in 2D. Thermal boundary conditions are fixed temperatures at the top of the model of 0 °C and a specified mantle potential temperature, T_m of 1350 °C plus a mantle adiabat at the bottom of 0.3 °C/km. In our numerical experiment viscosity is pressure and temperature dependent assuming an Arrhenius form of viscosity after (Conder et al., 2002; Harmon and Blackman, 2010) that produces viscosities within the ranges for a linearized dislocation creep (Conder et al., 2002) and diffusion creep (Karato and Wu, 1993; Hirth and Kohlstedt, 1996). We limit the maximum value of viscosity to 10^{23} Pa s in the lithosphere for potential temperatures <700 °C. For our initial condition, we start with a background thermal structure for a 30 My plate, and superimpose a 200 °C thermal anomaly between 50 – 300 km depth and -500 to 500 km from the center. We allow the model to evolve through time for 92 My.

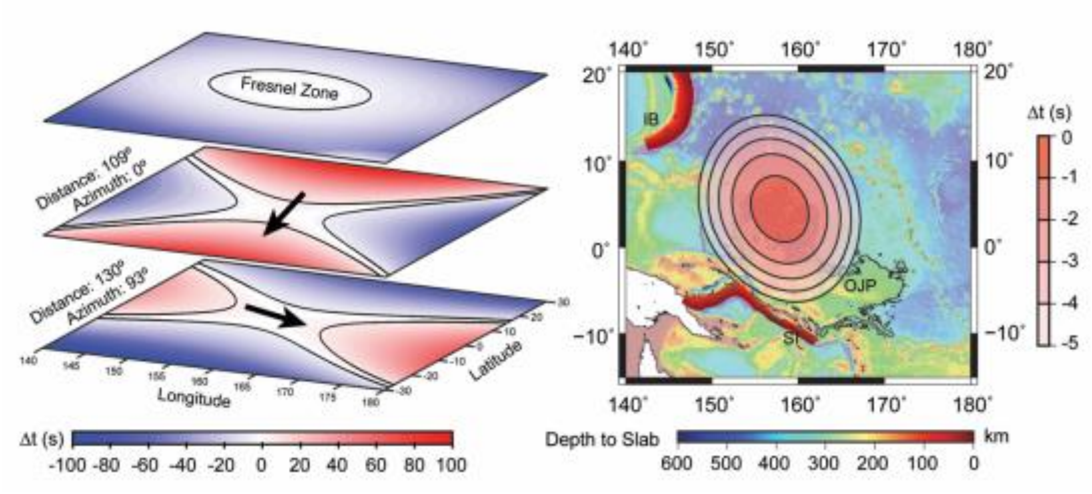

Figure 2.3: Fresnel zone for SS reflected off a discontinuity at 282 km depth. Panel on left shows contour of travel time difference for lateral perturbations to the SS bouncepoint. The Fresnel zone is defined by a ±T/4 contour. The top panel shows the effective Fresnel zone which is computed by summation of travel time differences for different event – station offsets. Arrows indicate the direction of propagation of the wave from event to receiver. Contours on the map show sensitivity of the Fresnel zone at intervals of 1s. The sensitivity of Fresnel zone reduces from the center, indicated by the dark red hue, towards the periphery. Colored overlays show the SI and IB slabs (Figure 2.1).

2.3.4 Fresnel Zone Testing

We investigated the possibility of off-axis slab structures manifesting in our OJP data at the deepest interface considered here, 282 km depth. We calculated the Fresnel zone for each bouncepoint by plotting travel time differences for non-specular reflection points from the specular reflection or the midpoint along the great circle path. The Fresnel zone for each individual bouncepoint corresponds to the saddle shaped region for which the travel time difference is < ±T/4, where T is the dominant period, ~20 s for SS (Figure 2.4). We stacked the Fresnel zones of our SS data finding a ~10° disc centered on the northern OJP (Figure 2.4). Our event – station distribution limits the effects of off–axis structure including the subducting slab along Solomon Islands, which is outside the region of sensitivity.

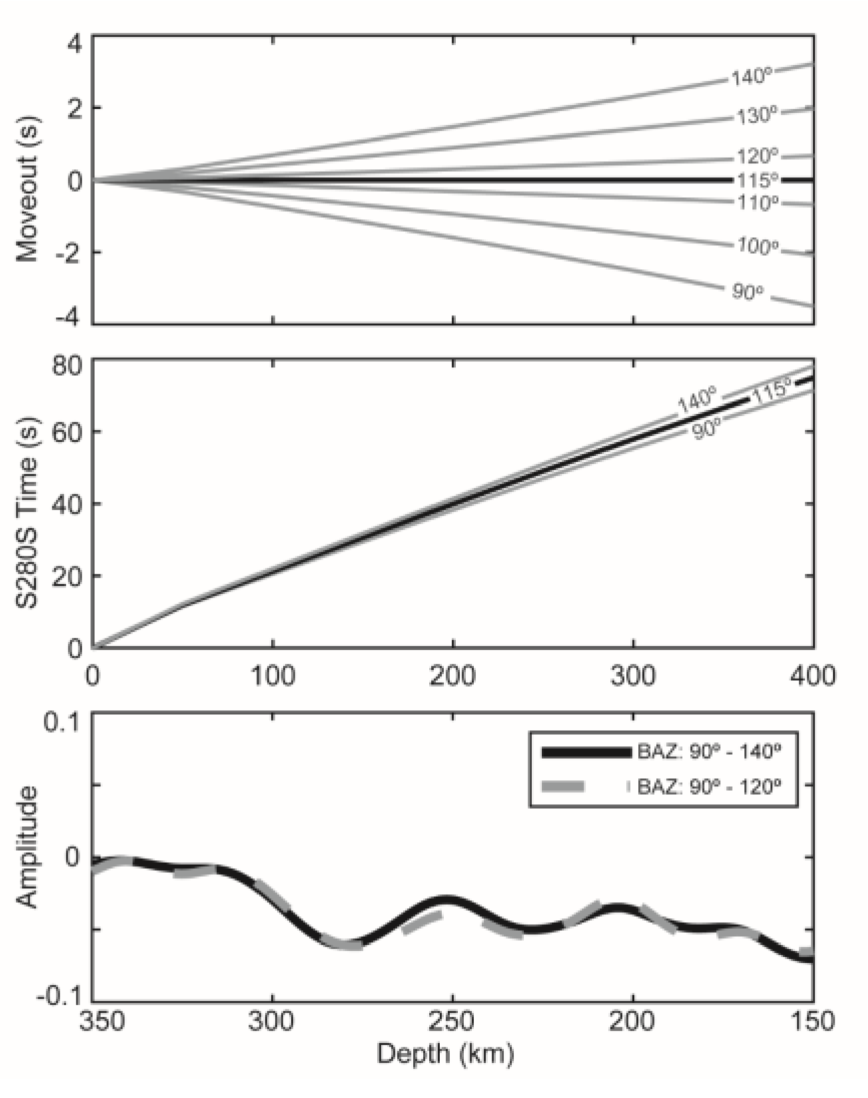

Figure 2.4: Effect of moveout in seconds for SS wave with different source – receiver offsets. (a) moveout in seconds for SS and (b) differential travel time prior to the SS phase at various reflection depths and epicentral distances (labelled on curves). Reference distance of 115 ° is used to calculate moveout. The moveout at 280 km is ~4s, which is less than 1/4th of the dominant period of our data, 20s. (c) SS stacks using waveforms within 90 °– 140 ° (black) and 90 °– 120 ° (dashed grey) epicentral distance ranges.

2.3.5 Moveout Testing

We also investigated the effect of moveout on our final result, i.e. variation in precursor-SS differential travel times for different event–station distances, which is greater for deeper discontinuity depths. We focus on the deepest interpreted phase at 282 km. Our stacks are dominated by waveforms arriving from an epicentral distance of 90° – 120°, and stacks including only those smaller distances are nearly identical to those that include the larger distance range. The moveout for an arrival from ~282 km depth within this range is ~4 seconds (Figure 2.5). This is less than ¼ of the dominant wave period (20 seconds) used in our study. Further, the stack with waveforms arriving from 90° – 120°, where there is less effect of moveout, is slightly broader, i.e. the opposite of expectation from moveout (Figure 2.5). This suggests that we are not detecting a difference caused by moveout. Therefore, while moveout may affect our constraints on the sharpness of the phase at 282 km, making the discontinuity appear slightly more gradual; it would not significantly affect our ability to image the discontinuity of interest. In practice the effect of moveout is incorporated within the error limits from the bootstrap.

2.4 Results

The OJP waveform at 0 to –45s is characterized by a broad lower amplitude sidelobe in comparison to other oceanic waveforms (Figure 2.6). This is likely owing to the thickened OJP Moho, as corroborated by the inversion results and discussed below. In addition, a significant pulse appears in the OJP stack near 282 km, which is not present in any other 10° oceanic bins.

Waveform modeling the OJP stack suggests three distinct, significant discontinuities beneath the plateau (Figure 2.6). We find a velocity increase (positive polarity) at 28 ± 4 km consistent with the Moho. A velocity decrease of 6 ± 4% is imaged at a depth of 80 ± 5 km and a velocity decrease of 5 ± 4% at a depth of 282 ± 7 km, were also imaged (Figure 2.6a). The negative discontinuities imaged at ~80 km and ~282 km are sharp, occurring over < 17 km depth. We present a best-fitting 1-D model that incorporates these seismic velocity discontinuities. The model assumes PREM velocity at 300 km depth since our results only constrain changes in velocity, rather than absolute velocity.

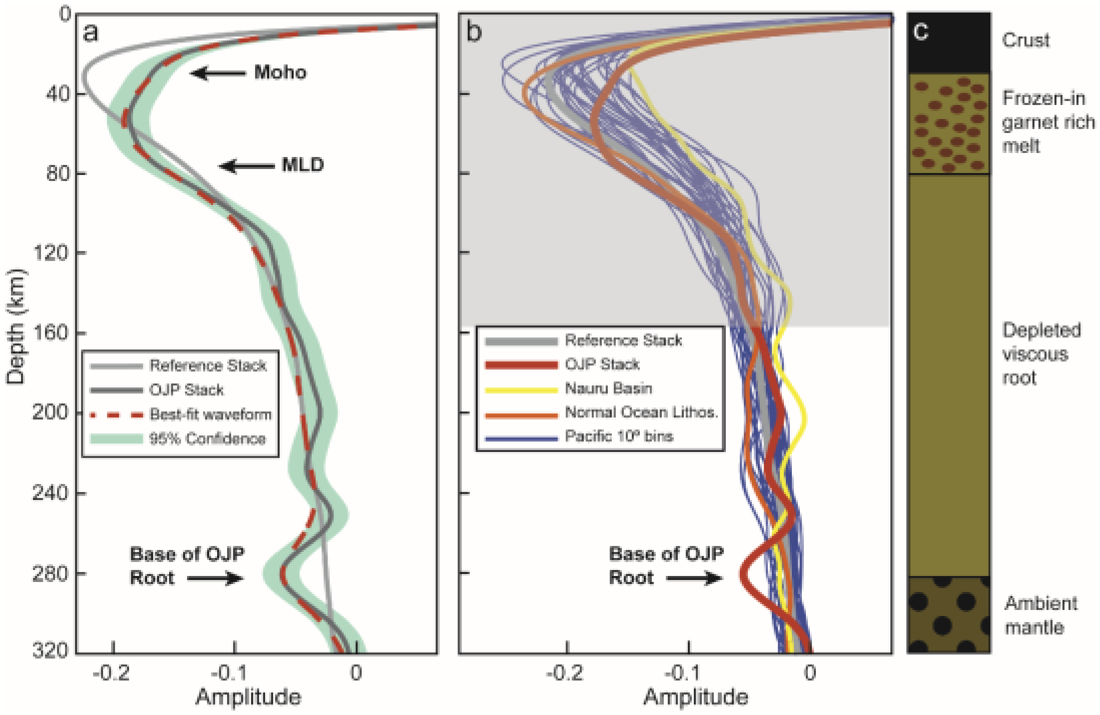

Figure 2.5: Waveform fit and discontinuity structure beneath OJP. (a) best-fit model (red dashed) compared to the OJP data (dark grey) and reference waveform (grey). Green shaded area shows 95% confidence limits. (b) OJP data stack compared to SS stacks beneath Nauru basin (yellow), normal oceanic lithosphere (orange), and 10 ° bouncepoint bins in the Pacific with > 500 waveforms (blue). The shallow part of waveforms in the center panel has been greyed out to highlight the deeper discontinuity at 282 km which is not observed elsewhere in the Pacific. (c) interpretive schematic of the root structure beneath OJP.

Finally, our numerical modeling test for the longevity of a thermal anomaly suggests that the majority of the thermal anomaly is dissipated within the first 30 My and the anomaly is entirely dissipated after 50 My. Figure 2.3a and 2.3b shows the initial thermal structure and the thermal structure at 47 My, with the thermal structure at the center of the original thermal anomaly plotted in figure 2.3c. At 47 My, the thermal anomaly is < 10 °C than the expected value from a half–space cooling model. The persistence of the anomalous structure today, 90 My after the last volcanic rejuvenation event, suggests a mechanism other than a purely thermal origin.

2.5 Discussion

The 28 ± 4 km deep Moho is in agreement with previous refraction work that found an average crustal thickness of 32 km (Furumoto et al., 1976; Miura et al., 2004). The fact that SS also requires such a deep Moho, in comparison to typical oceanic Moho depths, suggests that the thickened crust extends over a wide lateral area of the plateau. This is consistent with surface wave Moho estimates in the northern plateau area, which ranges from 26 – 32 km (Richardson et al., 2000).

The discontinuity at 80 km coincides with the gradual decrease in surface wave *SV* velocities from ~40 to 120 km depth (Richardson et al., 2000; French et al., 2013; Covellone et al., 2015). Velocity decreases with depth have been frequently imaged across at least some large sections of the Pacific in the 60 - 80 km depth range (Gaherty et al., 1999; Tan and Helmberger, 2007; Rychert and Shearer, 2011; Schmerr, 2012) including beneath the Hikurangi plateau (Stern et al., 2015), which is thought to have once been part of the same super plateau as OJP (Chandler et al., 2013). Our 80 km discontinuity may be related to other oceanic results and/or other results from ocean plateaus.

Alternatively, our observation could also be different than those of normal ocean lithosphere owing to the large melting event that is hypothesized to have formed the plateau. The same is true for OJP's sister plateaus which have had divergent histories for the past ~120 My.

The discontinuity at 282 km is the opposite sense (a velocity decrease with depth) in comparison to surface wave results that find slow velocities down to 250 – 300 km depth in comparison to surrounding regions and deeper depths (Richardson et al., 2000; Covellone et al., 2015). A gradual increase in velocity with depth from 80 to 282 km depth could reconcile the surface waves with the SS constraints (Figure 2.7a). The 282 km depth discontinuity beneath OJP is also unique. Although some observations of discontinuities at 250 km - 330 km depth have been reported, referred to as Lehmann or X, they are opposite in sign (+) in comparison to our (-) observations, more frequently associated with subduction, only rarely beneath the oceans (Deuss and Woodhouse, 2002; Bagley and Revenaugh, 2008). We do not see evidence for these positive phases in our 10° bins. We emphasize that although the region borders a subduction zone, our Fresnel zone is well outside the slab (Figure 2.4) as predicted by local tectonic, tomography, and earthquake locations. In addition, other bins of ours just as close to subduction show no sign of such a signature. Indeed, the OJP waveform looks very different at time differentials corresponding to 282 km depth from all other 10° bouncepoint bins of the Pacific, surrounding lithosphere in the Nauru Basin, or nearby "normal" lithosphere (Korenaga and Korenaga, 2008), closest in age (100 – 150 My) to that underlying OJP (130 - 150 My) (Figure 2.6b). This suggests that the OJP may be different from normal oceanic mantle down to great depth, ~282 km. An anomalous OJP mantle to ~282 km depth is evidenced in other studies as well. OJP is characterized by lower attenuation than surrounding regions

(Gomer and Okal, 2003). It also appears seismically slower in global models (French et al., 2013) and regional surface wave models (Richardson et al., 2000; Covellone et al., 2015) (Figure 2.7).

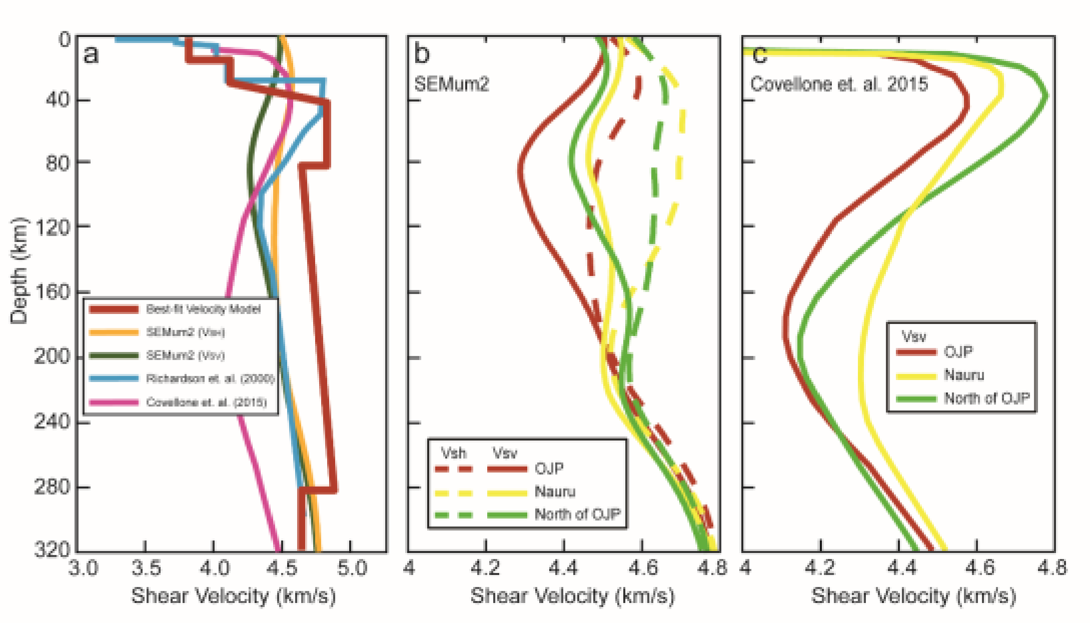

Figure 2.6: Discontinuity structure and velocity model beneath OJP compared to surface wave studies. (a) velocity models beneath the study area on northern OJP. Surface wave velocity models beneath northern OJP (red), Nauru (yellow) and the Pacific ocean north of OJP (green) from (b) SEMum2 (French et al., 2013) and (c) Covellone et al. (2015).

The physical processes that produce the 80 km and 282 km discontinuities may yield insights into the formation mechanism of the OJP. Mechanisms such as changes in anisotropy (Kawakatsu et al., 2009; Beghein et al., 2014; Rychert et al., 2014), hydration (Karato et al., 2015), melt (Kawakatsu et al., 2009; Hirschmann, 2010), or composition (Gaherty et al., 1999) may explain apparent velocity decreases with depth beneath the oceans.

2.5.1 Anisotropy

Anisotropic variations could explain apparent velocity discontinuities in SS waveforms (Rychert et al., 2014). Variability in our northern OJP study region is difficult to decipher from the broad scale of global models (Maggi et al., 2006; Beghein et al., 2014). However, azimuthal anisotropy is generally weak compared to surrounding regions in the 50 – 400 km depth range near OJP (Maggi et al., 2006). Many of our waveforms travel in a W-E or E-W direction. Therefore, if large azimuthal anisotropy did exist beneath northern OJP it could explain an apparent velocity decrease with depth if the fast direction were oriented N-S above or W-E below either the 80 km or the 282 km discontinuities. However, such orientations would not necessarily explain the anomalous nature of the mantle down to 282 km depth in comparison to surrounding regions as observed by other studies. For instance, a W-E orientation from 80 – 282 km could explain slow N-S travelling Rayleigh wave velocities (Richardson et al., 2000), although not the ~282 km discontinuity in our result or low attenuation in the region (Gomer and Okal, 2003). Overall, another mechanism would be required to explain why the region is anisotropically anomalous in comparison to surrounding regions (Klosko et al., 2001; Tommasi and Ishikawa, 2014). An increase in radial anisotropy (SH>SV) with depth can produce an apparent velocity decrease with depth in SS precursors. The anisotropy could be produced by layering or random distribution of olivine a-axes in the horizontal plane. However, surface wave models suggest decreasing radial anisotropy with depth from 80 to > 282 km under northern OJP (Figure 2.7b) (French et al., 2013; Covellone et al., 2015). In addition, as for the azimuthal anisotropy case, some other mechanism would still also be required in combination with the anisotropy either from very special current day tectonics or as a frozen-in signature to make the area distinct to 282 km in comparison to surrounding regions. Therefore, while we cannot preclude anisotropic effects, a purely anisotropic explanation for the OJP mantle is not consistent with seismic models, in which the plateau is isotropically anomalous in comparison to surrounding regions to depths of 200 – 300 km (Richardson et al., 2000; French et al., 2013; Covellone et al., 2015). Some other cause is also likely required to explain the anomalous OJP mantle.

2.5.2 Active Tectonics

The best-fitting 80 km discontinuity is sharp, occurring over < 17 km and an increase in hydration or melt with depth could explain such a sharp discontinuity. Increased water or melt at >80 km would weaken the mantle, and likely represent the LAB, precluding the possibility of a deeper viscous root beneath 80 km. Without a viscous root (e.g. hydration or melt between 80 – 282 km depth), an alternative explanation of anomalous mantle structures at deeper depths in surface wave velocity (Richardson et al., 2000; Covellone et al., 2015), attenuation (Gomer and Okal, 2003), the 80 km discontinuity and also the anomalous discontinuity at 282 km of this study would be required. However, there is no evidence for a simple active tectonic explanation for the discontinuities at 80 km or 282 km depth. Subduction tectonics at the North Solomon Trench are several 100s of kilometers south of our study area, with no evidence of slab transport towards our study region in the north in surface wave tomography (Covellone et al., 2015). Indeed, slab descent is steeply dipping and focused beneath the Solomon and New Guinea Islands, down to ~600 km depth (Figure 2.8), as illuminated by earthquake locations (Cooper and Taylor, 1985). In addition, there is no evidence for slab stagnation above the 410 km discontinuity in global surface wave studies (French et al., 2013) and P wave tomographic model (Fukao and Obayashi, 2013). Finally, xenoliths from the margins are consistent with a stable root structure related to anomalous mantle melting that extends to at least 120 km, i.e., deeper than the 80 km discontinuity (Tommasi and Ishikawa, 2014), implying that the 80 km discontinuity may not be the LAB. The xenoliths are from the plateau margin, 100s of km away from the center of our study region, where the plateau may be thinner, and likely reflect a minimum thickness for the plateau.

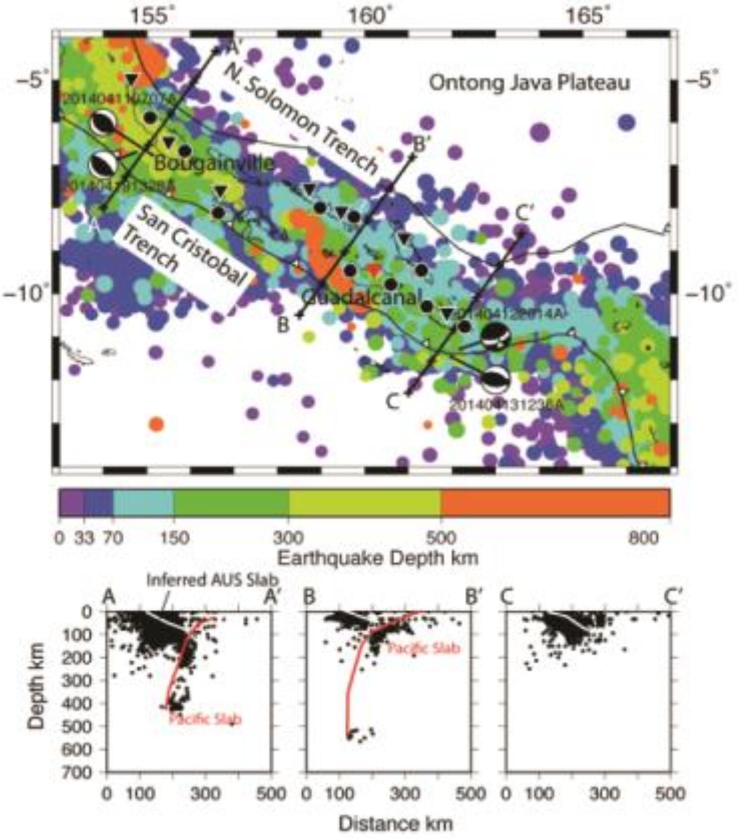

Figure 2.7: Map of seismicity from 1964 – 2014 color coded by depth (top). Focal mechanisms of April 2014 major earthquakes shown. Bottom panels show profiles of earthquakes depth within 100 km of profile line (A-A', B-B', C-C' indicated on map, x's indicate 100 km ticks). Interpreted slab interfaces drawn on for reference (White = Australian, Red = Pacific). Red triangle is GSN station HNR.

2.5.3 Elastically Accommodated Grain Boundary Sliding

The 80 km discontinuity occurs at a similar depth and with similar gradient parameters as those observed across the Pacific (Rychert and Shearer, 2011;

Schmerr, 2012). One possibility is that it is related to EAGBS, in which the effect of water on seismic waves is enhanced without necessarily causing a strong variation in viscosity (Karato et al., 2015). Although, the importance of this effect is debated (Jackson and Faul, 2010) and experimental work on hydration is beginning to emerge (Aizawa et al., 2008).

2.5.4 Compositional Origin, Possibly in a Viscous Root

Our seismic waves cannot constrain the time at which the 80 km discontinuity beneath OJP formed. One possibility is that it already existed, a compositional boundary related to depletion and dehydration that occurred at the ridge at the time the plate was formed. Discontinuities in this depth range are often imaged in the ocean basins (Gaherty et al., 1999; Tan and Helmberger, 2007; Rychert and Shearer, 2011). In this scenario compositional boundaries would need to persist despite the influence of plume melting, which might be challenging geodynamically.

Another possibility is that the ~282 km discontinuity may be related to a viscous root. How such a signature has persisted is not straightforward. For instance, a purely thermal anomaly would have dissipated within 50 My of the last volcanic pulse (Figure 2.3). Similarly, a purely thermal feature would not likely explain the sharp seismic velocity gradient observed at the base of the root or the low attenuation value for the region (Gomer and Okal, 2003). The anomalous velocity and discontinuity structure has persisted as the plateau traveled > 8000 km WNW over the past 120 My since its formation. Such persistence would suggest considerable viscosity, which is consistent with the current tectonics of the region, where the rigid plateau is resisting subduction to the south, and SKS splitting suggests mantle flow is perturbed around the root (Klosko et al., 2001). Low attenuation values similarly support this interpretation (Gomer and Okal, 2003). Such a viscous root could be a result of volcanic formation ~120 My ago and/or the rejuvenation event ~90 My ago. This differs from the LAB interpretation of a velocity drop at 73 km depth beneath Hikurangi plateau (Stern et al., 2015). Hikurangi is thought to have formed in the same large melting event as OJP (Chandler et al., 2013). However, the deeper (>100 km) discontinuity structure of Hikurangi has yet to be investigated. In addition, the super-plateau might have been laterally variable (Chandler et al., 2013) and the histories of the plateaus have diverged for 120 My.

One possible explanation for a viscous compositional root is that the magmatism and mantle upwelling that created the OJP may have left a lasting change on the residual mantle beneath, and large amounts of melting, > 30%, could have removed the garnet from the peridotite, which would result in low seismic velocities in the root beneath 80 km (Schutt and Lesher, 2006). The melting would also likely deplete and dehydrate the residual mantle, producing a viscous root that extends to the depth of melting. A high temperature and wet plume could provide the deep solidus required beneath OJP. Alternatively, depleted compositions could be transported to deeper depths via complex convection patterns as demonstrated by laboratory experiments (Griffiths and Campbell, 1990) and geodynamic modeling (King and Anderson, 1998). Or, shortening of the root may have pushed material to greater depths during interaction with the subduction zone. This mechanism can easily be reconciled with low attenuation values in the region since bulk composition is not expected to affect seismic attenuation. However, this effect can only explain a 1% velocity anomaly (Schutt and Lesher, 2006), whereas our contrast at 80 km depth is 6%, and the region is 4 – 5% slow in comparison to surrounding regions (Richardson et al., 2000; French et al., 2013).

Velocity drops of greater magnitude could arise from subtle seismic anisotropy in concert with a compositional change, frozen melts, and/or more exotic mineralogies. Since SS is sensitive to impedance, density effects could also play a role. Melt may have percolated through deeper mantle, freezing above the 80 km discontinuity. A garnet-rich rock like eclogite could increase the density and velocity of the upper 80 km. Alternatively, garnet-rich amphibolite solidified from hydrous plume melts could be seismically fast, with the added attraction of a stability boundary at a similar depth range (Allen and Boettcher, 1983). Another possibility is that small amounts of wet partial melting aided the formation of seismically slow phlogopite (Wolbern et al., 2012) at > 80 km depth. Observations of mantle peridotite from ophiolites and abyssal peridotites do not necessarily support large phlogopite percentages. However, another advantage of phlogopite is that it could 'dry-out' the olivine beneath 80 km, creating a relatively viscous mantle. Xenolith data from OJP support the notion of frozen melts and hydrous phases. There are abundant garnet-bearing pyroxenites < 80 km depth and > 100 km, with no garnet bearing xenoliths in between (Tommasi and Ishikawa, 2014). Additionally, there is evidence for metasomatism and the formation of amphibole, although it is much less abundant than the pyroxenite (Tommasi and Ishikawa, 2014). Similar metasomatic amphibole-rich layering has also been hypothesized to explain MLDs beneath the continents (Selway et al., 2015).

If a viscous root does exist to great depth beneath OJP, then the 80 km discontinuity is reminiscent of mid–lithospheric discontinuities (MLDs) observed beneath continental interiors, where xenoliths and seismic velocity anomalies support the existence of viscous roots to 200 – 250 km depth (Nettles and Dziewonski, 2008). One possibility is that large melting episodes in the Archean, similar to that which formed OJP, may have formed mid–lithospheric discontinuities observed within continental cratons today. This process may have been important in the early Archean for creating the continents, if subduction did not initiate until 3 Ga (Shirey and Richardson, 2011). Archean conditions and processes may have been much different from those operating today on OJP, i.e. higher mantle potential temperatures and possibly a stagnant lid. These higher temperatures likely enabled formation of thick basaltic crust, allowing formation of tonalite–tronghjemite–granodiorite (TTG) via re-melting of eclogite from the base of the crust (Bedard, 2006). Indeed, no TTG suites typical of Archean continental crust have been found at OJP, probably because the crust beneath OJP may not have thickened enough to produce eclogite. However, regardless of the potential temperature, Archean and modern day plumes could both potentially impart frozen-in compositional boundaries.

2.6 Conclusions

We used SS precursors to image seismic discontinuity structure beneath northern OJP. Our inversions constrain a positive Moho discontinuity at 28 ± 4 km depth and deeper negative discontinuities consistent with velocity decreases with depth at 80 ± 5 km and 282 ± 7 km. The result implies a thickened crust exists over a large lateral area of the northern plateau. The discontinuity at 282 km is not observed in our other ocean stacks, suggesting that the region may be anomalous to these depths. Thermal anomalies from the formation of the plateau via plume melting would have dissipated by now. Therefore, the persistence of anomalous structure at these depths in our result and those of others may suggest the existence of a viscous root, with the 282 km discontinuity potentially related to its base. The discontinuity at 80 km depth may be related to discontinuities observed across the Pacific at 60 – 110 km depth (Rychert and Shearer, 2011; Schmerr, 2012) and/or elastically accommodated grain boundary sliding. If it exists within a viscous root, the 80 km discontinuity is reminiscent of MLDs observed beneath continents. One possibility is that the 80 km discontinuity beneath OJP and possibly some MLD observations are compositional boundaries from previous large melting events.

Chapter 3

Imaging the Pacific Lithosphere

This chapter forms a paper which has been accepted for publication in the Journal of Geophysical Research: Solid Earth as a research article:

Tharimena S., Rychert C. A., Harmon N., White P. R., 2017. Imaging Pacific Lithosphere Seismic Discontinuities – Insights from SS Precursor Modeling. *Journal of Geophysical Research: Solid Earth (accepted).*

Page intentionally left blank.

3.1 Abstract

Oceanic lithosphere provides an ideal location to decipher the nature of the lithosphere–asthenosphere system which is vital to our understanding of plate tectonics. It is well established that oceanic lithosphere cools, thickens and subsides as it ages according to the conductive cooling models. Yet, this simple realization fails to explain various observations. For example, old oceanic lithosphere does not subside as predicted. Further, precise imaging of the lower boundary of the oceanic lithosphere has proven challenging. Here we use SS precursors to image the discontinuity structure across the Pacific Ocean using 24 years of teleseismic data. We image a sharp pervasive velocity discontinuity (3 – 15% drop over < 21 km) at 30 – 80 km depth that increases in depth with age from the ridge to at least 36 ± 9 My along the 1100 °C conductive cooling isotherm. Beneath seafloor > 36 My, there is no age–depth dependence, and we image the discontinuity at an average depth of 60 ± 1.5 km. The amplitude and sharpness of the boundary suggests a compositional variation and/or layered carbonatitic melt may be required to explain our observations rather than temperature alone. The strength and pervasiveness of the boundary suggests that it is likely related to the lithosphere–asthenosphere boundary. An additional deeper discontinuity at 80 – 120 km depth is imaged intermittently that in most cases likely represents a continuing negative velocity in depth.

3.2 Introduction

The concept of the lithosphere – asthenosphere system is well defined as the rheological boundary between the rigid lithosphere that transfers coherently and the weaker asthenosphere (Barrell, 1914; Daly, 1940), but its nature still remains enigmatic since various studies using a variety of geochemical and geophysical techniques have proposed different mechanisms to define the boundary (Regan and Anderson, 1984; Jones et al., 2001; Artemieva, 2006; Kawakatsu et al., 2009; Moorkamp et al., 2010; Rychert and Shearer, 2011; Karato, 2012). Oceanic lithosphere provides an ideal location to understand the nature of the lithosphere – asthenosphere system. To first order, oceanic lithosphere conductively cools resulting in a lithosphere that thickens progressively with age as the plate moves away from the ridge axis, leading to seafloor subsidence. Seismic imaging, heat flow and gravity studies have shown that seafloor subsides according to half – space cooling (HSC) for oceanic lithosphere < 70 My (Parsons and Sclater, 1977; Watts, 1978; Nishimura and Forsyth, 1989; Stein and Stein, 1992; Korenaga and Korenaga, 2008; Korenaga, 2015). Yet, this simple thermal model fails to explain the shallower than predicted subsidence of old oceanic lithosphere (> 70 My). This apparent deviation from the half-space cooling model has been attributed to additional heat source (Parsons and Sclater, 1977; Smith and Sandwell, 1997) possibly caused by small scale convection (Parsons and Mckenzie, 1978; Dumoulin et al., 2001; Huang and Zhong, 2005) and/or hot spot alteration (Korenaga and Korenaga, 2008).

The thickness of the oceanic lithosphere likely relates to the observed pattern of seafloor subsidence. Mapping the depth and character of the lithospheric discontinuities, primarily the lithosphere – asthenosphere boundary (LAB), the transition from the rigid plate to the weaker convecting asthenosphere, might help to explain observations such as the anomalous subsidence described above. Understanding the nature of the LAB is essential as it has important implications for the driving forces of plate tectonics and mantle convection (Fischer et al., 2010). However, mapping the LAB with existing seismic methods has proven to be a challenge; there is uncertainty on the depth, velocity contrast and sharpness of the LAB.

In geodynamic modelling, the LAB is placed at the intersection of the geotherm and adiabat that separates the conductively cooled lithosphere from the convecting mantle, classically associated with the depth of the 1300 ºC isotherm (Artemieva, 2006). In these thermal models the lithosphere thickens with age following subsidence patterns. The associated predicted seismic velocity gradients from experiments (Jackson and Faul, 2010) suggest gradual velocity gradients between the lithosphere and the asthenosphere (Rychert et al., 2012). Plate model (PM) (Stein and Stein, 1992) predictions are slightly sharper than half-space cooling (HSC), but seismic velocity gradients are still expected to be very gradual, >80 km for seafloor older than 25 My (Rychert et al., 2012). Surface waves also image a lithosphere that thickens with seafloor age over the Pacific plate in global models (Nishimura and Forsyth, 1989; Ritzwoller et al., 2004; Maggi et al., 2006; Nettles and Dziewonski, 2008). Thickening of the lithosphere has also been observed using surface waves on a regional scale near the East Pacific Rise (Harmon et al., 2009) and beneath the east Pacific Ocean ridges incorporating body waves (Gu et al., 2005). Surface waves offer the most comprehensive map of the oceanic lithosphere velocities although with limited resolution on the sharpness of the LAB transition, which is key to understanding its nature.

A variety of other methods have also been used to constrain the depth and sharpness of oceanic lithospheric discontinuities although with less comprehensive lateral coverage. A receiver function study with stations on the Pacific Plate and the Philippines plate observed a sharp (7 – 8% over 10 – 15 km) discontinuity at 51 – 95 km depth that increased in depth with age from 9 – 130 My (Kawakatsu et al., 2009; Kumar and Kawakatsu, 2011). P-to-S receiver functions from stations in the Philippines sea and northwest Pacific Ocean have been used to infer an age-dependent discontinuity with a gradual velocity change with depth beneath young seafloor, and a sharp constant depth, ~70 km, discontinuity beneath old oceanic crust (Olugboji et al., 2016). Several Pacific transect studies suggest discontinuities at relatively constant depth using a variety of phases, for instance a sharp negative discontinuity was imaged at 72 – 112 km depth using ScS phases (Bagley and Revenaugh, 2008), at 40 – 80 km depth using multiple S bounces (Tan and Helmberger, 2007), and at 54 – 64 km depth using a combination of ScS phases, multiple S bounces and surface waves (Gaherty et al., 1999). SS precursor studies have also imaged a sharp LAB but one suggesting a discontinuity at 30 – 130 km depth that increases in depth with age from 15 – 128 My (Rychert and Shearer, 2011) and the other interpreted as a very subtle age-depth dependence, a discontinuity at ~60 km (Schmerr, 2012). These studies suggest that the discontinuities imaged in the 60 – 110 km depth range beneath the Pacific may not have a simple thermal origin. Mechanisms such as chemical composition (Gaherty et al., 1999), hydration (Hirth and Kohlstedt, 1996; Karato, 2012), anisotropy (Beghein et al., 2014; Auer et al., 2015), elastically accommodated grain boundary sliding (Karato, 2012; Karato et al., 2015; Olugboji et al., 2016), and/or partial melt (Tan and Helmberger, 2007; Kawakatsu et al., 2009; Kumar and Kawakatsu, 2011) may be required along with temperature to explain these seismic observations of a boundary that does not necessarily follow a simple age – depth trend, but could affect and/or define the LAB. These discontinuities may have important implications for our understanding of the LAB. However, directly connecting these discontinuities to the LAB has proved challenging. A more comprehensive imaging of discontinuity structure at high resolution is required over an entire oceanic plate to better understand the nature, evolution and defining mechanism of the lithosphere – asthenosphere system.

In this study, we focus on seismically imaging the Pacific lithosphere using SS precursors, which are sensitive to the structure near the bouncepoints. We comprehensively image the discontinuity structure across most of the Pacific at a high resolution. We test for multiple discontinuities including positive discontinuities and provide a detailed view of the depth and pervasiveness of discontinuities across the Pacific than previously seen. Finally, we discuss possible anisotropic contributions to observed discontinuities.

3.3 Methods

We build on the SS Lithospheric Profiling (hereafter referred to as SSLIP) method of *Rychert and Shearer* (2011) (hereafter referred to as RS11) to image lithospheric discontinuities beneath the Pacific. The SS seismic phase is an S wave that bounces once at the surface of the Earth before arriving at a station (Figure 3.1). SS precursors are underside reflections from velocity discontinuities that arrive before the main SS phase due to shorter paths through the upper mantle. SS precursors are sensitive to the discontinuity structure near the bouncepoint, which is halfway between the source and the receiver (Figure 3.1a). The advantage of using SS waveforms is that it allows us to image the lithospheric structure beneath regions that have sparse station coverage. These precursors are generally weak and cannot be consistently identified on individual seismograms. However, multiple seismograms can be stacked to bring these features above the noise (Shearer, 1991b; Shearer et al., 1999). SS precursors have been traditionally used to image deeper discontinuities such as the 410-, 520- and 660- km discontinuities (Shearer, 1991b; Shearer and Masters, 1992; Shearer, 1993, 1996; Flanagan and Shearer, 1998; Deuss and Woodhouse, 2002; Gu and Dziewonski, 2002; Niu et al., 2002; Chambers et al., 2005; Houser et al., 2008; Lawrence and Shearer, 2008; Deuss, 2009). SS precursors have also been used to image shallow discontinuity structure such as the Moho across Asia (Heit et al., 2010; Rychert and Shearer, 2010), and lithospheric discontinuities beneath the Pacific (Rychert and Shearer, 2011; Schmerr, 2012) and a large igneous province (Tharimena et al., 2016).

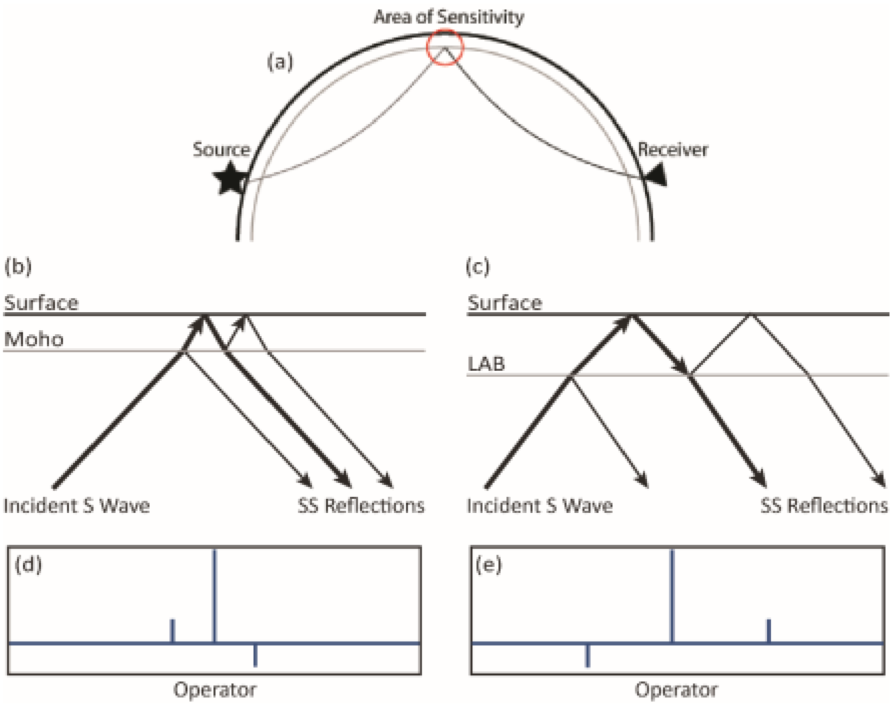

Figure 3.1: (a) Schematic of an SS bouncepoint. Raypaths of the SS waveform (bold), the SS precursor and reverberation are shown for (b) a velocity increase with depth (c) a velocity decrease with depth. (d, e) Lithospheric operators corresponding to velocity structures shown in (b) and (c) respectively.

We model stacked SS waveforms in a two-stage process. In the first stage, we model the attenuation of the SS waveform stack to generate an attenuated reference stack. Then we model the waveform by convolving lithospheric operators corresponding to velocity discontinuity structure with the attenuated reference stack.

3.3.1 Data and Stacking

We used the Incorporated Research Institutions for Seismology (IRIS) dataset from 1990 to 2014 with event to station (epicentral) distances of 90° – 180° (Figure 3.2). The waveforms were pre-processed to remove instrument response. Events with magnitude > 5.5 Mw and source depth < 75 km were used to ensure good signal–to–noise ratio and minimize complications arising from depth phases (Rychert and Shearer, 2011). The horizontal components were rotated to radial and transverse components. We considered the transverse components, Hilbert transforming them to produce symmetric pulses. The waveforms were resampled to 10 samples/second and were low-pass filtered at 0.1 Hz. An automated procedure was used to eliminate seismograms with incomplete records. The SS phase was picked as the maximum amplitude (positive or negative), in a time window 40 seconds before and after the theoretical SS arrival time. The amplitude of each seismogram was normalized to the SS phase. The waveforms were centered on the SS phase and records with negative amplitude were flipped to align with the maximum positive amplitude. Each record was then weighted to its signal–to–noise ratio, which is the ratio of the maximum SS amplitude to the standard deviation in a time window 270 s to 30 s preceding the SS pulse. Waveforms with signal–to–noise ratio < 4 were rejected. Additionally, waveforms with normalized amplitudes > 1 within a 90 s window preceding the SS pulse and/or long period noise evaluated as zero-crossing of SS pulse >

20 s were also rejected. We obtained 999,593 waveforms with bouncepoints beneath the Pacific that fit the source parameters described above, 89,478 of which also fit the signal-to-noise, SS peak and long period noise criteria (Figure 3.3). The waveforms were then aligned on the maximum amplitude, stacked, and normalized to unit amplitude.

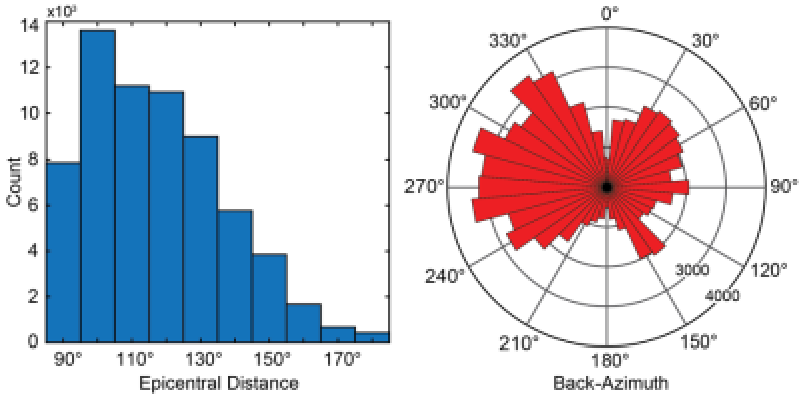

Figure 3.2: Event – station (epicentral distance) and back-azimuth distribution of the data used in the present study.

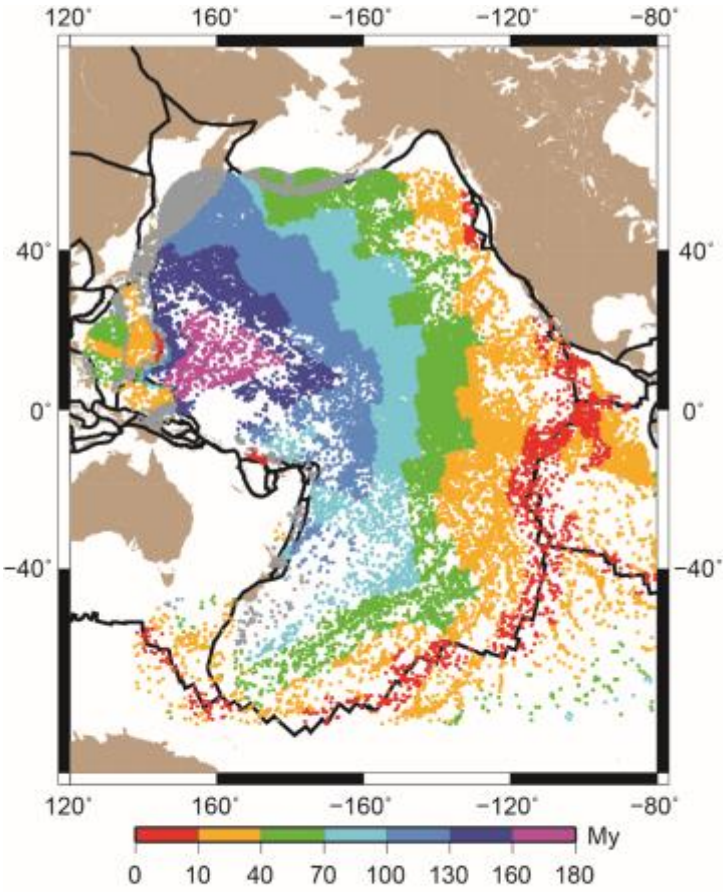

Figure 3.3: SS bouncepoints used in the 10 ° Pacific bins. Colors represent seafloor age (Muller et al., 2013). Grey dots are bouncepoints with no age estimate. Solid black lines represent plate boundaries (Bird, 2003).

3.3.2 Pacific Binning

We divided the Pacific Ocean into 10° bins, spaced about 10° apart, which approximates the Fresnel zone of the SS phase at long periods (Shearer, 1991a; Tharimena et al., 2016). Our event – station distribution results in an ~10° region of sensitivity centered on our bins, thereby limiting the effect of off-axis structures due to the saddle shaped Fresnel zone of individual SS bouncepoints (Shearer, 1991a; Deuss and Woodhouse, 2002; Tharimena et al., 2016). Waveforms with bouncepoints (Figure 3.3) within the 10° bins were stacked using the procedure described in the previous section. Although the majority of bins have > 500 waveforms, bins in the South Pacific generally have < 500 waveforms. Unlike the method of RS11, we do not restrict the inversion to bins with > 500 waveforms. This was possible since we imposed additional quality control checks on the data while stacking. The additional quality checks included rejecting waveforms with long period noise, precursor energy greater than the main SS pulse, and indiscernible SS pulses by visual inspection. These stringent standards ensured only good quality seismograms

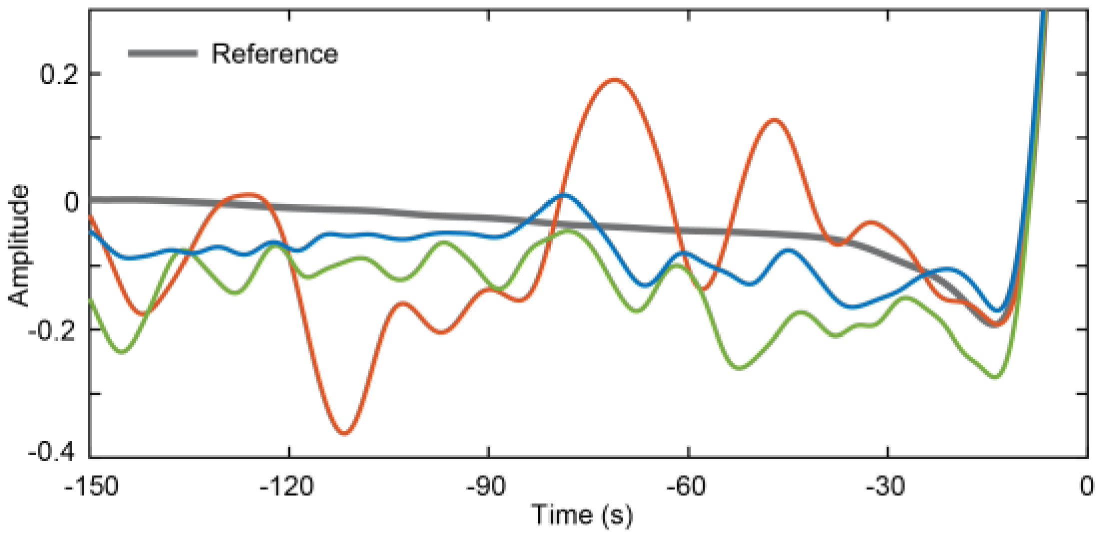

Figure 3.4: Noise degrades quality of the stacks that have < 150 waveforms. Solid grey line is a global SS oceanic stack. The colored wiggles show stacks from 3 bins in the South Pacific where there is poor bouncepoint coverage.

were included in the stack. Visual inspection of the stacks indicated that at least 150 waveforms are required to be well resolved from the best – fitting attenuated waveform, and noise degrades the quality of stacks with < 150 waveforms, for which the SNR < 4 (Figure 3.4).

Error in the data bin were estimated using bootstrap resampling with replacement. We stack the same number of SS waveforms in each bin, but randomly resampling them from the original stack of each bin allowing repetition of waveforms. We perform 100 bootstraps for each bin.

3.3.3 Pacific Bin Attributes

The age of bins is calculated as a weighted average of age of bouncepoints included in the bin determined by a spatially filtered grid from the model of *Muller et al.*, (2013). We classify bounce points in each bin as "normal" (simple history) or "anomalous" (altered) based on the correlation criteria model of *Korenaga and Korenaga* (2008). We then use the weighted average of these bounce points to classify each bin as normal or anomalous using a 50:50 cutoff.

3.3.4 Reference Phase

The reference phase is composed of an S wave stack convolved with an attenuation operator, t^*. The inversion for t^* is performed first before continuing on to the inversion for discontinuity structure. t^* was allowed to vary from 3 – 6 s in the inversions (Bhattacharyya et al., 1996). The t^* operator primarily affects the width of the main SS pulse (Rychert and Shearer, 2011) and does not interfere with the precursors (Figure 3.5). Therefore, small variation in the attenuation operator do not significantly affect the depth or sharpness of the discontinuities in our final results. The S waveform stacks are

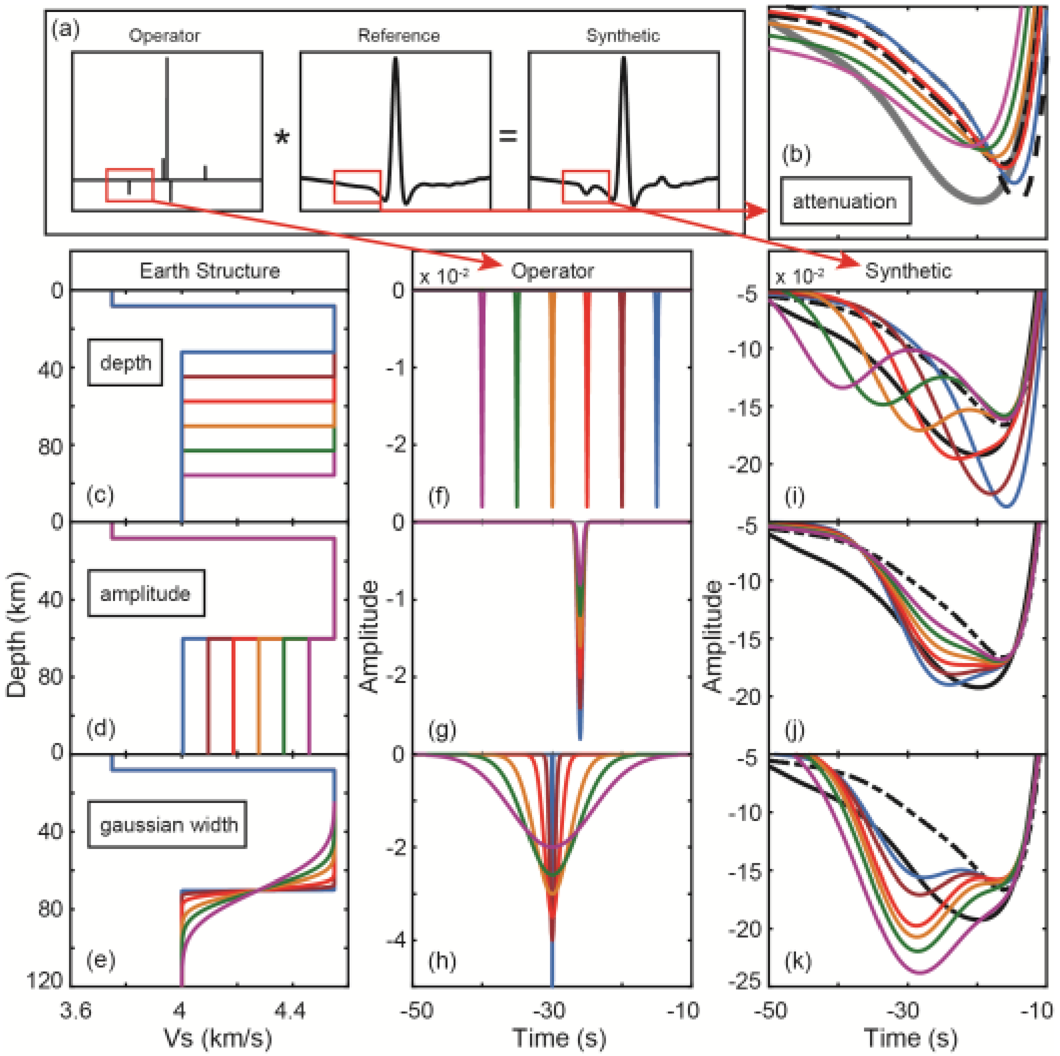

Figure 3.5: Visualization of effect of parameters on the models, adapted from Rychert and Shearer, 2011. (a) Forward model showing convolution of lithospheric operators with a reference waveform to generate a synthetic waveform. (b) Effect of attenuation operator (t) on the reference S waveform. Panels (c – e) show the Earth structure that correspond to lithospheric operators in panels (f – h). Panels (i – k) show the effect of changing the depth (f), amplitude (g), and Gaussian width (h) of a lithospheric operator on the reference waveform.*

produced using a similar procedure to that used for SS as described in section 3.3.1. We use data within epicentral distances of 30° – 55°. The same magnitude and depth cut-offs applied to SS waveforms were applied.

Waveforms are weighted to their signal–to–noise ratio. We tested two reference phases. The first reference phase is for the Pacific Ocean computed using all the S waveforms, and the second is a set of S reference stacks computed for each 10° bin using the same sources included in the corresponding SS stack. There was no significant difference in our results using either the Pacific S or bin-specific S reference waveforms. In all cases the difference in the depth estimates is < ± 4 km and amplitude is < ± 1%. For simplicity, we show results using the bin-specific S reference waveform in our study. For the bin-specific S reference stacks, the signal–to–noise ratio is scaled such that the total weight of an event (in the SS stack) is preserved in the S stacks. This eliminates possible bias from source effects that might be specific to a particular bouncepoint bin (Rychert and Shearer, 2011). The reference phase also includes a 7 km thick oceanic crust with a crustal velocity of 3.75 km/s and Moho reflection coefficient of 0.05.

We tested the effect of varying crustal thickness on our inversions. We used CRUST1.0 (Laske et al., 2012) to calculate average crustal thickness for each bin. Crustal thickness of bins varies from 6.9 km to 11.2 km with an average crustal thickness of 7.2 km across the Pacific. Only a couple of bins in the far northwest Pacific have crustal thickness of 10.1 km and 11.2 km. Our tests showed negligible effect of variable crustal operator on our inversions and hence we chose a constant crustal thickness of 7 km.

3.3.5 Modeling

We model the stacked data waveform from 0 to 300 seconds preceding the SS arrival, searching for discontinuities in the ~20 – 200 km depth range. Our synthetic waveforms are computed by convolving the attenuated reference waveform with a lithospheric operator corresponding to the discontinuity. We allowed the time-offset of the operator to vary, to model discontinuities at a variety of depths. We allowed a range of amplitudes to model a range of velocity contrasts. We allowed both positive (velocity increase with depth) and negative (velocity decrease with depth) discontinuities in our models. An example of a positive discontinuity is the Moho (Figure 3.1b, 3.1d) and a negative discontinuity is the LAB (Figure 3.1c, 3.1e). We use a Gaussian function to investigate a range of discontinuity sharpnesses, i.e., step functions to gradual velocity changes (Rychert and Shearer, 2011; Tharimena et al., 2016). We first searched for a single discontinuity. Bins that could not be resolved with a single discontinuity were then tested for double discontinuities, again either positive or negative polarity. Adding a second discontinuity to the bins that were well-fit by a single discontinuity did not give a significantly better fit. In the double discontinuity bins, we also allowed for irregularly shaped operators to test our resolution to multiple discontinuities vs. gradational velocity contrasts.

We used a differential evolution algorithm (Storn and Price, 1997; Price et al., 2005) to find the operator(s) that gives the best-fit synthetic from 0 – 300s prior to the main SS phase. This approach minimizes both the model storage size and computation time in comparison to a typical grid search (eg. RS11). In this approach, an initial set (P – parent) of lithospheric operators were chosen. These operators were convolved with a reference waveform and the goodness-of-fit of the corresponding synthetics was measured. A new set of lithospheric operators (M – mutants) were generated using a scaled difference of two randomly selected lithospheric operators from the initial set (P) and adding the difference to a third randomly selected lithospheric operator from the initial set (P). The goodness-of-fit of the synthetics using this second set (M) of lithospheric operators was measured. A pairwise comparison of the goodness-of-fit between the initial set (P) and the second set (M) was done to choose the operators from either set P or set M that gave a better fit. This new set of lithospheric operators (N - daughter) became the initial set (P) for the second generation/iteration. The process of generating a mutant set (M) and pairwise comparison set (N) continued until an optimum solution was found. This population based numerical optimizer is similar to the grid search method used by RS11, but allowed for testing multiple discontinuities without an exponential increase in computational time. Benefits of the differential evolution algorithm over grid search for a large number of parameters is well documented (Price et al., 2005).

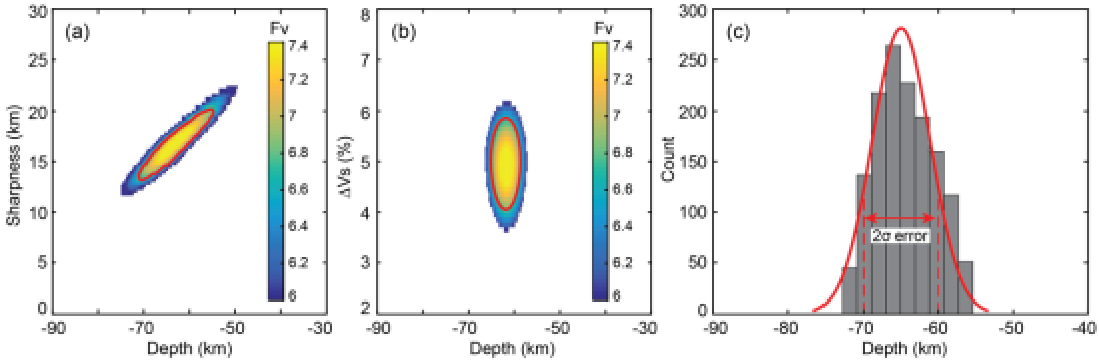

Figure 3.6: Visualization of tradeoff between different parameters of a lithospheric operator for an example bin 164. (a) tradeoff between depth of discontinuity and sharpness. (b) tradeoff between depth of discontinuity and percent velocity change. The red line demarcates the region of the best-fit solutions. (c) Histogram of discontinuity depths for models that are statistically significant as determined by F-test (Fv > 6.6 for bin 164).

An automated procedure determines the best-fitting model parameters using the differential evolution algorithm for each bootstrap sample in a bin. The error reported in the model parameters corresponds to the range of model parameters within the bootstrapped limits of the data. The error is determined by 95% confidence bounds, which corresponds to two standard deviations of the mean of the resulting variability in the bootstraps (Figure 3.6).

We test for the significance of model parameters beyond the attenuated reference stack using an F-test for significance of regression (Hosmer et al., 1997; Draper and Smith, 1998). The number of degrees of freedom in the data waveforms was determined using autocorrelation of an SS waveform generated using all of the waveforms in the 10° Pacific bins. We estimated 11 degrees of freedom in the data in the time window used in the inversions. Our final result resolves 4 model parameters for the single discontinuity (attenuation + 1 discontinuity), 7 model parameters for the double discontinuity (attenuation + 2 discontinuities) and 4 model parameters for the positive discontinuity (attenuation + 1 discontinuity). Since we include a constant oceanic crust of 7 km (section 3.3.4), the Moho corresponds to 1 fixed parameter. Each discontinuity corresponds to 3 free model parameters (depth, amplitude, and Gaussian width) and attenuation corresponds to 1 free model parameter (t^*). The effect of varying parameters (depth, amplitude and sharpness) on the models is illustrated in figure 3.5, and the trade-off between these model parameters is illustrated in figure 3.6.

The best-fitting model parameters were used to determine the depth, sharpness and amplitude of the velocity discontinuities. Operator amplitudes were scaled to velocity variation using the equation for SS reflection coefficient (Aki and Richards, 2009), assuming a constant mantle density of 3.38 g cm^{-3} and an incidence angle of 26.7 degrees. Although we use a constant density, we note that SS is affected by both density and velocity, and we do not have the ability to distinguish between the two. Similarly, depth was scaled from the delay time of the operator, which is a function of the two-way travel time between the discontinuity and the free surface (Aki and Richards, 2009). The depth scaling was done assuming a constant oceanic crustal thickness of 7 km, crustal velocity of 3.75 km/s, an upper mantle velocity of 4.55 km/s, and an average horizontal slowness of 0.12 s/km. We assumed a plane wave approximation for our calculations. Discontinuity depths were also estimated using the velocity model of (Nishimura and Forsyth, 1989), but there was no significant change (± 5 km) in the discontinuity depths compared to our depth estimates using a fixed crustal and mantle velocities. Discontinuity sharpness was governed by the width of the Gaussian operator and is reported as ± 1 standard deviation or twice the Gaussian half-width. Although the velocity change may occur over a total depth range of four times the Gaussian half-width.

Variation in the arrival time of the precursor phase from moveout for the range of event-to-station distances used here is minimal, having little effect on our result. The moveout on our deepest interpreted phase (120 km) for our 90 – 180 degrees epicentral distance range is < 3s (Figure 3.7). Furthermore, 95% of the waveforms in our stacks arrive from an epicentral distance of 90° – 150° (Figure 3.2), which only gives a ~1.6s difference in arrival time from moveout. This is much less than 1/4th of the dominant wave period (20s) used in our study. Therefore, while moveout may slightly affect our constraints on the sharpness of the discontinuities making them appear slightly more gradual, it does not significantly affect our ability to image the discontinuities < 120 km depth. In practice, the effect of moveout is incorporated within the error limits from the bootstrap.

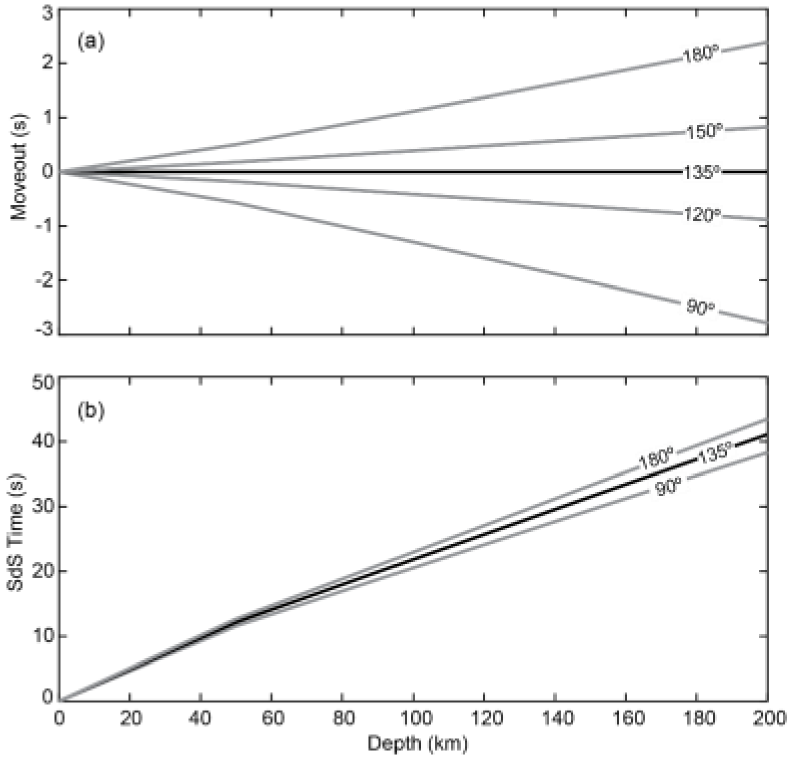

Figure 3.7: Effect of moveout in seconds for SS waveform at different source – receiver offsets. (a) Moveout in seconds for SS. (b) Differential travel time prior to SS phase for various depth and epicentral distances (labeled on curves). Reference distance of 135 ° was used to calculate moveout. The moveout for a discontinuity at 120 km is < 3s, which is less than dominant period of our data, 20s.

3.3.5.1 Optimization

The differential evolution algorithm has two parameters that control the speed of convergence on the optimum solution, the mutation rate and the selection rate. The mutation rate, also called the scaling factor (F), controls the generation of lithospheric operators in the mutant set (M). The scaling factor is a value from within the range (0,1]. A scaling factor value close to 0 produces a mutant set that is near to the parent set. As the scaling factor value increases, the mutant set moves farther away from the parent set. Higher scaling factors are generally chosen when the model space is large. The optimal value of the scaling factor is determined by trial and error. In this approach, a synthetic seismogram is modeled with a known discontinuity for different values of the scaling factor. The optimal scaling factor is the value for which the least number of iterations are required to converge on the known solution. An optimum scaling factor of 0.3 is used for the SS precursor modeling presented in this thesis.

The selection rate, also called the crossover probability (Price and Storn, 1997; Storn and Price, 1997; Price et al., 2005), was used to complement the evolution search strategy. The crossover probability is a user defined value from within the range [0,1] that controls the fraction of lithospheric operators selected from the mutant set to the daughter set (N). A uniform random number generator is used to determine if a given lithospheric operator is selected from the mutant set, assuming the mutant operator has a better fit than the corresponding lithospheric operator from the parent set. If the generated random number is less than or equal to the crossover probability, the lithospheric operator from the mutant set is copied to the daughter set (N). If the generated random number is greater than the crossover probability, the lithospheric operator from the parent set is copied to the daughter set. The crossover probability ensures that each lithospheric operator, regardless of its location in the parent or mutant set, has the same probability of being inherited to the daughter set (Syswerda, 1989). A trial and error approach was used to determine an optimum crossover probability of 0.3.

3.4 Results

We resolve lithospheric discontinuity structure in 82 out of 91 bins in the Pacific with significantly increased lateral coverage across the Pacific than in previous studies (Figure 3.8) (Rychert and Shearer, 2011; Schmerr, 2012). We image a pervasive negative discontinuity, i.e. velocity decrease with depth, at

30 – 80 km depth in 64 bins. We also image some complexities; locations with a shallow positive discontinuity (20 – 36 km), locations with no discontinuities, and locations where the negative gradient continues to greater depth.

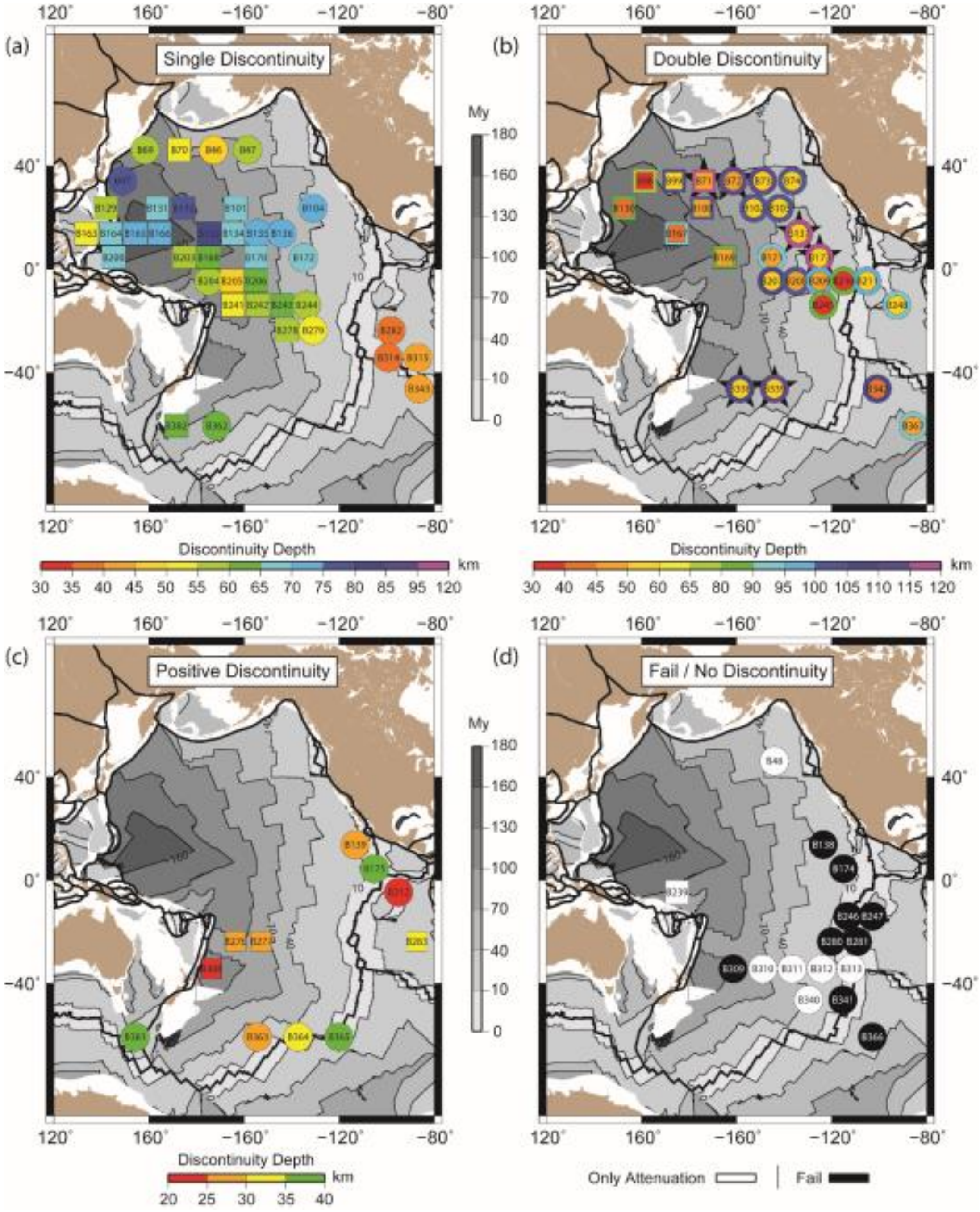

Figure 3.8: Pacific 10° SS bouncepoint bins with discontinuity depths. Numbers within the symbols indicate Pacific bin numbers. Colored circles and squares

correspond to discontinuity depths for normal and anomalous lithosphere respectively for (a) single discontinuity (b) double discontinuity (c) positive discontinuity. Overlapping circles and squares in (b) correspond to double discontinuity with the outer color showing depth of deeper discontinuity and inner circle showing depth of shallow discontinuity. Six bins encircled by black stars indicate explicit double discontinuity. (d) white bins require only attenuation to fit the data. Black bins could not be resolved. Depth scales are different for maps (a, b and c). Background colors show seafloor age with age contours (thin black lines) at an interval of 30 My (Müller et al., 2013). Thick black lines represent plate boundaries (Bird, 2003).

3.4.1 Shallow, Positive Discontinuity

We resolve a positive discontinuity in 11 out of 91 bins in the Pacific, 8 of which sample relatively young < 30 My lithosphere and 3 bins sample > 90 My lithosphere (Figure 3.8c, Table 3.1). The results here do not include an oceanic Moho at 7 km depth. Once we established these 11 bins required a shallow positive discontinuity, we took out the Moho at 7 km depth that was assumed for the rest of the bins, since these shallow positive discontinuities may represent thickened crust. However, including an oceanic Moho at 7 km depth had no significant effect on our results. The discontinuity is quite sharp at depths ranging from 20 – 36 km and velocity contrast of 2 – 15% (average velocity contrast of 8%). We do not resolve any positive discontinuities at depths greater than 36 km. Waveform fits for the positive discontinuity are shown in figure 3.9.

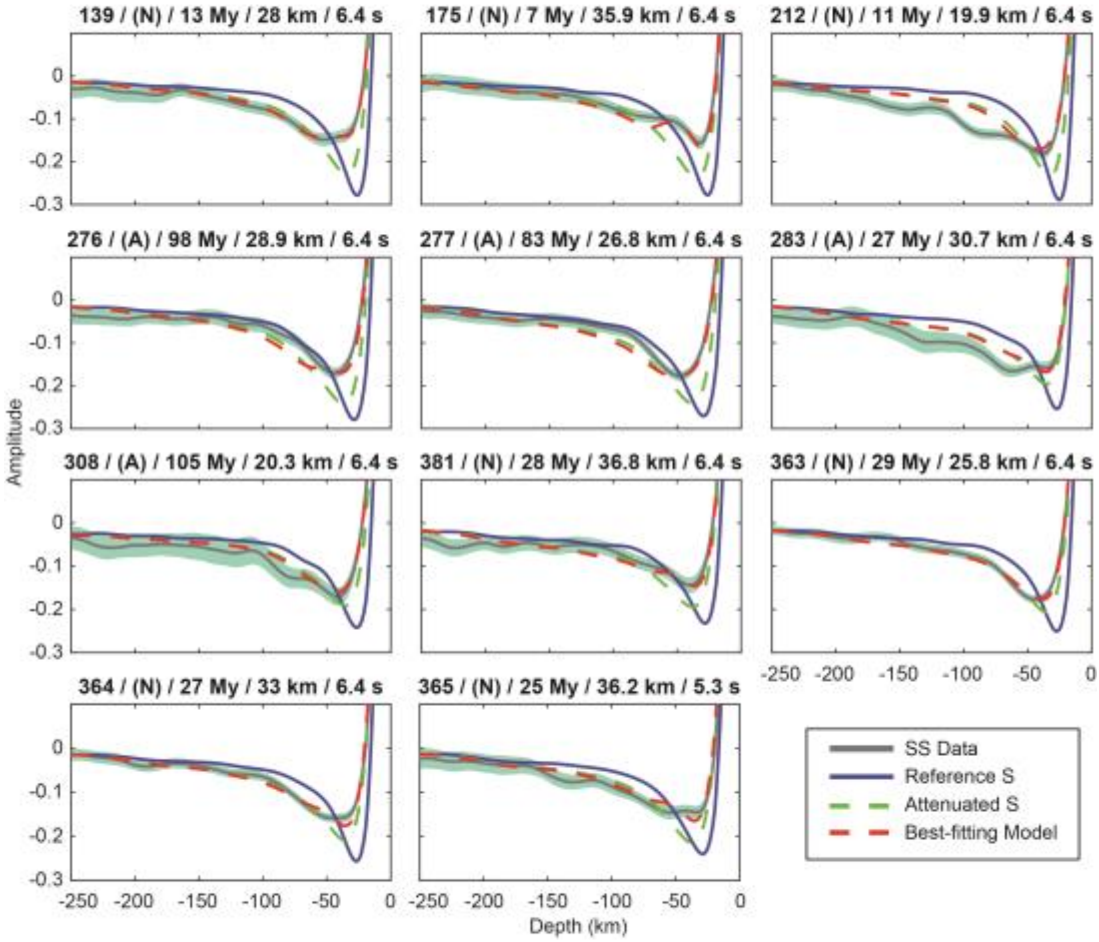

Figure 3.9: Waveforms showing fit of best-fitting model (dashed red) with the data (solid grey) for positive discontinuity. Solid blue line is the weighted reference S wave corresponding to each bin and dashed green line is the attenuated S wave. Shaded region indicates 2 standard deviation error in the data. The header for each plot shows the bin numbers from figure 3.8, normal or anomalous lithosphere (N/A), age in My, depth of discontinuity in km and attenuation in seconds.

Table 3.1: Positive Discontinuity Results for Individual Bouncepoint Bins

Bin	Type	Lon	Lat	Bounces	Age ($My^{1/2}$)	Depth (km)	Depth Bounds (km)	Amplitude (%)	Sharpness (km)	Attenuation (s)	Interpretation
139	N	-113	15	421	4	28	25 - 32	14	2	6.4	Moho
175	N	-105	5	370	3	36	35 - 39	15	2	6.4	Moho
212	N	-95	-5	483	3	20	19 - 24	5	2	6.4	Attenuation
276	A	-163.6	-25	304	10	29	25 - 33	7	2	6.4	Moho
277	A	-152.7	-25	380	9	27	24 - 30	10	2	6.4	Moho
283	A	-87.3	-25	345	5	31	28 - 34	2	2	6.4	Moho
308	A	-173.8	-35	292	10	20	19 - 24	3	2	6.4	Moho
381	N	154.3	-55	369	5	37	35 - 39	5	2	6.4	Moho
363	N	-154.3	-55	523	5	26	23 - 30	3	2	6.4	Attenuation
364	N	-137	-55	506	5	33	29 - 35	3	2	6.4	Attenuation
365	N	-120	-55	361	5	36	32 - 38	5	0	5.3	Moho

Bins marked "N" represent predominantly normal oceanic crust and those marked "A" represent predominantly anomalous oceanic crust (Korenaga and Korenaga, 2008). Depth scaling is described in section 3.3.5. We do not include a 7 km oceanic crust for modeling these bins. Amplitude refers to the shear velocity drop (percent) in depth. Sharpness refers to width of the Gaussian operator, represented by $\pm 1\sigma$ *i.e. two times the Gaussian half width.*

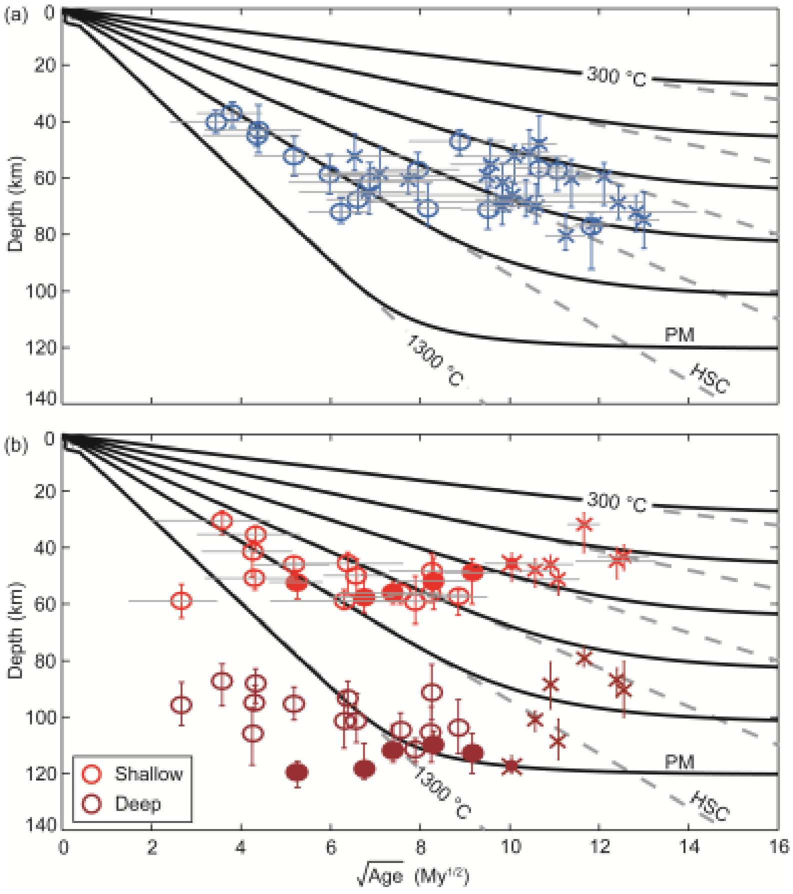

Figure 3.10: Discontinuity depth versus square root of seafloor age for (a) single discontinuity and (b) double discontinuity. Circles and crosses represent normal and anomalous lithosphere respectively. Darker circles and crosses in (b) show depths of

deeper discontinuity. Symbols with filled colors indicate bins with explicit double discontinuity. The remaining 20 bins could be equally well fit with a skewed Gaussian operator. The solid black lines show plate model (PM) [Stein and Stein, 1992], assuming a potential temperature of 1350°C and a plate velocity of 60 mm/yr, isotherms from 300°C to 1300°C at an interval of 200 °C. Dashed grey lines show half-space cooling (HSC) model isotherms from 300°C to 1300°C. Horizontal error bars in (a) and (b) represent the age of seafloor to one standard deviation in each bouncepoint bin. Vertical error bars indicate 95% confidence bounds on depth range.

3.4.2 Pervasive Negative Discontinuity

We resolve a single sharp negative discontinuity in 64 bins, 38 of which require a single negative discontinuity (Figure 3.8a, 3.10a, Table 3.2) and 26 of which require a shallow and a deeper negative discontinuity (Figure 3.8b, 3.10b, Table 3.3). Here we discuss the shallow pervasive discontinuity, i.e. the best-fit depth from 38 single discontinuity bins and the shallow discontinuity depth from the 26 double discontinuity bins as a single result. The depth of the shallow discontinuity varies from 30 – 72 km according to the conductive cooling model until 36 My along a 1100 °C thermal contour. We use a piecewise linear fit to the age–depth data to estimate the breakpoint where there is a change in slope in the data. The inversion yields a breakpoint of 36 ± 9 My with a slope of 8.9 ± 4.7 km/My$^{1/2}$ from 0 – 36 My and -0.4 ± 2.7 km/My$^{1/2}$ from 36 – 180 My. Error bars indicate 2 sigma variation. There is no age dependence after ~36 My and the discontinuity appears to flatten in the depth range of 43 – 80 km, an average depth of 60 km (Figure 3.10) and a 1.5 km standard error of the mean. Waveform fits to the data for bins with a single negative discontinuity are shown in figure 3.11 and for bins with double discontinuity are shown in figure 3.12. The discontinuity is sharp with velocity contrast of 3 – 15 %, an average velocity contrast of 7 ± 2% occurring over < 21 km (Table 3.2, 3.3). Some bins require a wide Gaussian operator that suggests the velocity contrast occurs over a greater depth range and/or the lithospheric thickness varies laterally in the sampled region. Although we use a piecewise liner fit to determine the breakpoint age in our data, 36 ± 9 My, there is strong correlation between the depth and square root of seafloor age < 50 My, at 0.68 (including bin 211) and 0.82 (excluding bin 211).

Table 3.2: Single Discontinuity Results for Individual SS Bouncepoint Bins

Bin	Type	Lon	Lat	Bounces	Age ($My^{1/2}$)	Depth (km)	Depth Bounds (km)	Amplitude (±2%)	Sharpness (±4 km)	Attenuation (s)
46	N	-172.8	45	2883	9	47	43 - 52	6	19	4.0
47	N	-158.4	45	1839	8	57	51 - 68	14	16	4.1
69	N	158.4	45	1943	11	58	53 - 65	6	10	3.4
70	A	172.8	45	3055	10	52	48 - 62	5	20	4.0
97	N	148.9	35	1256	12	77	72 - 92	7	10	3.8
101	A	-163.6	25	4532	10	70	69 - 72	12	10	6.0
104	N	-130.9	25	644	6	72	67 - 76	9	9	5.0
129	A	141.8	25	1102	9	59	54 - 64	10	22	3.0
131	A	163.6	25	1023	12	69	63 - 75	4	15	3.0
132	A	174.5	25	1795	12	76	74 - 79	13	10	4.5
133	A	-174.8	15	1755	11	81	73 - 86	14	10	4.4
134	A	-164.6	15	3203	11	70	62 - 76	15	8	6.0
135	N	-154.3	15	3540	10	71	66 - 78	9	11	6.0
136	N	-144	15	2748	8	71	62 - 77	3	13	6.0
163	A	133.7	15	969	7	52	44 - 57	11	16	3.3
164	A	144	15	816	10	66	61 - 70	4	18	3.7
165	A	154.3	15	987	13	72	66 - 79	3	17	3.0
166	A	164.6	15	1018	13	75	65 - 85	5	9	3.0
168	A	-175	5	392	11	60	53 - 70	3	10	3.0
170	A	-155	5	1093	10	68	62 - 77	3	11	5.9
172	N	-135	5	1016	7	68	61 - 73	5	9	5.8
200	A	145	5	586	10	69	61 - 74	14	21	4.5
203	A	175	5	459	12	60	55 - 70	9	14	3.9
204	N	-175	-5	290	11	57	47 - 67	12	12	3.2
205	A	-165	-5	571	11	48	38 - 58	6	9	3.0
206	A	-155	-5	1091	10	62	55 - 70	6	13	4.4
241	A	-164.5	-15	532	10	51	43 - 59	9	9	4.5
242	A	-154.3	-15	853	10	55	46 - 63	9	16	4.4
243	A	-144	-15	893	8	61	59 - 66	4	17	5.6
244	N	-133.7	-15	835	6	59	52 - 66	15	10	4.5
278	A	-141.8	-25	526	7	58	49 - 66	12	15	6.0
279	N	-130.9	-25	491	5	52	45 - 59	7	9	3.0
282	N	-98.2	-25	295	4	37	33 - 42	4	5	3.0
314	N	-99.3	-35	284	3	40	36 - 44	9	6	5.2
315	N	-86.9	-35	302	4	45	41 - 49	13	9	3.3
343	N	-86.4	-45	289	4	43	34 - 51	13	9	3.3
362	N	-171.4	-55	486	7	61	54 - 68	12	20	6.0
382	A	171.4	-55	356	7	65	57 - 73	6	19	6.0

Bins marked "N" represent predominantly normal oceanic crust and those marked "A" represent predominantly anomalous oceanic crust (Korenaga and Korenaga, *2008). Depth scaling is described in section 3.3.5. These bins include a 7 km thick oceanic crust as described in section 3.3.5. Amplitude refers to the shear velocity drop (percent) in depth. Sharpness refers to width of the Gaussian operator, represented by* $\pm 1\sigma$ *i.e. two times the Gaussian half width.*

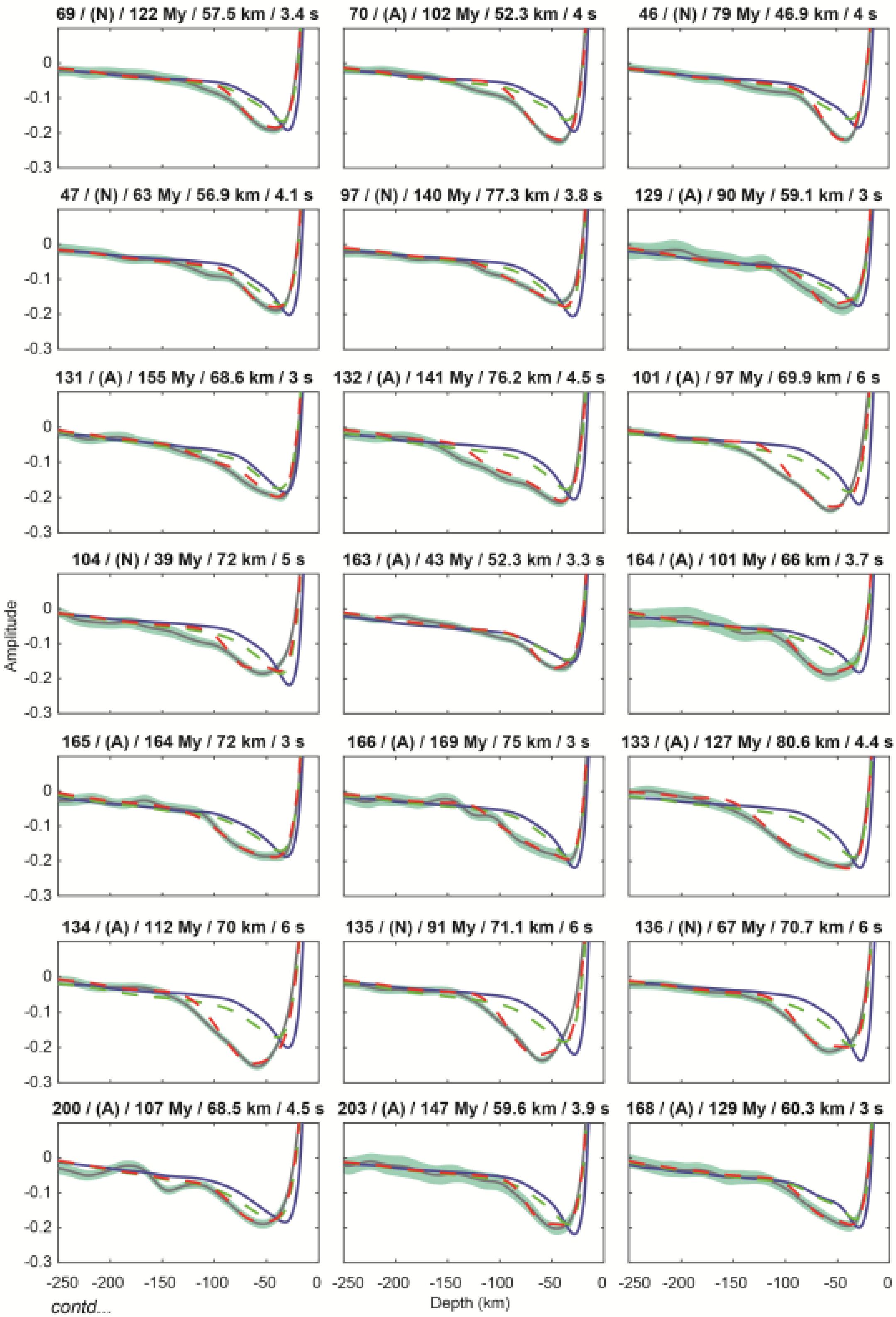

contd...

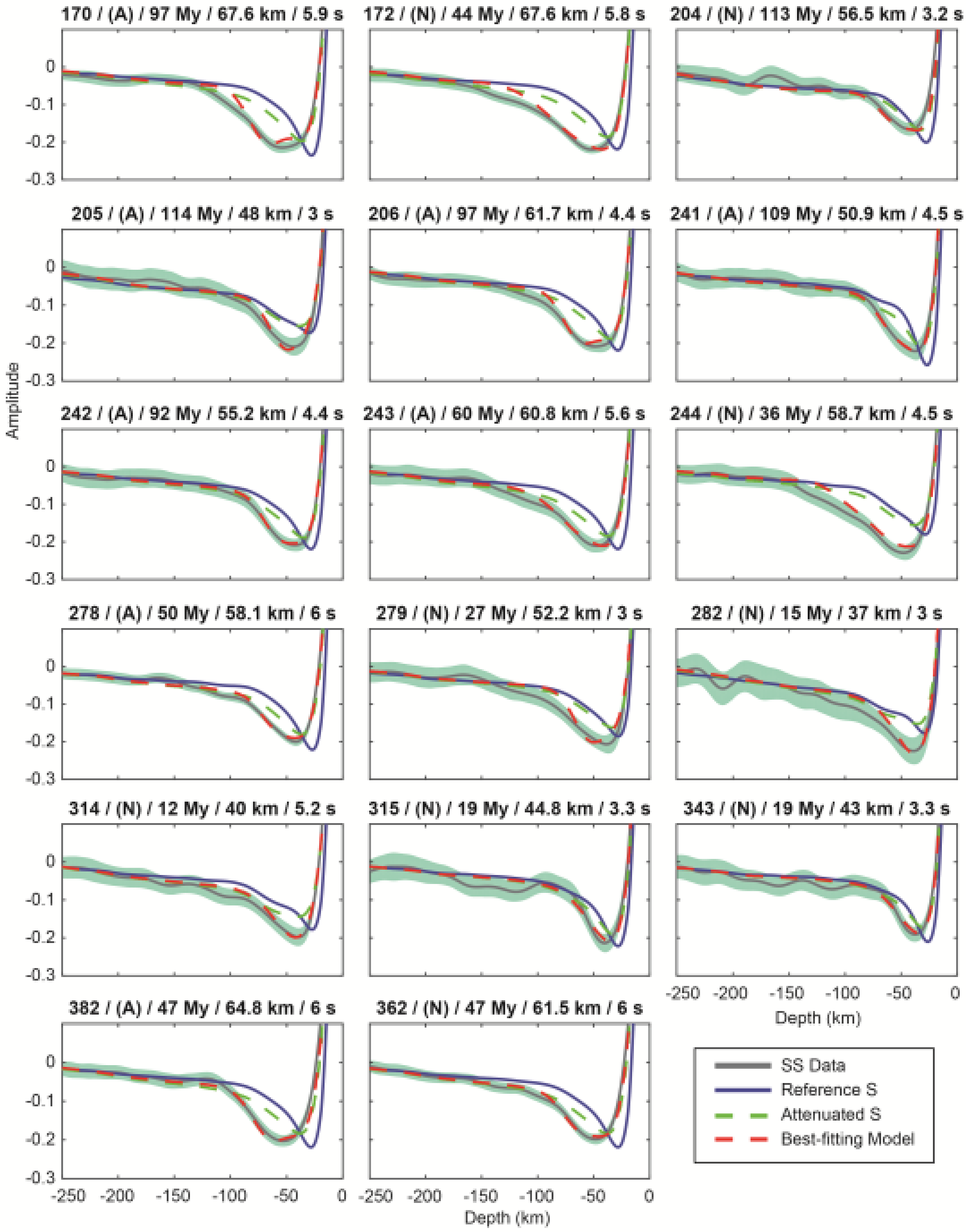

Figure 3.11: Waveforms showing fit of best-fitting model (red-dashed) with the data (solid grey) for single discontinuity. Solid blue line is the weighted reference S wave corresponding to each bin and dashed green line is the attenuated S wave. Shaded region indicates 2 standard deviation error in the data. The header for each plot shows the Pacific bin identifier from figure 3.8, normal or anomalous lithosphere (N/A), age in My, depth of discontinuity in km and attenuation in seconds.

Table 3.3: Double Discontinuity Results for Individual SS Bouncepoint Bins

Bin	Type	Lon	Lat	Bounces	Age ($My^{1/2}$)	Depth 1 (km)	Depth Bounds (km)	Amplitude 1 (±2%)	Sharpness 1 (±3 km)	Depth 2 (km)	Depth Bounds (km)	Amplitude 2 (±1%)	Sharpness 2 (±3 km)	Attenuation (s)
71*	A	-173.8	35	2936	10	46	42 - 52	4*	5*	118	114 - 120	5*	7*	5.7*
72*	N	-161.4	35	2731	9	49	44 - 60	5*	7*	113	106 - 120	3*	2*	4.3*
73	N	-149	35	1367	8	59	50 - 67	4	0	112	108 - 116	5	8	6.0
74	N	-136.6	35	448	6	59	55 - 62	10	6	101	91 - 111	3	2	4.9
98	A	161.4	35	1241	12	32	28 - 42	6	10	79	75 - 82	3	5	5.1
99	A	173.8	35	2857	11	51	48 - 57	5	9	109	101 - 115	4	3	3.7
100	A	-174.5	25	2856	11	48	44 - 54	5	8	101	98 - 105	7	10	3.7
102	N	-152.7	25	2667	9	57	55 - 64	5	10	104	94 - 113	2	2	5.2
103	N	-141.8	25	1381	8	56	52 - 60	5	8	105	99 - 113	2	2	5.3
130	A	152.7	25	678	12	45	40 - 51	9	6	87	83 - 93	3	2	4.5
137*	N	-133.7	15	1455	7	57	49 - 63	4*	6*	118	109 - 122	3*	2*	5.3*
167	A	174.9	15	695	13	43	39 - 48	4	2	90	80 - 100	6	5	5.0
169	A	-165	5	642	11	46	43 - 49	7	9	89	81 - 97	3	2	3.9
171	N	-145	5	2116	8	48	42 - 55	11	15	91	81 - 101	2	2	6.0
173*	N	-125	5	830	5	52	48 - 58	4*	6*	120	116 - 125	4*	5*	3.0*
207	N	-145	-5	1235	8	57	55 - 59	6	4	105	96 - 116	4	5	3.0
208	N	-135	-5	1619	7	50	44 - 59	4	5	102	92 - 109	8	10	5.4
209	N	-125	-5	927	5	46	43 - 48	7	8	95	89 - 101	3	2	3.7
210	N	-115	-5	647	4	30	27 - 35	5	5	87	81 - 96	7	11	3.0
211	N	-105	-5	689	3	59	53 - 65	4	6	96	88 - 103	5	3	3.0
245	N	-123.4	-15	514	4	35	32 - 41	4	5	88	83 - 95	6	5	3.0
248	N	-92.6	-15	649	4	51	48 - 55	4	11	95	89 - 97	3	2	5.5
338*	N	-158	-45	580	8	52	44 - 62	9*	10*	110	105 - 113	2*	2*	4.4*
339*	N	-144	-45	749	7	56	52 - 60	11*	8*	112	103 - 116	3*	2*	6*
342	N	-100.8	-45	324	4	41	37 - 50	13	10	106	97 - 117	3	40	4.1
367	N	-85.7	-55	295	6	46	42 - 57	6	8	93	87 - 100	2	2	4.8

Bins marked "N" represent predominantly normal oceanic crust and those marked "A" represent predominantly anomalous oceanic crust (Korenaga and Korenaga, 2008). Depth scaling is described in section 3.3.5. These bins include a 7 km thick oceanic crust as described in section 3.3.5. Depth 1, Amplitude 1 and Sharpness 1 refers to the shallow discontinuity and Depth 2, Amplitude 2 and Sharpness 2 refers to the deeper discontinuity. Both shallow and deeper discontinuities are of negative sign i.e. velocity decrease with depth. Amplitude refers to the shear velocity drop (percent) in depth. Sharpness refers to width of the Gaussian operator, represented by ±1σ *i.e. two times the Gaussian half width.*

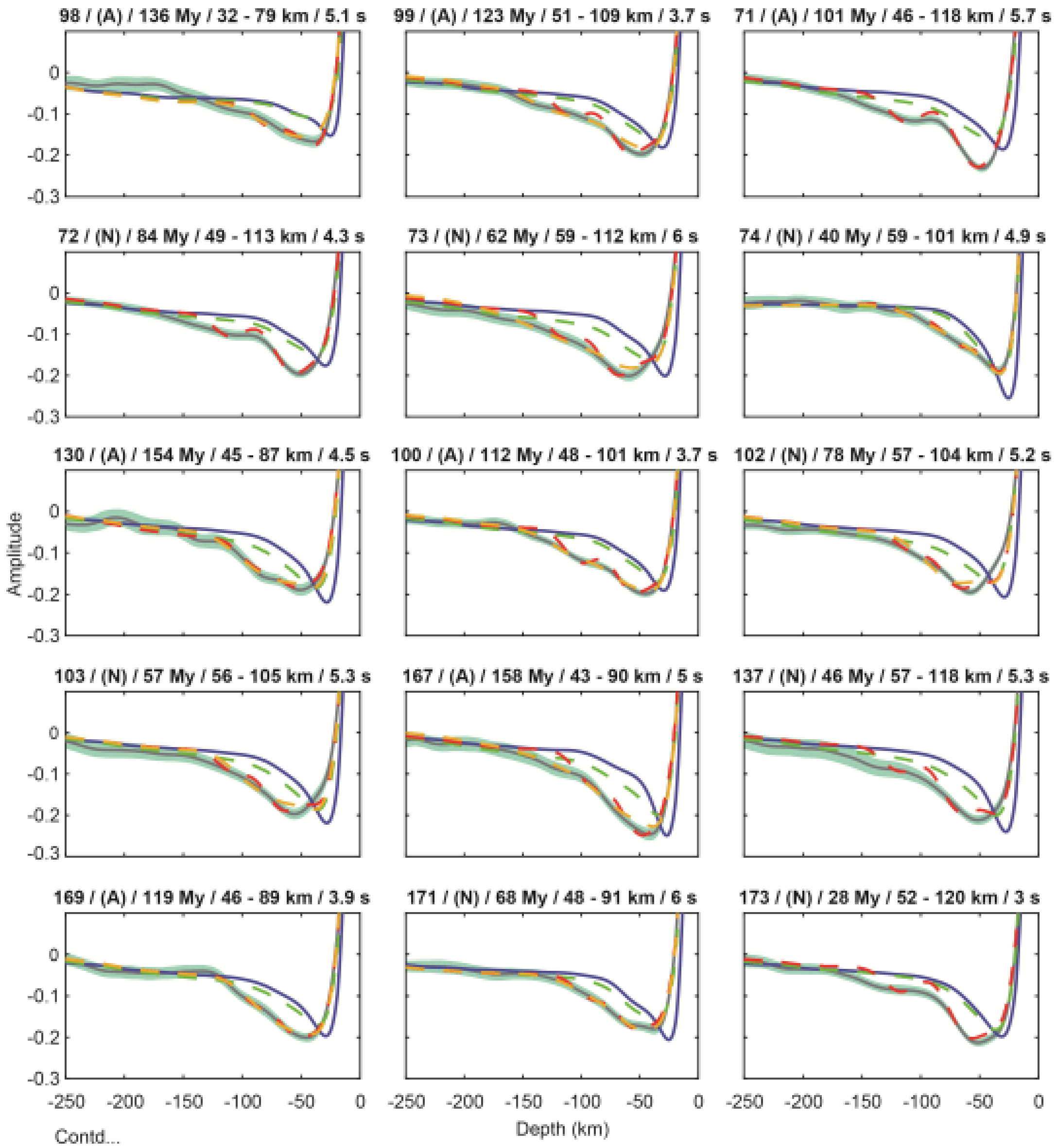

Contd...

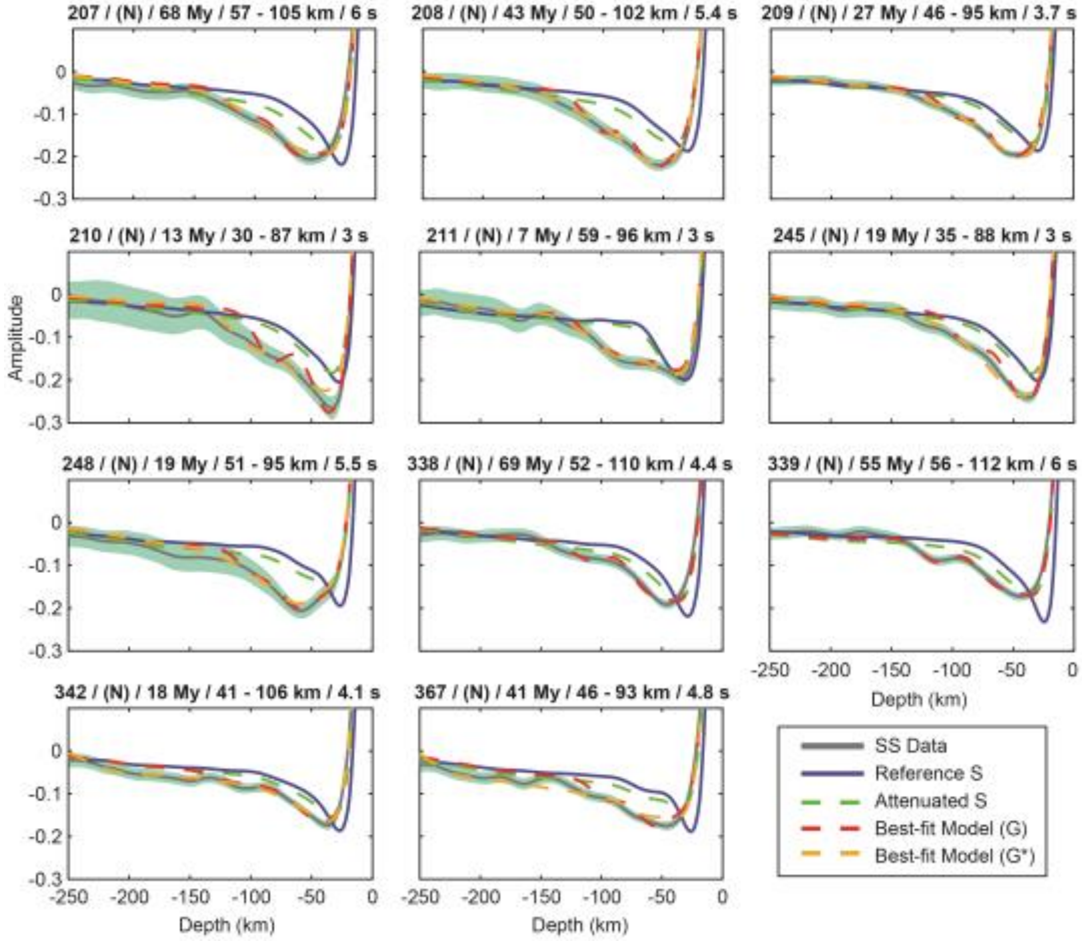

Figure 3.12: Waveforms showing fit of best-fitting model using both Gaussian (dashed red) and skewed Gaussian (dashed yellow) operators with the data (solid grey) for bins with double discontinuity. Solid blue line is the weighted reference S wave corresponding to each bin and dashed green line is the attenuated S wave. Shaded region indicates 2 standard deviation error in the data. The header for each plot shows the bin numbers from figure 3.8, normal or anomalous lithosphere (N/A), age in My, depth of shallow - deep discontinuity in km and attenuation in seconds.

3.4.3 Resolution of the Shape of the Velocity Gradient

In the 26 bins described above, a deeper negative discontinuity at 80 – 120 km depth is required along with a shallow negative discontinuity to fit the data. We could not resolve any bin that requires a shallow positive and a deeper negative or vice versa. Further, we tested to see if two negative discontinuities could be replaced by a single discontinuity with a large Gaussian width. Only bin 98 could be resolved with a simple single wide Gaussian operator but has a statistical better fit with the data using a double negative discontinuity. One reason a single wide Gaussian operator cannot easily replace two discontinuities is that interference at shallow depth with the main SS pulse causes a bad fit. This can be avoided with irregularly shaped pulses, which we also tested.

We could fit 20 bins with a single skewed Gaussian operator out of 26 bins that have double discontinuity. Only 6 (Bins 71, 72, 137, 173, 338, 339) could not be resolved and require a double discontinuity (Figure 3.10). These 6 bins also have the appearance of a double pulse (Figure 3.12). The skewed functions for the double discontinuity bins are best-fit with a sharp Gaussian at shallow depths, followed by a rectangular function and a gradual Gaussian tail at the end (Figure 3.13). In most cases the models converge to a solution where there is a sharp discontinuity at shallow depths followed a more gradual tail (large Gaussian width).

The skewed operator test suggests that while we can resolve the existence of velocity discontinuities, there is some uncertainty in the exact shape. We cannot distinguish between two sharp discontinuities and two sharp discontinuities with a linear gradient (skewed Gaussian) between them (Figure 3.14). We report the depths of the asymmetric operators as both the maximum amplitude (hereafter referred to as SG depths) and as the depth of half the total velocity drop (hereafter referred to as CDF depths). In case of bins with a single discontinuity, we did not find any significant change in discontinuity depths when skewed Gaussian operators were used (Figure 3.15). The CDF depths are < ± 3 km and SG depths are < ± 6 km compared to

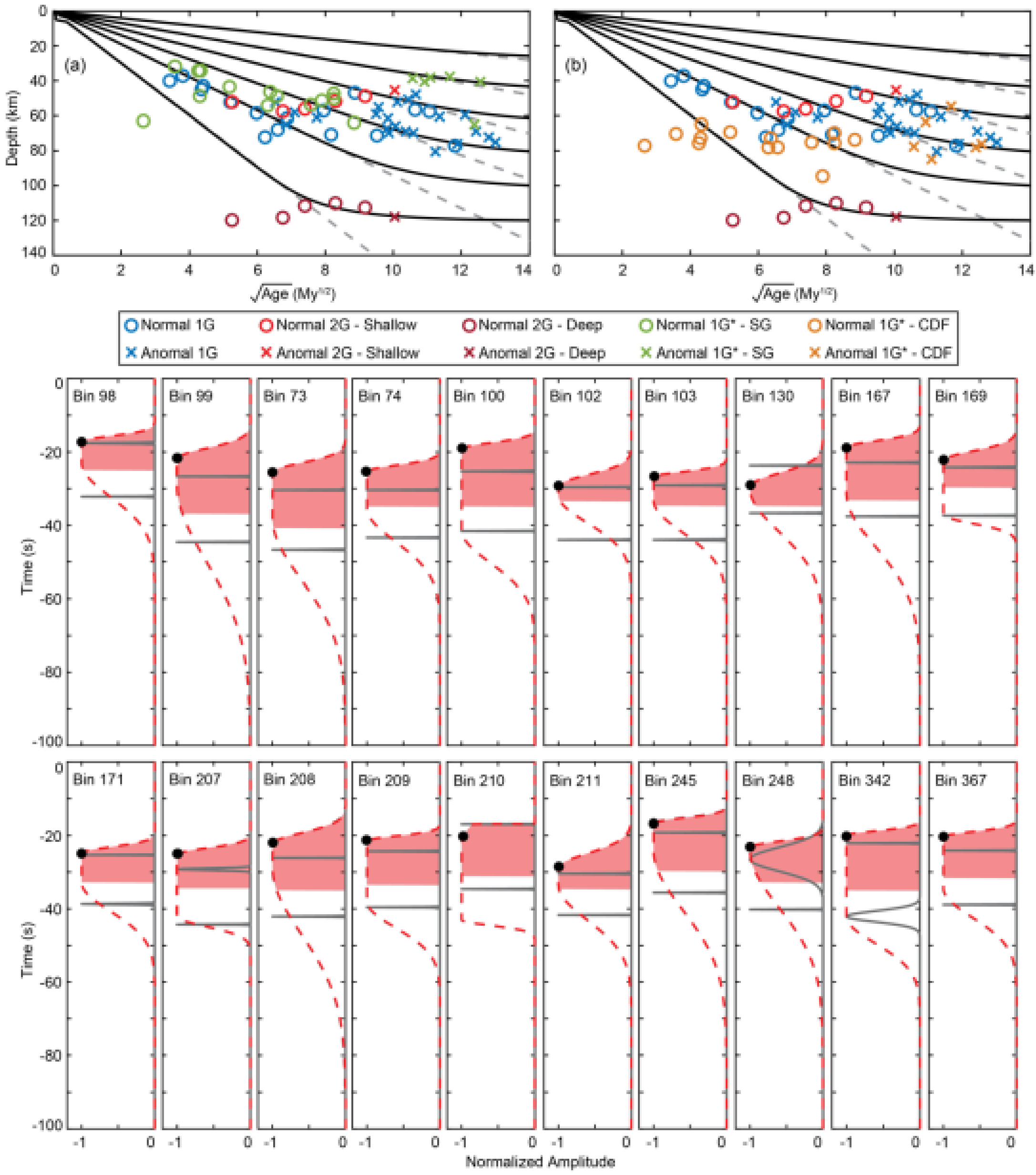

Figure 3.13: Discontinuity depth results for bins with double discontinuity modeled using a skewed Gaussian operator. The SG depths are plotted in (a) and CDF depths in (b). The bottom panels show bins that could be equally well fit by a skewed Gaussian operator (dashed red) or a double discontinuity (two Gaussian) operator (solid grey). The black circle shows the delay time at which SG depths are calculated. The red shaded area is used to calculate the CDF depths. "Normal" and "Anomal" refers to normal and anomalous bins (Table 3.3). "G" represents a Gaussian and "G" represents a skewed Gaussian operator. Numbers "1" and "2" represents the number of operators used.*

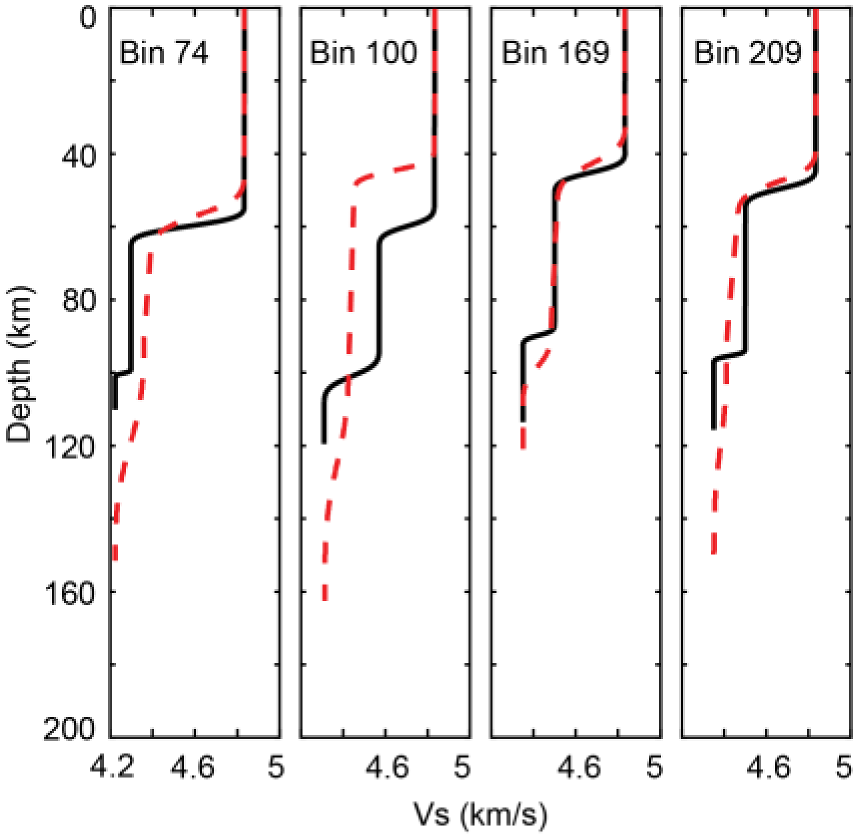

Figure 3.14: Examples of velocity – depth profiles corresponding to Gaussian (solid black) and skewed Gaussian (dashed red) discontinuity operators from figure 3.13.

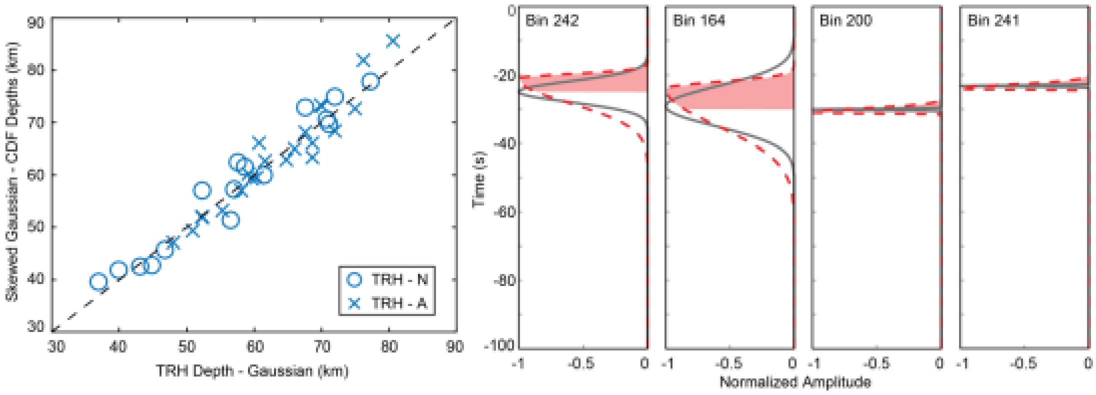

Figure 3.15: Discontinuity depths (bins with single discontinuity, Table 3.2) modeled using Gaussian functions compared to CDF depths from skewed Gaussian operators. Panels on the right show 4 examples of a Gaussian (grey) and skewed Gaussian (dashed red) operators that were used to model bins with a single discontinuity.

discontinuity depths calculated using symmetric Gaussian functions. In case of bins with a double discontinuity the fits to the data using skewed Gaussian operators are statistically similar or better in some cases compared to the fits to the data using two Gaussian operators (Figure 3.16). The SG depths are < ± 5 km compared to the previously reported shallow discontinuity from the double discontinuity bins and shows similar age-depth trend (Figure 3.13a). But the CDF depths are much deeper, generally occurring midway between the shallow and deeper discontinuity (Figure 3.13b). The CDF depths are in the range of 55 – 90 km, average depth of ~75 km, and show no apparent age dependency. The SG depths are probably the most important since SS is most sensitive to the depth of the strongest and sharpest velocity change.

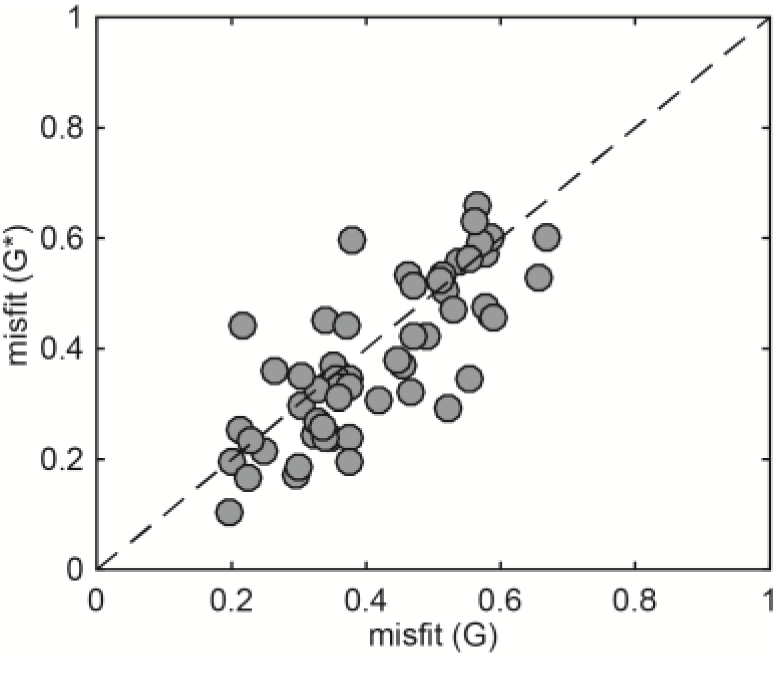

Figure 3.16: Comparison of misfit between discontinuities modeled using Gaussian (G) and skewed Gaussian (G) operators, for bins with both single (Figure 3.8a) and double discontinuity (Figure 3.8b). The misfit function is calculated as the normalized root mean squared error in the time window 0 to 150s prior to the SS phase.*

3.4.4 No Discontinuity and Failed Bins

Nine bins could not be resolved at all owing to small number of waveforms and/or noise (Table 3.4). Seven bins could be modeled with attenuation alone, allowing a maximum attenuation of 6.4 s, and required no additional discontinuity (Figure 3.8d, Table 3.4). Waveform fits to the data are shown in figure 3.17.

Table 3.4: Bins with No Discontinuity and Failed Bins

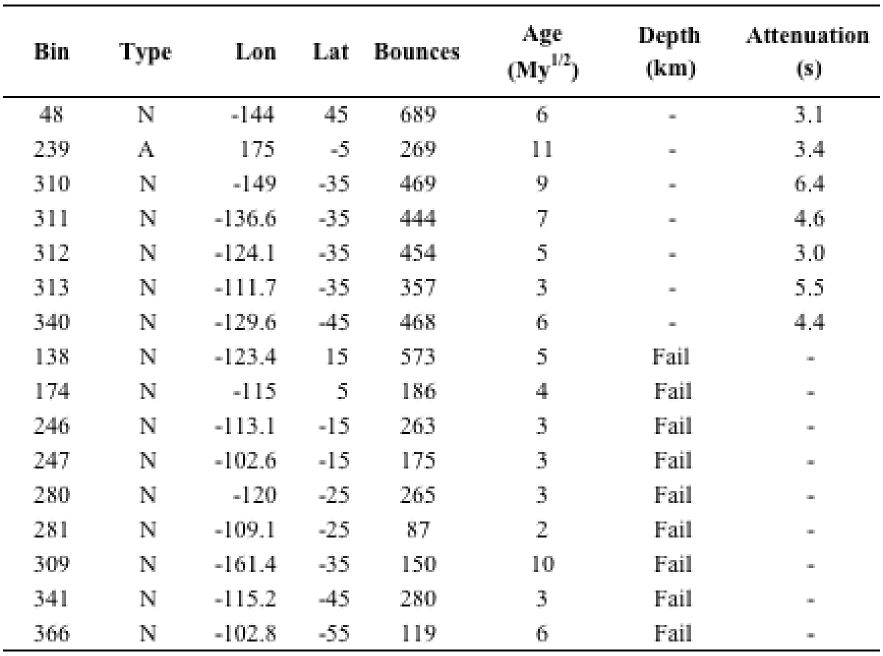

Bin	Type	Lon	Lat	Bounces	Age ($My^{1/2}$)	Depth (km)	Attenuation (s)
48	N	-144	45	689	6	-	3.1
239	A	175	-5	269	11	-	3.4
310	N	-149	-35	469	9	-	6.4
311	N	-136.6	-35	444	7	-	4.6
312	N	-124.1	-35	454	5	-	3.0
313	N	-111.7	-35	357	3	-	5.5
340	N	-129.6	-45	468	6	-	4.4
138	N	-123.4	15	573	5	Fail	-
174	N	-115	5	186	4	Fail	-
246	N	-113.1	-15	263	3	Fail	-
247	N	-102.6	-15	175	3	Fail	-
280	N	-120	-25	265	3	Fail	-
281	N	-109.1	-25	87	2	Fail	-
309	N	-161.4	-35	150	10	Fail	-
341	N	-115.2	-45	280	3	Fail	-
366	N	-102.8	-55	119	6	Fail	-

Bins marked "N" represent predominantly normal oceanic crust and those marked "A" represent predominantly anomalous oceanic crust (Korenaga and Korenaga, 2008). Bins that have no depth value require no additional discontinuity and can be fit with attenuation alone. Bins marked "Fail" are noisy and have insufficient waveforms.

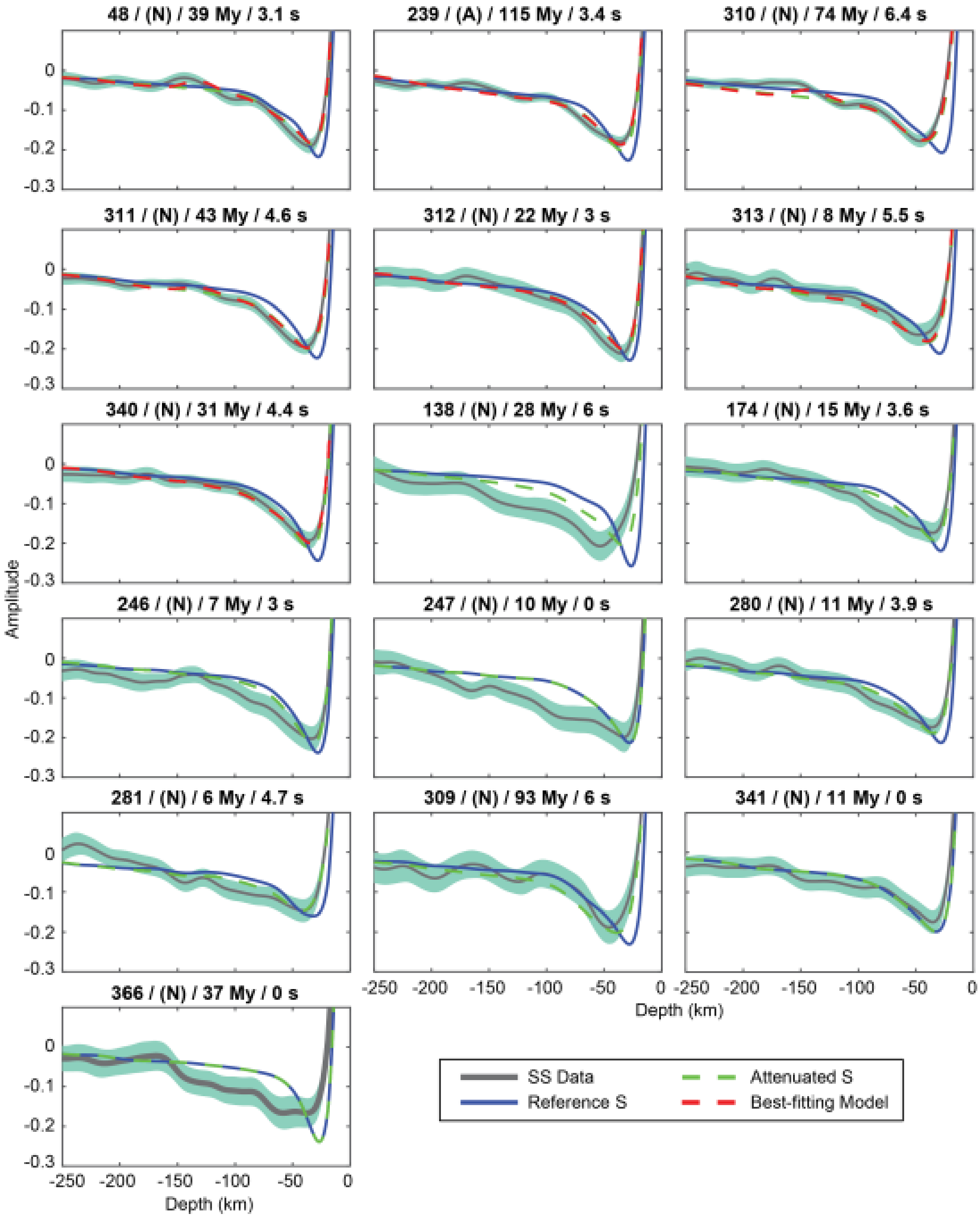

Figure 3.17: Bins marked "N" represent predominantly normal oceanic crust and those marked "A" represent predominantly anomalous oceanic crust (Korenaga and Korenaga, 2008). Bins that have no depth value require no additional discontinuity and can be fit with attenuation alone. Bins marked "Fail" are noisy and have insufficient waveforms.

3.5 Discussion

3.5.1 Shallow, Positive Discontinuity

Resolution of the shallowest discontinuities (< 30 km) is difficult since phases arrive very close to the main SS phase and can trade off with the attenuation operator. We investigate this trade-off for the shallow positive discontinuities. We typically allow attenuation operators of 3 – 6 s in our inversions (section 3.3.4), but all bins with a positive discontinuity are better fit with a larger attenuation operator (Table 3.1). If we allow a maximum attenuation of 6.4 s, only 8 of 11 bins require a positive discontinuity, although the depth and sharpness constraints in these bins remain unchanged.

Several of our bins with a shallow, positive discontinuity are located in regions that have been altered by volcanism, and may represent a thickened crust (marked as "Moho" in Table 3.1). For example, bins 276 and 277 sample the Manihiki Plateau, and bin 308 samples the Hikurangi plateau. Manihiki and Hikurangi plateaus are thought to have been part of a much larger Ontong Java super plateau that formed due to a massive volcanic event 120 My ago (Taylor, 2006). The ~25 km thick crust that we image is consistent with previous crustal thickness estimates of 15 – 25 km from seismic reflection survey and gravity modelling (Davy and Wood, 1994; Davy et al., 2008). Bin 175 samples the Galapagos archipelago and the thicker crust, ~35 – 40 km, that we image is consistent with receiver function study in the region that has reported a velocity increase at 37 ± 7 km depth (Rychert et al., 2014a). Bin 283 is near the eastern hotspot track/Nazca Ridge and may reflect thickened crust. The positive discontinuity in bin 139 can be explained by its proximity to the southern margin of the North American continent which has a crustal thickness of 20 – 35 km (Laske et al., 2012), sampled by the large Fresnel zone (~10°) of the SS. Finally, bins 365 and 381 are both located on mid-ocean ridges, but require a positive discontinuity at 36 and 37 km depth even if very high attenuation (6.8s) is assumed. If very large attenuation of > 6.8s is allowed, five (bins 212, 283, 308, 363, 364) out of 11 bins require no additional discontinuity (Figure 3.18), four (212, 363 363, and 364) that are located near mid-ocean ridges and might be characterized by higher than average attenuation (Dalton et al., 2008).

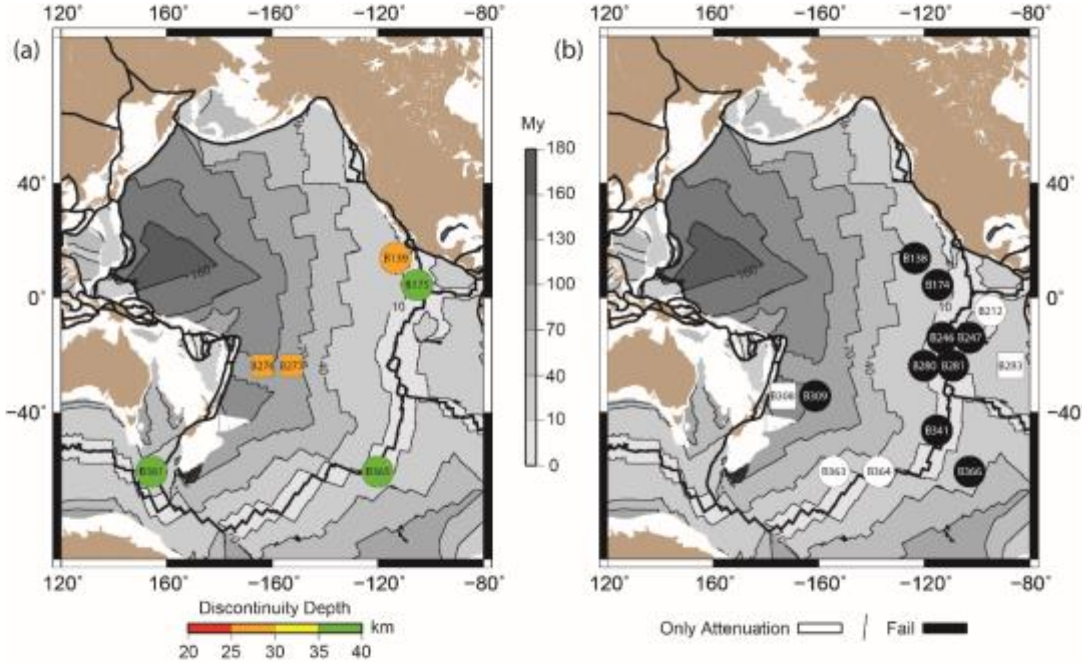

Figure 3.18: Pacific 10 ° SS bouncepoint bins with discontinuity depths allowing for higher attenuation. Numbers within the symbols correspond to Pacific bin identifiers. Bins 212, 283, 308, 363 and 364 in Figure 3.8c require no additional positive discontinuity if higher attenuation (>= 6.8 s) is allowed. Circles and squares show normal and anomalous lithosphere respectively. Colors in (a) show depth of positive discontinuity. (b) White bins require only attenuation to fit the data. Black bins could not be resolved. Background colors show seafloor age with age contours (thin black lines) at an interval of 30 My (Müller et al., 2013)). Thick black lines represent plate boundaries (Bird, 2003).

3.5.2 Pervasive Negative Discontinuity

3.5.2.1 Comparison to Previous Studies

Our results for the shallow, pervasive negative discontinuity (Figure 3.19) in the depth range of 30 – 80 km are in agreement with a previous study using SS precursors that imaged a sharp, (4 – 13% over <70 km) age dependent discontinuity at 25 – 70 km depth beneath young seafloor (< 40 – 70 My) (Rychert and Shearer, 2011). Our depths are only slightly deeper than RS11. Our results show greater depth-age dependence beneath young seafloor than those of *Schmerr*, [2012] (Figure 3.20).

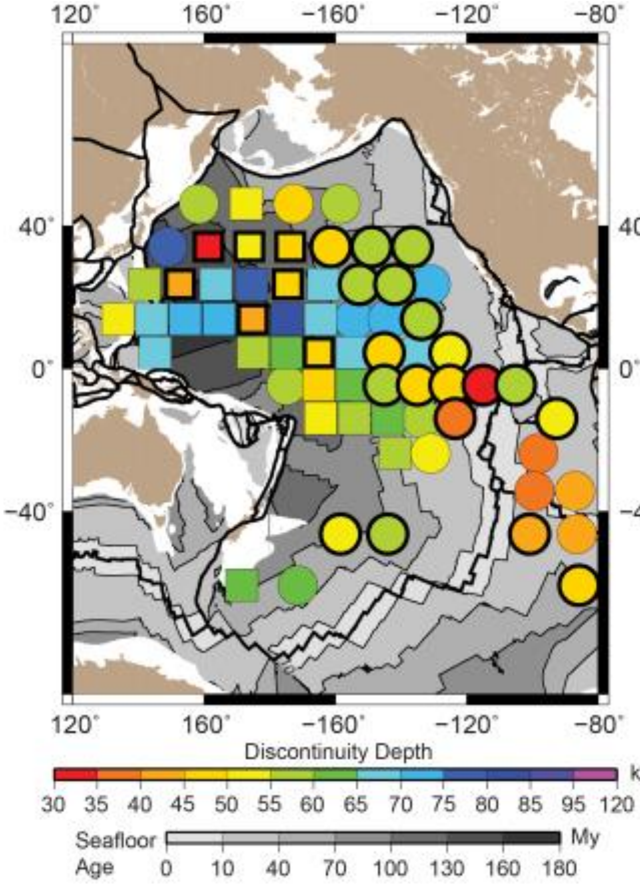

Figure 3.19: The shallow discontinuity at ~60 km is pervasive across most of the Pacific. Bins with no black outline show single negative discontinuity (Figure 3.8a). Bins with a thick black outline show shallow discontinuity from double discontinuity bins (Figure 3.8b). Background colors show seafloor age with age contours (thin black lines) at an interval of 30 My (Müller et al., 2013)). Thick black lines represent plate boundaries (Bird, 2003).

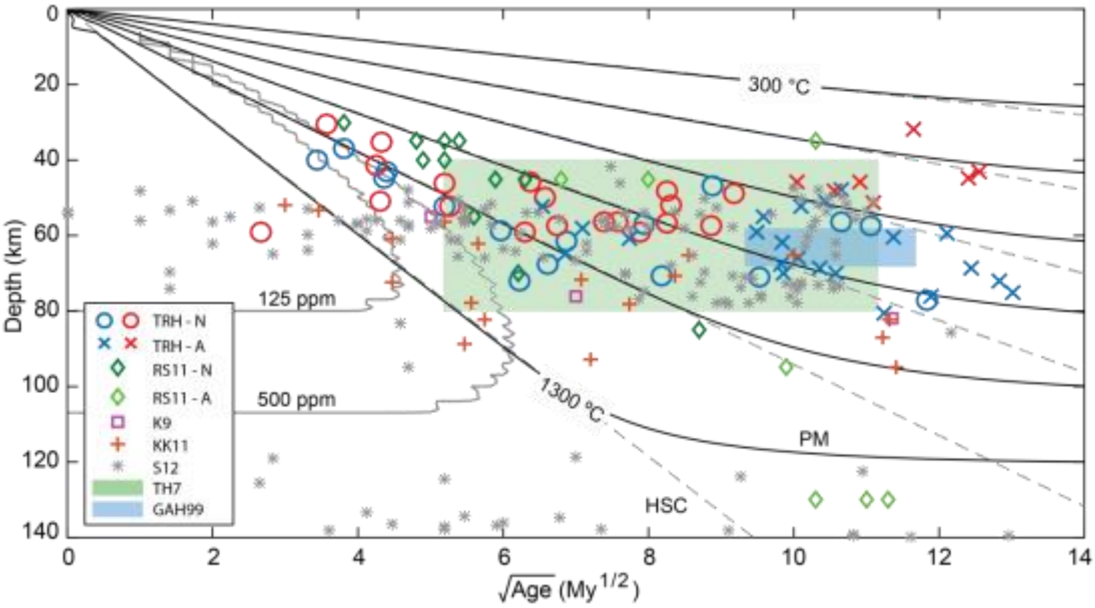

Figure 3.20: Depth of the shallow pervasive discontinuity compared to seafloor age and plate model (PM) / half – space cooling (HSC) isotherms. The present study is referred to as TRH. Circles (O) and crosses (X) correspond to normal (TRH - N) and anomalous lithosphere (TRH – A) respectively. Blue "O"/"X" shows results of single discontinuity and red "O"/"X" shows results of shallow discontinuity in bins with a deeper negative discontinuity (not shown). Diamonds show SS precursor results for normal (RS11-N) and anomalous (RS11-A) lithosphere from RS11 (Rychert and Shearer, 2011). Squares and pluses show LAB depths from receiver function studies of K9 (Kawakatsu et al., 2009) and KK11 (Kumar and Kawakatsu, 2011). Stars (S12) show discontinuity from previous SS precursor study (Schmerr, 2012). Colored boxes show results from TH7 (Tan and Helmberger, 2007) and GAH99 (Gaherty et al., 1999). Solid grey lines show melting region for a mantle melting model with varying amounts of water (ppm) (Katz et al., 2003). Solid black lines show isotherms for plate model (Stein and Stein, 1992) and dashed grey lines show isotherms for half space cooling model.

Our results for younger oceans are also supported by receiver function studies of oceanic stations in the northwest Pacific that image a sharp (7 – 8%

velocity reduction over 10 – 15 km) discontinuity at 55 km and 76 km with a plate age of 25 My and 49 My in the Philippine sea (Kawakatsu et al., 2009) (Figure 3.20). Further, a discontinuity in the depth range of 51 – 92 km that progressively increases with age from 9 – 70 My was also imaged using receiver functions along three oceanic plate margins in the Pacific (Kumar and Kawakatsu, 2011).

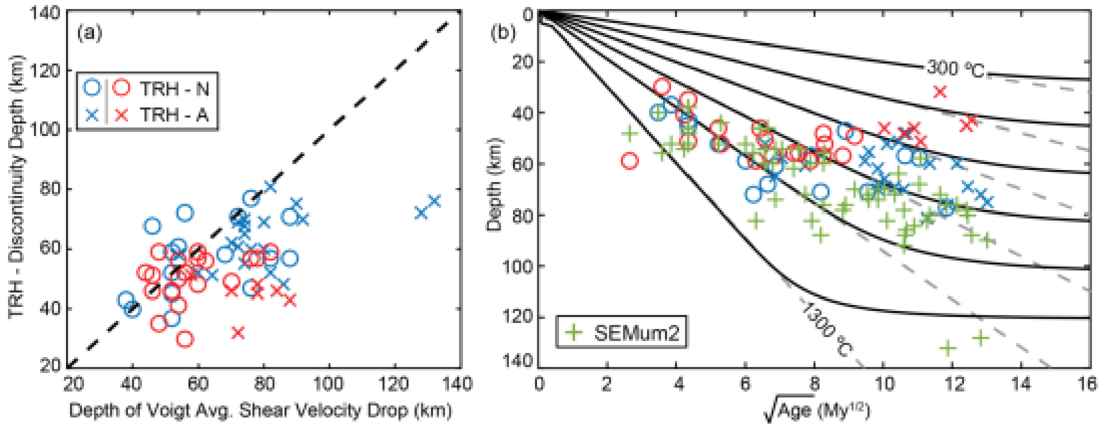

Figure 3.21: (a) Shallow discontinuity depths compared to depth of the negative gradient in Voigt average shear velocity in a global surface wave model, SEMum2 (French et al., 2013). TRH refers to the present study. Circles (O) and crosses (X) correspond to normal (TRH – N) and anomalous lithosphere (TRH - A). (b) Discontinuity depths from present study and depths estimated from SEMum2 plotted against square root of seafloor age.

Our discontinuity depth results beneath young seafloor, < 36 My (as determined by piecewise linear fit to the age–depth data), are also in general agreement with surface wave results that image a thickening lithosphere with age in both global (Nishimura and Forsyth, 1989; Maggi et al., 2006; Nettles and Dziewonski, 2008; French et al., 2013) and regional studies (Gu et al., 2005; Harmon et al., 2009). For example, our discontinuity depth results are in good agreement with the depth of the negative gradient in Voigt average isotropic shear velocity in a global surface wave model, SEMum2 (French et al., 2013) (Figure 3.21). We image a discontinuity in the depth range of 30 – 59 km compared to a discontinuity at 38 – 56 km in SEMum2 beneath similarly young seafloor (Figure 3.21b). However, the discontinuity we image is sharper, an average velocity contrast of ~7 – 8% occurring over <21 km compared to an average velocity drop of ~3.5% occurring over ~65 km in global surface wave models (French et al., 2013).

The discontinuity depths we image beneath the older (> 36 My) lithosphere appears to be at a near constant depth of ~60 km, cutting across isotherms from half-space cooling and plate models. The near constant depth discontinuities that we image are similar to those imaged in the depth range of 40 – 80 km (Gaherty et al., 1999; Tan and Helmberger, 2007), 40 – 100 km (Schmerr, 2012) and 60 – 94 km beneath old seafloor (Kumar and Kawakatsu, 2011) (Figure 3.20). Our results are also broadly consistent with the mean depth of the gradual drop in velocity with depth in surface wave models in most locations, although surface waves tend to be systematically deeper, by ~10 km (mean depth ~75 km) with 2 locations much deeper (~130 km) (French et al., 2013) (Figure 3.21).

Our results beneath older seafloor are also in agreement with the 6 – 12% velocity drop at 40 – 100 km depth beneath seafloor > 36 My (Rychert and Shearer, 2011) (Figure 3.20), but suggest a much more pervasive feature than previously detected (Figure 3.19). Our results are shallower (50 – 80 km) than the four deep (95 – 130 km depth) bins from RS11 (bins 70, 71, 99, 132). This is likely related to uncertainty in gradient shape and/or an artifact of the different parameterizations of the two studies. RS11 only allowed a single negative discontinuity, and thus required broad gradients in these bins. The gradients were tapered on the source side to avoid interference, and the peak of the Gaussian was reported. This would be more similar to our skewed results for double discontinuity bins. This could reconcile depth differences between bins 71 and 99, which were also fit by a wide skewed or a double discontinuity operator here and also bin 99 which had a large Gaussian width in RS11, leaving only bin 132 discrepant. Overall, the resolution and parameterization here is improved from the past since our larger dataset, with better quality control, allows for better constraints on the character of the gradient.

3.5.2.2 Comparison to Previous Transect Studies

We also compare our results to the pacific transects PA5 (Gaherty et al., 1999) and PAC06 (Tan and Helmberger, 2007) (Figure 3.22). For this comparison, we generated data and reference stacks, using the procedure described in section 2, to approximate the pacific transects PA5 and PAC06. The depth scaling was done assuming a constant oceanic crustal thickness of 7 km, crustal velocity of 3.75 km/s, an upper mantle velocity of 4.55 km/s, and an average horizontal slowness of 0.12 s/km. We resolve a sharp discontinuity, ~6% velocity contrast over <10 km at a depth of 40 – 60 km compared to the ~6% velocity change in the depth range of 40 – 80 km reported by PAC06 study (Tan and Helmberger, 2007). Similarly, we resolve a ~6% velocity contrast over <15 km at a depth range of 42 – 73 km along the PA5 transect compared to a sharp (<30 km thick) 6% velocity drop at a relatively constant depth of 60 ± 20 km (Gaherty et al., 1999). The discontinuity along PAC06 appears to be sharper than along PA5 transect. But the PA5 transect fits better with a sharper double negative discontinuity at 45 km and 70 km with a velocity contrast of 5 – 6% occurring over <10 km. The fact that our SS precursors also require sharp discontinuities in the similar depth range along PA5 and PAC06 transects suggests mechanisms other than temperature alone are required.

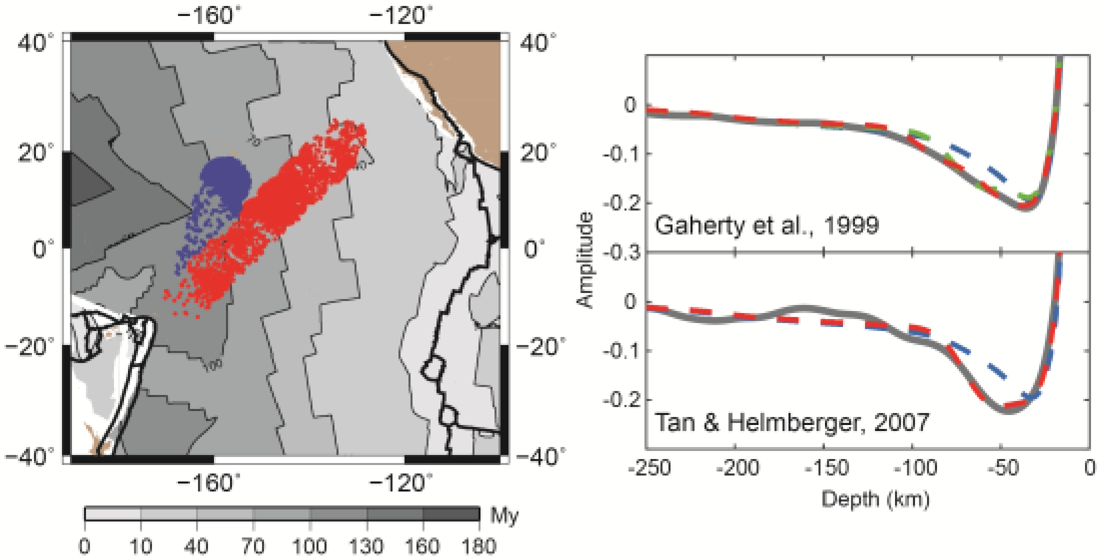

Figure 3.22: Bouncepoints included in the stacks that approximate the Pacific transects, PA5 (blue) (Gaherty et al., 1999) and PAC06 (red) (Tan and Helmberger, 2007). The background colors show seafloor age (Müller et al., 2013). Waveform fits for the two transects are shown on the right. Solid grey line is the data, dashed blue is the attenuated reference S wave, dashed red is the best-fit model and dashed green in the upper panel is best-fit model using a single discontinuity.

The discontinuity that we image along PA5 and PAC06, agree with the best-fit result from RS11, a 3 – 10% change over <50 km (Rychert and Shearer, 2011). However, a discontinuity was not statistically required along PA5 and PA06 in RS11. The improvement in resolution here is probably from our larger dataset, additional quality checks that we impose and also a different back azimuth distribution, primarily 50° – 90°, in comparison to the W – E back-azimuths that dominated RS11. Our stacks excluding the 50° – 90° back azimuth range show a reduction in amplitude for the two transects, suggesting an azimuthal anisotropic component to the discontinuity (Rychert et al., 2012; Rychert et al., 2014b). When we limit the back azimuth range considered here to that of RS11, we can no longer resolve a significant discontinuity along PA5. However, PAC06 could be resolved to within ± 4 km.

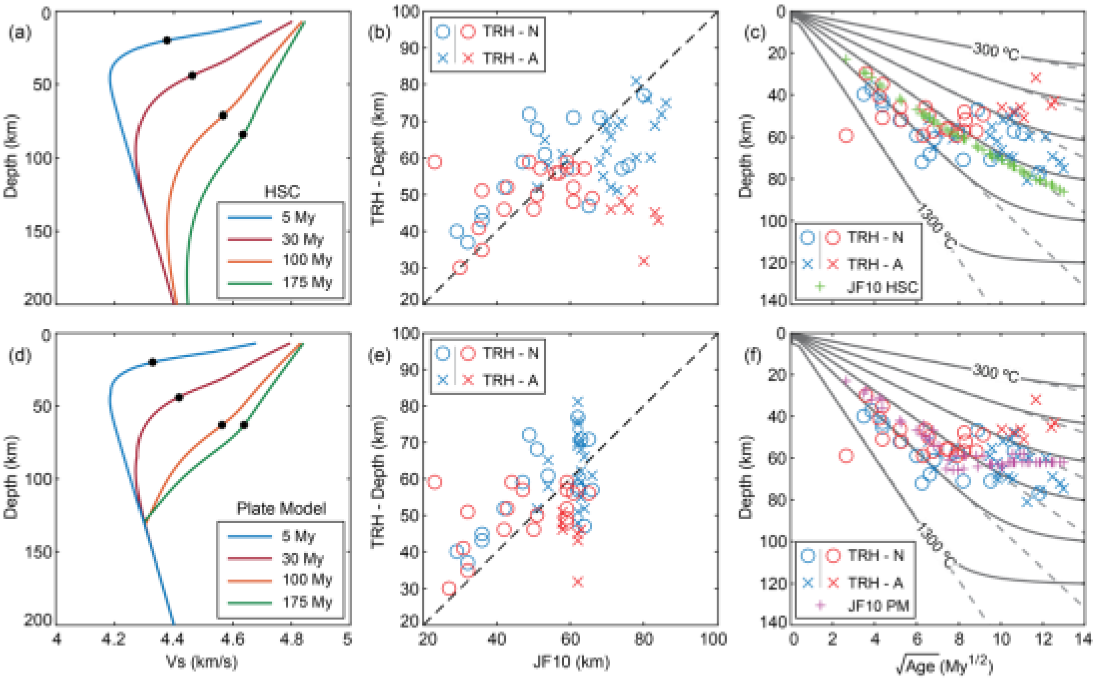

Figure 3.23: Our shallow pervasive discontinuity depths (TRH) compared to experimentally predicted depths for thermal models, JF10 (Jackson and Faul, 2010). Predicted seismic velocities assuming grain size of 20 mm, appropriate for typical mantle temperatures 1300 – 1450 ℃ and water content 50 – 2000 H/10^6Si at 150 km depth (Behn et al., 2009) for (a) half – space cooling (HSC) and (d) plate model (PM) (Stein and Stein, 1992). TRH discontinuity depths compared to predicted depths from (b) HSC and (e) PM. Predicted depth is the center of the negative velocity gradient in both HSC and PM indicated by black markers in (a) and (b). TRH discontinuity and predicted depths compared with age of bins for (c) HSC and (f) PM. Circles and crosses correspond to normal (TRH - N) and anomalous lithosphere (TRH – A) respectively. Blue color shows results of single discontinuity and red color shows results of shallow discontinuity in bins with double negative discontinuity.

3.5.2.3 Comparison to a Thermal Model

Our results show that the shallow, negative discontinuity beneath young ocean, < 36 My as determined by piecewise linear fit, increases in depth from 30 to 80 km with increasing seafloor age. This result is consistent with a thermally defined lithosphere that thickens with age (Figure 3.20), falling along the 1100 °C isotherm. To test a thermal origin for the Pacific lithospheric discontinuities, we considered experimental predictions for seismic velocity (Jackson and Faul, 2010) (hereafter referred to as JF10) from a half-space cooling (HSC) and plate model (PM) (Stein and Stein, 1992). We assume a grain size of 20 mm (Behn et al., 2009) and mantle potential temperature of 1350 °C. The anelastic effects (velocities deeper than the kink in the profiles) are frequency dependent. Here we assume surface wave frequency – depth relationships (Forsyth, 1992), although the frequency effect is not strong (Rychert et al., 2012). The predicted seismic velocity gradients are sharper for younger ages and more gradual beneath old seafloor (Figure 3.23). We estimate the discontinuity depth as the midpoint of the negative gradient in shear velocity for JF10, although the depth of the sharpest negative JF10 gradient are very similar (Figure 3.23). Our results for the shallow discontinuity are similar in depth range (< ±10 km) to those estimated from JF10 for seafloor < 36 My. For seafloor > 36 My, our results are shallower than estimated from JF10 (Figure 3.23b, 3.23e). There is strong correlation, 0.81 for HSC and 0.81 for PM, between our results and estimations from JF10 for seafloor < 36 My. However, our gradients are much sharper at all ages (3 – 15% over < 21 km) compared to those predicted by JF10, 8 – 11.5% over < 170 km for HSC and 10 – 11.5% over < 130 km for PM) (Figure 3.24, 3.25). The magnitude of discontinuity sharpness (% change in velocity / total depth range) we model is on an average 4 times greater than the predictions from JF10 (Figure 3.24). The sharpness of the discontinuity and the lack of relationship between discontinuity depth and square root of age in comparison to the predictions from JF10 suggests that the discontinuity we image may not have a purely thermal origin and other processes may be required to explain the discontinuity.

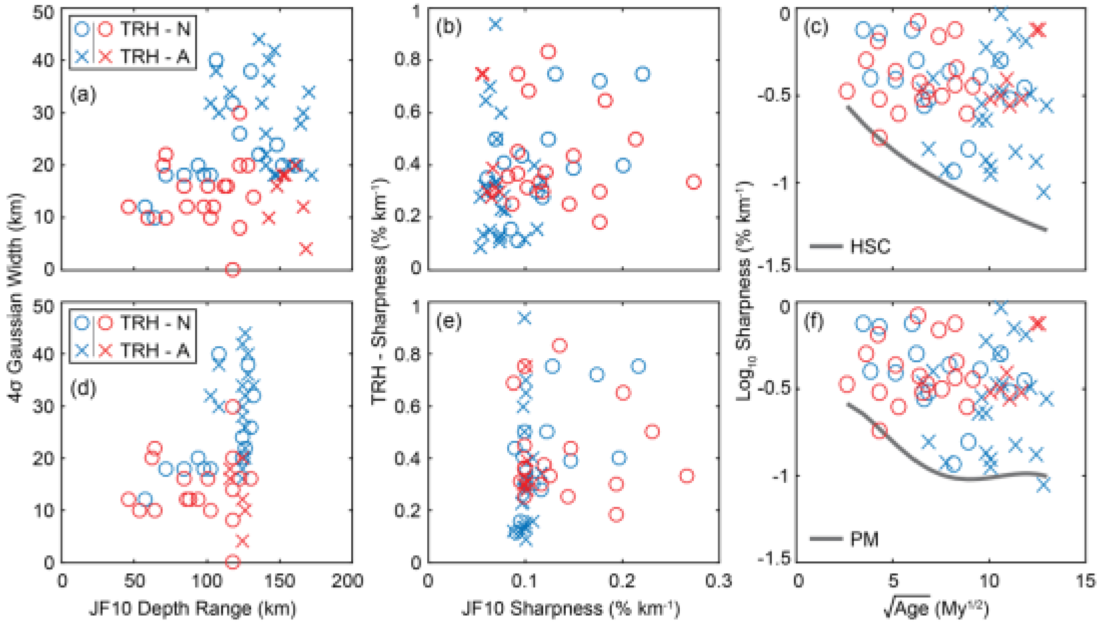

Figure 3.24: Discontinuity sharpness compared to thermal model. TRH refers to the present study. Gaussian width, i.e. ±2σ, of the discontinuity compared to total depth range of negative velocity gradient in JF10 for (a) HSC and (b) PM. TRH discontinuity sharpness, i.e. % change in velocity over total depth range, compared to JF10 discontinuity sharpness for (b) HSC and (e) PM. Logarithm of discontinuity sharpness (Log$_{10}$ Sharpness) compared to seafloor age for (c) HSC and (f) PM. Solid grey line in (c) and (f) show logarithm of sharpness from JF10. Circles and crosses correspond to normal (TRH - N) and anomalous lithosphere (TRH – A) respectively. Blue shows results of single discontinuity and red shows results of shallow discontinuity in bins with double negative discontinuity.

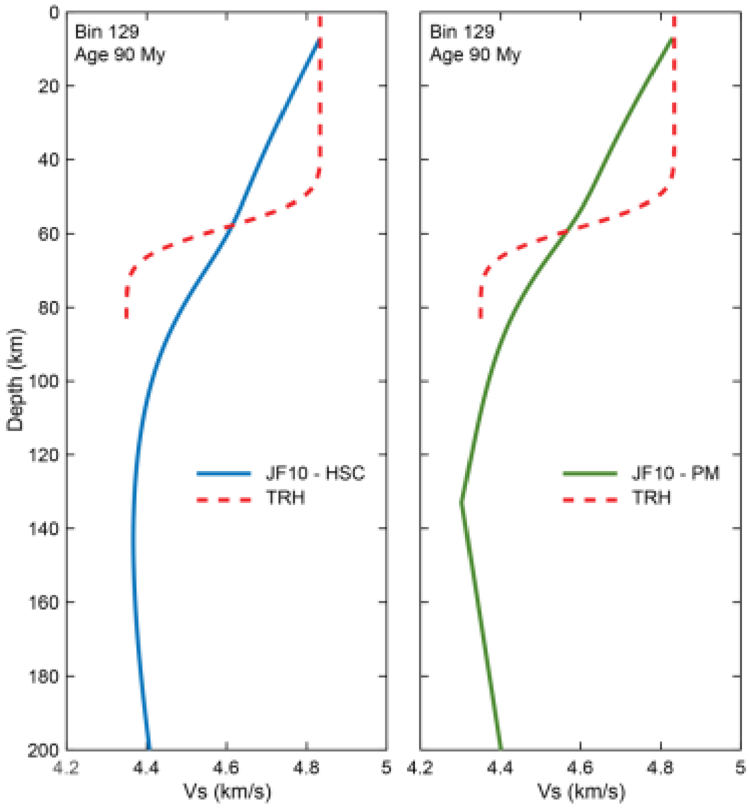

Figure 3.25: TRH velocity model for Bin 129 with seafloor age of 90 My compared to JF10 velocity model for HSC (blue) and PM (green). Depth is in relation to seafloor.

3.5.2.4 Causative Processes for the Shallow, Pervasive Negative Discontinuity

Anisotropy: An abrupt change in seismic anisotropy could explain apparent velocity discontinuities in SS waveforms (Rychert et al., 2014b). Azimuthal anisotropy would cause SS precursor underside reflections of varying amplitude and sign (positive or negative) depending on the back azimuth direction. Limitations in back-azimuthal distribution of the data make tight constraints difficult. However, we attempted to detect polarity variations in the discontinuity required by our SS waveforms when stacked along different back-azimuth ranges. Although we detect variations in amplitude with back-azimuth, we do not see evidence for variations in polarity. In addition, we do not detect positive polarity discontinuities near ~60 km depth in any bins across the Pacific. This suggests that azimuthal anisotropy is not the only factor defining the observed discontinuity.

Negative SS precursors could result from a sharp increase in radial anisotropy with depth. However, whether or not radial anisotropy is strongly increasing at 60 km depth is debated. An increase in radial anisotropy from 0 to 100 or 150 km depth is a feature of most global models (Nettles and Dziewonski, 2008; Beghein et al., 2014; Burgos et al., 2014; Auer et al., 2015). Although, in-situ regional constraints suggest that the strongest anisotropy is shallow (Weeraratne et al., 2007; Takeo et al., 2013; Lin et al., 2016). These studies constrain azimuthal anisotropy that would translate to radial anisotropy if caused by horizontal alignment of olivine. In addition, if our results represent the same feature(s) imaged by receiver functions from the Pacific (Kawakatsu et al., 2009; Kumar and Kawakatsu, 2011), radial anisotropy cannot provide a simultaneous explanation (Harmon et al., 2016; Rychert and Harmon, 2017).

Composition: Extraction of basaltic melt at a mid-ocean ridge may result in a dry, depleted residuum (Hirth and Kohlstedt, 1996). The difference in seismic velocity between the seismically fast residuum and the slower deeper mantle beneath could produce a seismic velocity discontinuity, related to the depth of melting near ~60 km depth, which would be age independent (Gaherty et al., 1999). This resembles the depth of our results (50 – 80 km, average depth of ~60 km) beneath seafloor > 36 My old which show no age dependence. Compositional boundaries can also be quite sharp (Hirth and Kohlstedt, 1996; Rychert et al., 2005; Rychert et al., 2007), certainly sufficient to explain our constraints on the depth range over which the discontinuity occurs. In terms of magnitude, typically chemical depletion can explain ~1% velocity contrast (Schutt and Lesher, 2006). However, in the special situation where there is frozen-in melt at shallow depths as a garnet-rich rock like eclogite, the contrast could be larger, ~5% (Hacker and Abers, 2004). In addition, although we parameterized the inversion in terms of seismic velocity, density effects from composition might also play a role, potentially enhancing the apparent contrast by 2 – 3%**.** Therefore, if a somewhat exotic melt composition is pervasively frozen-in to the lithosphere this could explain up to an ~8 % sharp contrast, satisfying the bulk of our observations beneath seafloor > 36 My.

Although dehydration may also contribute to seismic velocity discontinuities, it may not be significant beneath the older seafloor (> 36 My) if the effect of hydrated olivine on seismic waves is diminished at cold temperatures (Behn et al., 2009). However, alternatively, it has been suggested that elastically accommodated grain boundary sliding (EAGBS) could enhance the effect of water on seismic waves (Olugboji et al., 2013; Karato et al., 2015), and the temperature–pressure dependence of the effect would create a discontinuity with a similar age – depth dependence to our observations at younger ages. However, the magnitude of this effect is debated (Jackson and Faul, 2010) and experimental work on hydration is beginning to emerge (Aizawa et al., 2008).

Partial Melt: The presence of melt in the asthenosphere could explain a large velocity drop with depth. This might occur along the solidus if melt is present in significant amounts just deeper than the solidus. At the mid ocean ridge axis, large volumes of melt in the mantle (~1%) could produce a velocity drop of up to 7.9%, although the exact magnitude depends on the amount of melt and melt-distribution geometry (Hammond and Humphreys, 2000; Kawakatsu et al., 2009). Just off the ridge axis, the small degrees of asthenospheric melt could accumulate in regions where the solidus acts as a permeability boundary (Sparks and Parmentier, 1991; Hirschmann, 2010; Katz, 2010), enhancing the velocity contrast along the solidus out to ~40 My assuming 500 ppm water content (Katz et al., 2003) (Figure 3.26). The melt concentration may be significantly higher at the permeability boundary (porosity on the order of 0.10 or 10% by volume) (Sparks and Parmentier, 1991). At young seafloor ages (< 36 My), the solidus happens to also be quite similar to the 1100 °C isotherm and could explain the correlation at young ages (Figure 3.20, 3.26). The enriched solidus (500 ppm water) diverges from the 1100 °C isotherm at greater ages (Figure 3.20).

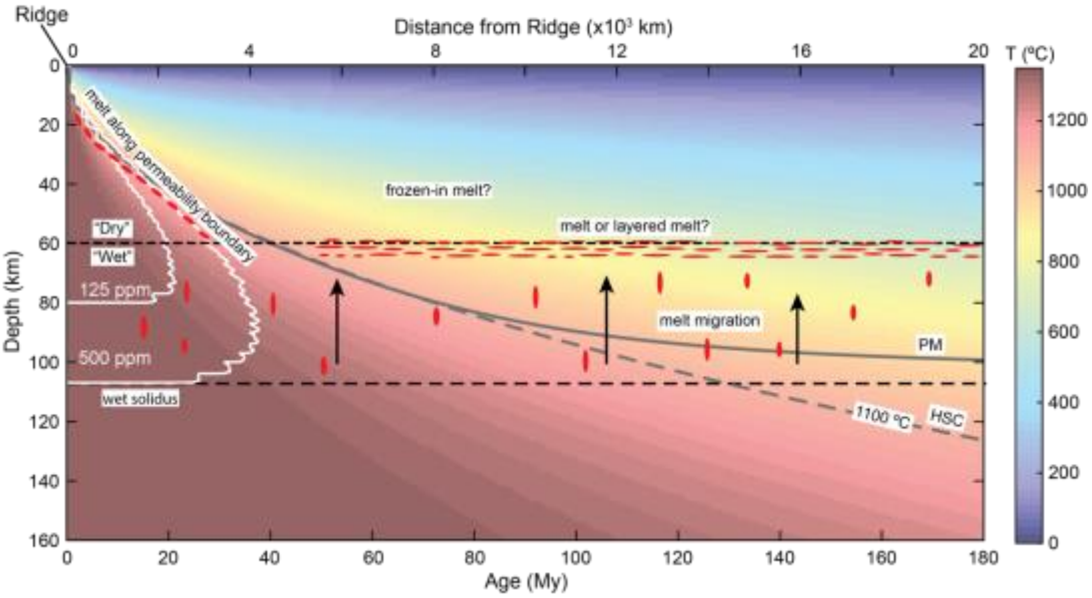

Figure 3.26: Schematic of a model that explain the shallow and deep discontinuity in our results. Solid and dashed grey lines show 1100 ℃ isotherm for PM and HSC respectively. White lines demarcate melting region for a mantle melting model with varying amounts of water (ppm) (Katz et al., 2003).

Beneath older seafloor, mantle melt production is expected to be small. In addition, temperatures are expected to be below the silicate melt solidus at 60 km depth. Volatiles such as water and CO_2 could form a small degree of partial melt in the asthenosphere, although sub oceanic mantle is expected to be depleted in volatiles, with correspondingly small melt contents (<< 0.1% melt), insufficient to explain our result (Hirschmann, 2010). In areas of local enrichment (~500 ppm H_2O and CO_2), such as mantle plumes or subducting slabs, volatiles could potentially stabilize melt accumulation at 50 – 80 km depth to 140 My seafloor (Sifre et al., 2014) through the formation of a permeability boundary and/or the neutral buoyancy of the melt (Sakamaki et al., 2013). Diking of asthenospheric melt and subsequent heating and thinning of the lithosphere (Havlin et al., 2013) could explain a ~60 km lithosphere in regions with high melt production (at least 0.63 % melt). However, all of these models require large, constant supply of volatiles and/or melt, which is not predicted over the entire Pacific. One possibility is that low degrees of asthenospheric carbonatite melt (Hirschmann, 2010) in horizontal bands such as suggested in the "millefeuille model" could produce the required velocity contrasts over large swaths of the Pacific without the need for extreme volatile and/or melt contents (Kawakatsu et al., 2009), potentially explaining our observation. The melt would likely affect the strength of the mantle (Hirth and Kohlstedt, 1995; Faul, 1997), and the boundary would necessarily represent the lithosphere-asthenosphere boundary in this case (Rychert et al., 2005; Rychert et al., 2007).

3.6 Conclusions

We resolve a sharp, pervasive seismic discontinuity across the Pacific at 30 – 80 km depth with a 3 – 15% shear velocity drop over < 21 km in the depth. It increases in depth with age from the ridge to 36 ± 9 My according to conductive cooling along the 1100 °C isotherm. Beneath older seafloor, > 36 My, there is no apparent age – depth dependence and the discontinuity is imaged at a constant depth of 60 ± 1.5 km. A purely thermal origin of the discontinuity is unlikely as the velocity contrast is sharper than expected from thermal models. The discontinuity beneath younger seafloor is likely related to the accumulation of melt at a permeability boundary, which is controlled by the solidus depth. The discontinuity depths beneath older seafloor could be explained by a compositional boundary from a strong pervasive frozen-in melt signature. Although not necessarily the LAB, this type of pervasive compositional variation would probably influence mantle rheology and the LAB transition. Alternatively, melt could explain our observations at older ages where thin layers of carbonatitic melt form as in the “millefeuille” model, and/or coalesces at a permeability boundary. In this situation, the melt would likely weaken the mantle, and the boundary would then represent the LAB. An intermittent 4% drop in shear velocity over < 11 km is imaged in the depth range of 80 – 120 km depth (average depth of ~100 km) with no apparent age dependence. In many cases, it could represent continually decreasing velocity in concert with the shallower feature.

Chapter 4

Imaging the Cratons

This chapter forms a paper under review in Science magazine as a research report:

Tharimena S., Rychert C. A., Harmon N., A unified seismo–petrological continental root defined by melt. *Science* (*in review*).

Page intentionally left blank.

4.1 Abstract

The precise thickness of the continents and the property that defines them are debated. Xenoliths suggest a ~175 km thick chemical lithosphere whereas seismic tomography supports a much thicker (>250 km) root and a gradual lithosphere-asthenosphere transition, consistent with a thermal definition. Here we model SS precursors using 11,839 bouncepoints beneath continental interiors. We find a 7 – 9 % velocity drop at 130 – 190 km depth. The discontinuity depth is well-correlated with the deepest origin depths of diamond bearing kimberlites. In addition, it corresponds to the coarse – to – deformed xenolith transition, and the carbonated–silicate solidus. This suggests that melt likely explains the discontinuity, and defines the plate even beneath deep continental interiors.

4.2 Introduction

The origin of continents has been obscured by billions of years of history. Various hypotheses have been put forward to explain their formation including large mantle plume – related melting events that led to compositional depletion (Boyd, 1989), stacking of young oceanic lithosphere (Calvert et al., 1995), or island arc accretion with orogenic thickening at subduction zones (Lee et al., 2011; Taylor and Mclennan, 1995).

Continents are buoyant, stable features with a thick lithosphere that have resisted recycling in to the mantle since formation. Xenoliths brought to the surface by kimberlite eruptions provide direct sampling of the interior of the continents, and suggest that the continental lithosphere could be 150 – 200 km thick (Boyd et al., 1985; Pearson et al., 2003). Further, study of Archean diamonds and their inclusions, primarily from the Kaapvaal and Siberian cratons (Richardson et al., 1984), suggests that the thick continental lithosphere could have formed and was cold as early as 3.4 Ga (Boyd et al., 1985). Geochemical analysis of mantle xenoliths also suggest that the continental lithosphere is made up of highly depleted, low-density, dehydrated compositions that help stabilise cratons (Jordan, 1978; Pollack, 1986). Isostasy similarly supports the notion of buoyant, chemically distinct continental lithosphere/roots extending to great depths beneath cratons (Jordan, 1975).

The stability and longevity of the cratonic lithosphere is generally attributed to positive chemical buoyancy (Jordan, 1988) and viscosity (Sleep, 2003), which are required by geodynamic models (Cooper et al., 2004; Lenardic and Moresi, 1999). In addition, the mobile belts that surround the cratons may be important in protecting them from erosion (Lenardic et al., 2000). However, imaging their internal discontinuity structure and its relation to formation, evolution and longevity of cratons has proven challenging.

The notion of thick continental lithosphere from xenolith thermobarometry is supported by seismic data. Seismic tomography can resolve deep continental lithospheric structure on the scale of 10s to 100s of km. Surface waves suggests the continents are seismically fast in comparison to oceans down to 200 – 300 km depth beneath cratons, in both global and regional models (Cammarano and Romanowicz, 2007; Dalton et al., 2009; Nettles and Dziewonski, 2008). Whereas some body wave studies have argued that the fast anomalies could extend even deeper to 400 km (Jordan, 1988; Masters et al., 1996). The transition from seismically fast to slow anomalies is generally considered to be the base of the cratonic root and is deeper, ~200 – 280 km (Pasyanos, 2010), than observed from xenolith data, 150 – 200 km depth (Figure 4.1). Seismic waves are primarily sensitive to temperature, so the discrepancy between the shallow geochemical boundary and the deeper seismic signature could imply that a thin chemical lithosphere is underlain by a thicken thermal root (King, 2005; Lee et al., 2011). The seismic velocity gradient from the fast continental lithosphere to the underlying slower asthenosphere is often very gradual in surface wave tomography models, consistent with a thermal definition. However, some studies suggest that surface waves resolution is quite broad at these depths and may not have the sensitivity to resolve low velocity structure > 200 km depth (Pedersen et al., 2009). In addition, some studies suggest that the low-velocity zone beneath cratons may be subtle or even non-existent (Gaherty and Jordan, 1995; Gaherty et al., 1999; Revenaugh and Jordan, 1991).

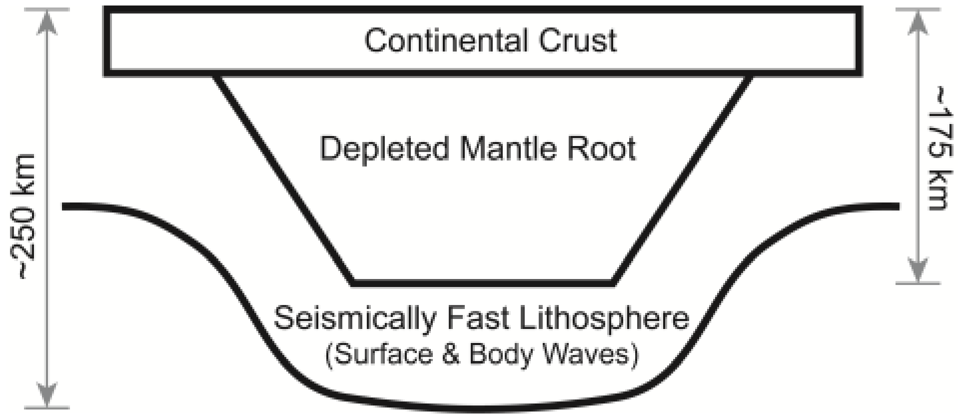

Figure 4.1: How thick are the continents? A schematic showing the discrepancy between seismic and petrological continental thickness estimates.

Regional surface wave models offer better resolution, specifically the anisotropic fabric within the lithosphere compared to global tomography models. Both radial and azimuthal anisotropic structures have been used to explain negative velocity drops within and at the base of the lithosphere beneath North America (Bostock, 1998; Rychert and Shearer, 2009; Wirth and Long, 2014; Yuan and Romanowicz, 2010), South Africa (Sodoudi et al., 2013) and Australia (Debayle and Kennett, 2000; Ford et al., 2010). A structure is radial anisotropic when horizontally polarized shear velocity is faster than vertically polarized shear velocity ($V_{SH} > V_{SV}$)) and a structure is azimuthal anisotropic when shear velocity is faster along a certain direction governed by the orientation of the olivine a-axis. The North American craton, one of the widely studied continental regions, is suggested to be underlain by two layers of anisotropy, an anisotropic fabric that is predominantly frozen in the lithospheric, and an asthenospheric anisotropic component that is maintained by shear deformation due to mantle convection (Gaherty, 2004; Yuan and Romanowicz, 2010). In this scenario, the cratonic lithosphere is suggested to be 180 km, the base of which is characterized by shear deformation.

Other seismic techniques have also been used to probe the lithospheric structure. Some receiver function studies have reported sharp discontinuities in the 150 – 300 km depth range beneath the South African and South American cratons, and interpreted them as the LAB (Hansen et al., 2009; Heit et al., 2007; Sodoudi et al., 2013). However, other studies have not been able to image discontinuities associated with LAB in that depth range beneath North America and Australia, suggesting that velocity gradients at this depth are too gradual for receiver function imaging (Abt et al., 2010; Ford et al., 2010; Kumar et al., 2012; Rychert and Shearer, 2009). But discontinuities at shallower depths (60 – 120 km), termed mid-lithospheric discontinuities (MLD), are frequently imaged (Abt et al., 2010; Ford et al., 2010; Kumar et al., 2007; Selway et al., 2015). These shallow negative velocity discontinuities have been associated with the presence of melt or fluids, changes in chemical composition, and/or anisotropy (Selway et al., 2015; Thybo and Perchuc, 1997; Wolbern et al., 2012; Yuan and Romanowicz, 2010). However, the origin and defining mechanism of both MLD and LAB has been a subject of intense debate. Seismic velocity and seismic discontinuity structure can help with a better understanding of the current continental cratons, and perhaps offer clues to the past. In particular, constraints on the Moho, MLD, and LAB may be related to formation. However, self-consistent and tight constraints on variability among continents have proven to be a challenge.

Here we use SS precursors to image the lithospheric discontinuity structure beneath cratons including the Moho, MLD, and LAB. The benefit of SS is that it can be used to evaluate existence of a discontinuity, its depth, strength and sharpness in a self-consistent way. Characterising the cratonic LAB and MLD globally could give a better understanding of the origin and evolution of the continents.

4.3 Data and Methods

The cratons are divided into 8 regions, North America (NA), South America (SA), Europe (EUR), Siberia (SIB), West Africa (WAF), South Africa (SAF), India (IND) and Australia (AUS), based on the 3SMAC classification scheme (Nataf and Ricard, 1996). Due to lack of regionalization in Antarctica, we classify the region east of the Transantarctic mountain range as the East Antarctic craton (ANT).

We use SS precursors (Rychert and Shearer, 2010, 2011; Schmerr, 2012; Tharimena et al., 2016) to image the lithospheric discontinuity structure beneath cratons including the Moho, mid-lithospheric discontinuity (MLD) and lithosphere-asthenosphere boundary (LAB). SS precursors are weak underside reflections from velocity discontinuities and require stacking a large number of seismograms to bring them above noise (Rychert and Shearer, 2010, 2011; Tharimena et al., 2016). We use transverse component data from Incorporated Research Institutions for Seismology (IRIS) from 1990 – 2015 with source – receiver offsets of 90º – 140º (Figure 4.2), pre-processed to remove instrument response. Events with magnitude >5.5 Mw and source depth < 75 km are used to ensure good signal–to–noise ratio (SNR) and minimize complications from depth phases. The transverse component data is Hilbert transformed and low – pass filtered at 0.1 Hz. The filtered traces are centered on the SS phase, which is the maximum positive or negative amplitude in a window 40s before and after the theoretical arrival time of the SS phase. Negative SS phases are flipped and each trace is weighted to its SNR, which is the ratio of maximum SS amplitude to the standard deviation in a window 270s to 30s preceding the SS pulse. Waveforms with SNR > 4 are stacked and normalized to unit amplitude. We obtain 92,517 waveforms that have bouncepoints beneath the cratons and fit the source parameters described above, 11,839 of which also fit the SNR criteria. We also generate a reference SS stack using ~93,000 waveforms with bouncepoints beneath the global ocean basins. The global oceanic SS stack is relatively unaffected by the thin oceanic crust (~6 – 8 km). This gives us an ideal starting point to test for discontinuity structure beneath cratons as it is unaffected by the thin oceanic crust (~6 – 8 km).

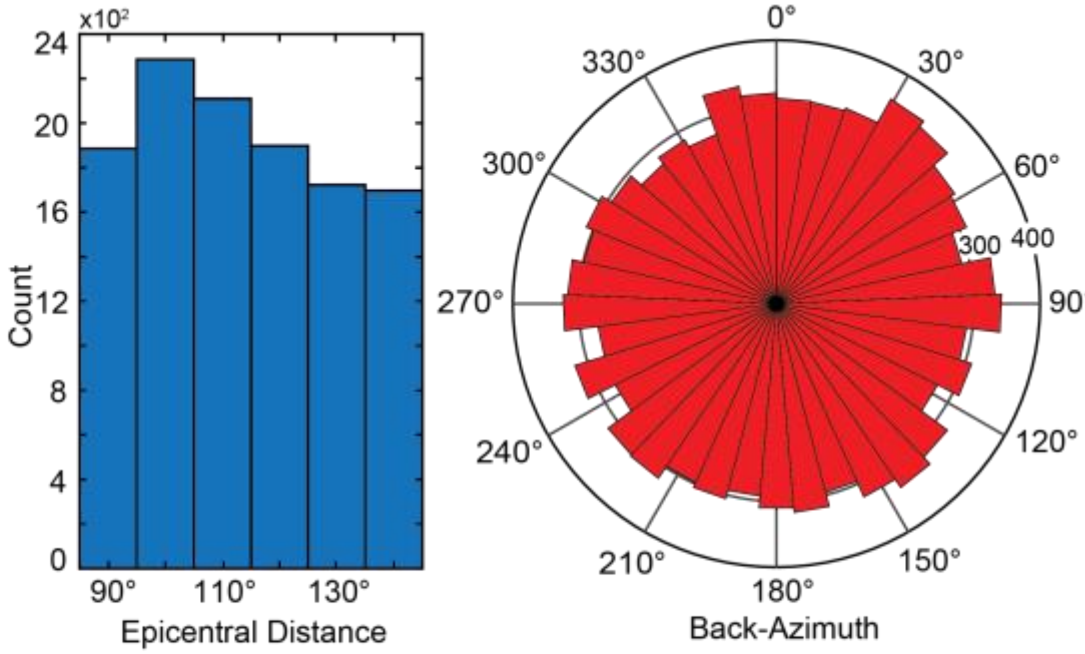

Figure 4.2: Event – station (epicentral distance) and back-azimuth distribution of the data used in the present study.

4.3.1 SS Precursor Modeling

We model the discontinuity structure using a forward modelling approach. Operators that correspond to discontinuities are convolved with a reference waveform (SS oceanic stack) to generate a synthetic waveform to match the data stacks in the time window preceding the main SS phase (Rychert and Shearer, 2010, 2011; Tharimena et al., 2016). The discontinuity operator is a Gaussian function that tests a range of discontinuity sharpnesses, i.e. step function to gradual velocity gradients. The sharpness of discontinuities in our study represents four times the Gaussian half-width, or ±2σ.

We test for various discontinuities by systematically increasing the number of discontinuity operators, allowing the model to choose between a positive or a negative discontinuity (Figure 4.3). At each step in the modelling process, the goodness-of-fit of the synthetic waveform with the data waveform was estimated. A grid search algorithm was used to determine the synthetic waveform that best-fits the data waveform and is statistically significant, i.e. a synthetic with the least residuals. An F-test was used to determine the statistical significance of the model parameters (Hosmer et al., 1997). We estimated 11 degrees of freedom in the data using autocorrelation of the reference SS waveform. We use 1 model parameter (depth) for the Moho and 3 model parameters (depth, amplitude and Gaussian width) for other discontinuities. The data, reference and best-fit synthetic waveforms are then migrated from time to depth domain. We use IASP91 reference Earth model (Kennett and Engdahl, 1991) and a global average horizontal slowness for SS

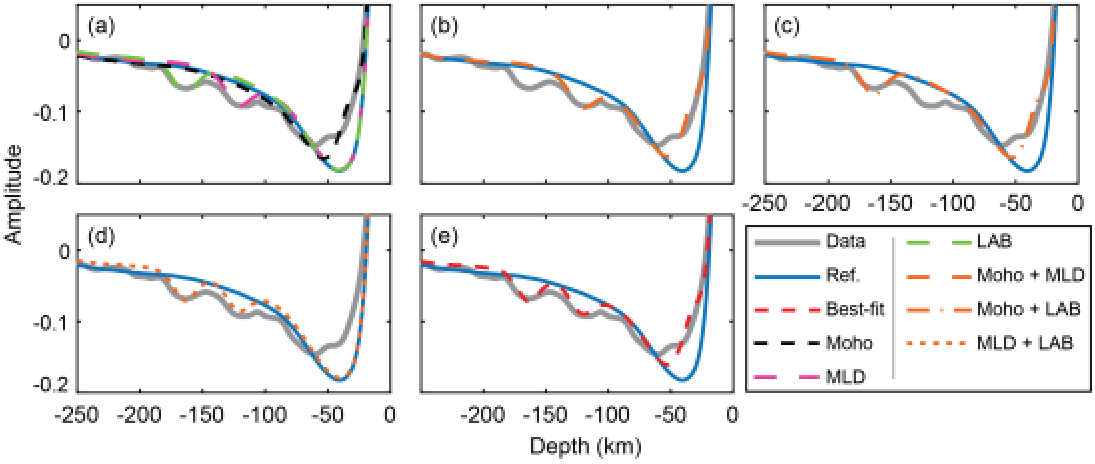

Figure 4.3: Visualization of the modeling process. Discontinuities are systematically introduced and the model parameters are tested for statistical significance.

of 0.12 s/km, at a reference epicentral distance of 115°, to calculate the travel times for different depth layers. These travel times are used to migrate the waveforms to depth domain (Shearer et al., 1999) (Figure 4.4). Tests using different velocity models for migration to depth did not yield significantly different results within the time window preceding the main SS phase. For example, the error in the depth of the discontinuity using IASP91 (Kennett and Engdahl, 1991) and S40RTS (Ritsema et al., 2011) velocity models for time – depth migration is < ±4 km.

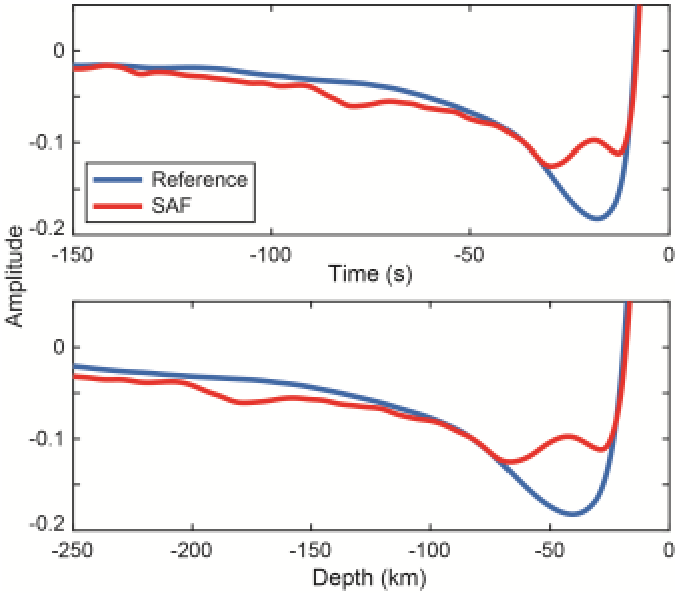

Figure 4.4: Visualization of migration of waveform stack from time to depth domain using IASP91 reference Earth model (Kennett and Engdahl, 1991).

The best-fitting model parameters are used to determine the depth, amplitude, and sharpness of the discontinuity(s). Velocity discontinuities produce two first – order reflections, a precursor that arrives before and a reverberation that arrives after the SS phase. We model only precursors in this study. The depth of the discontinuity is scaled from delay time of the precursors using the method of *Rychert and Shearer* [2010]. Similarly, operator amplitudes are scaled to velocity variation amplitudes (percentages) using SS reflectivity coefficient (Aki and Richards, 2009). For the modelling presented here, we assume a shear velocity of 3.55 km/s in the crust and 4.78 km/s in the mantle (average shear velocity from *French et al, 2013*), and a global average horizontal slowness for SS of 0.12 s/km.

4.3.2 Error Analysis

To quantify the error, we perform bootstrap resampling of the data with replacement (Efron and Tibshirani, 1986) for each of the 9 craton stacks. The bootstrap test involves stacking the same number of SS waveforms in each craton stack, randomly resampling waveforms included in the original stack allowing repetition of waveforms. We perform 100 bootstraps for each craton stack. We determine the best-fitting model parameter(s), using the method described above, for each bootstrap and invert them to determine the depth, amplitude, and sharpness of the discontinuity(s). The error in the model parameters corresponds to the range of model parameters within the bootstrapped limits of the data. The uncertainty is given by 95% confidence bounds, which corresponds to two standard deviations of the mean of the resulting variability.

The moveout of precursors, i.e. variation in precursor – SS differential travel times for different event – station distances, also adds error to our depth estimates. However, the effect of moveout is less than 1/4th of the dominant wave period (20s) used in our study, and is incorporated within the error limits from the bootstraps (Tharimena et al., 2016).

4.4 Results

The SS stacks beneath cratons are characterized by a broad low amplitude sidelobe caused by the thick continental crust. Waveform modelling suggests a crustal thickness of 35 – 48 km beneath the 9 cratons (Figure 4.5, Table 4.1). The one standard error estimate in depth based on bootstraps is 4 km.

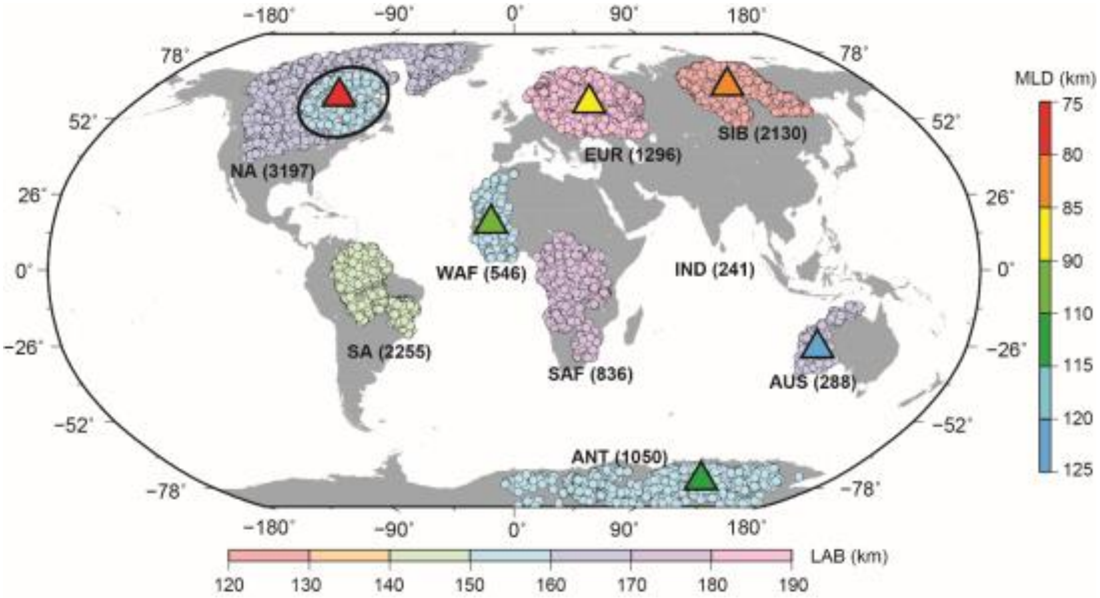

Figure 4.5: SS bouncepoints (colored circles) beneath cratons binned using 3SMAC classification (Nataf and Ricard, 1996). Pastel colors indicate lithosphere – asthenosphere boundary (LAB) depths beneath cratons, NA – North America, EUR – Europe, SIB – Siberia, SA – South America, WAF – West Africa, SAF – South Africa, IND – India, AUS – Australia, and ANT – Antarctica. Numbers in parentheses indicate number of bouncepoints. Colored triangles indicate mid–lithospheric discontinuity (MLD) depths. The black line defines region used for Hudson Bay – NA regional stack.

We image a negative discontinuity beneath all cratons at 130 – 190 km depth except the IND craton (Figure 4.5, 4.6). The discontinuity is relatively sharp with an average velocity contrast of 8 ± 2% over < 30 km (Table 4.1). The discontinuity beneath EUR appears to be relatively gradual with a velocity contrast of 9 ± 2% over < 52 km centered at 186 km depth, which can be seen as a broad feature with negative amplitude (Figure 4.6). The SIB, WAF, SAF, AUS and ANT cratons have a relatively sharp negative discontinuity with a velocity contrast of 7 ± 3% over < 20 km. The 95% confidence bounds on the depth estimates are < ±4 km except beneath EUR where the confidence bound is ±8 km. We do not image a negative discontinuity beneath the IND craton which is characterized by a broad low amplitude feature, at 70 – 160 km depth, well separated from the Moho phase at 37 km depth. Relaxing the SNR criteria from 4 to 3 for bouncepoints beneath IND, we obtain an additional 250 waveforms but the SS stack is still characterized by the low amplitude feature and we do not image a negative discontinuity.

We also image a shallower negative discontinuity at 80 – 121 km depth, beneath some cratons (Figure 4.6, Table 4.1). We image this discontinuity at 86 ± 7 km depth beneath EUR, 83 ± 4 km beneath SIB, 100 ± 5 km beneath WAF, 121 ± 3 km beneath AUS, and 110 ± 3 km beneath ANT cratons. The discontinuity is sharp with an average velocity contrast of 5 ± 1.5 % occurring over <14 km. There is relatively large uncertainty beneath EUR due to the broad negative amplitude in the SS stack compared to the reference waveform, similar to the gradual velocity gradient of the deeper discontinuity at 186 km. We do not image a discontinuity at 80 – 121 km depth using the entire NA craton stack. However, when we include only bouncepoints in the Hudson Bay and eastern NA, we image a discontinuity at 78 ± 4 km with a velocity contrast of 5 ± 1 % occurring over < 10 km (Figure 4.6). The Moho for the Hudson Bay – NA stack is at 49 ± 4 km, well within the error bounds of the Moho imaged using all of the data beneath NA craton at 45 ± 4 km depth. The deeper discontinuity in the Hudson Bay – NA stack is imaged at 152 km depth, slightly shallower than in the entire NA stack at 167 km depth.

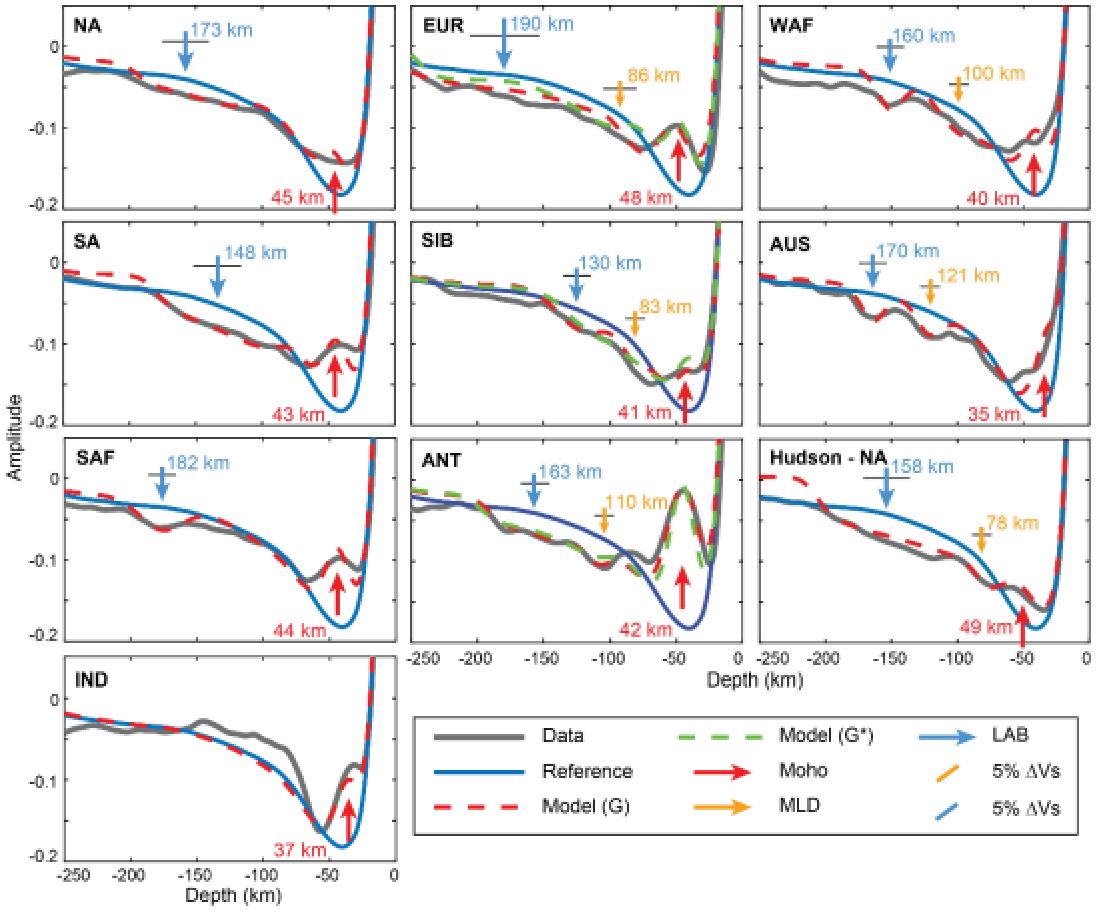

Figure 4.6: Waveform fits of the cratons modeled using a global oceanic SS stack as a reference waveform and simple Gaussian operators (G). The colored arrows show the location of discontinuities - red is Moho, yellow is mid – lithospheric discontinuity (MLD) and blue is the lithosphere – asthenosphere boundary (LAB). EUR, SIB and ANT could be equally well fit by skewed Gaussian operator (G). The length of yellow and blue arrows indicate % velocity drop. The horizontal bars indicate Gaussian widths over which the velocity drop occurs.*

Table 4.1: SS Discontinuity Structure Beneath Cratons

				Mid-Lithospheric Discontinuity				Lithosphere - Asthenosphere Boundary			
Craton	**Code**	**Bounces**	**Moho** (±4 km)	**Depth** (km)	**Bounds** (km)	**% Vs** (km/s)	**Gaussian Width** (±2σ km)	**Depth** (km)	**Bounds** (km)	**% Vs** (km/s)	**Gaussian Width** (±2σ km)
North America	NA	3197	45	-	-	-	-	173	168 - 178	8 ± 2	24
Hudson Bay	Hudson-NA		49	78	74 - 82	5 ± 1	10	158	153 - 163	8 ± 2	28
South America	SA	2255	43	-	-	-	-	148	141 - 155	8 ± 3	30
Europe	EUR	1296	48	86	79 - 93	6 ± 2	15	190	182 - 198	9 ± 2	52
Siberia	SIB	2130	41	83	79 - 87	4 ± 1	6	130	126 - 134	7 ± 3	20
West Africa	WAF	546	40	100	95 - 105	4 ± 2	10	160	155 - 165	7 ± 3	14
South Africa	SAF	836	44	-	-	-	-	182	176 - 188	7 ± 3	14
Australia	AUS	288	35	121	118 - 124	6 ± 1	10	170	167 - 173	7 ± 3	14
Antarctica	ANT	1050	42	110	107 - 113	5 ± 1	12	163	159 - 167	7 ± 3	17
India	IND	241	37	-	-	-	-	-	-	-	-

4.4.1 Shape of the Velocity Gradient

We tested whether the two negative discontinuity operators could be represented by a single wide Gaussian operator. However, we could not model SS stacks, that have 2 negative discontinuities, with a single broad Gaussian operator. Broad Gaussian operators generally do not give a good fit to the data due to interference with the main SS pulse. This can be avoided using an asymmetric Gaussian operator, hereafter referred to as skewed Gaussian operator. A skewed / asymmetric Gaussian operator is defined as having two different slopes for the two legs of the Gaussian and a square function in between (dashed red line in Figure 4.7).

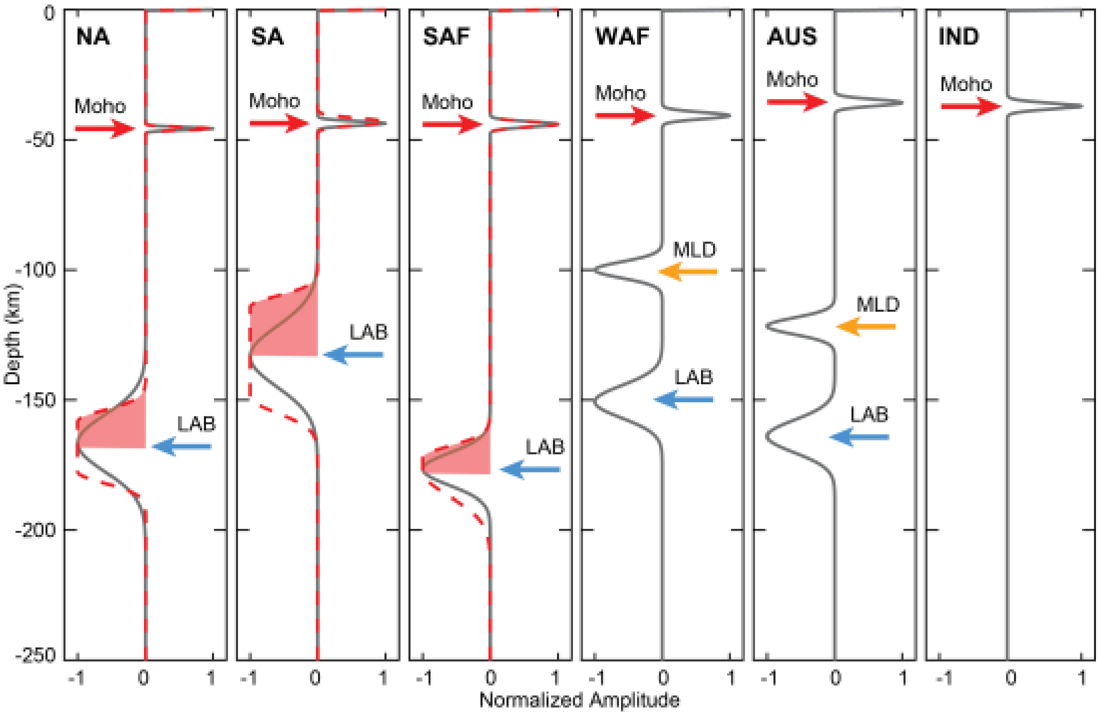

Figure 4.7: Cratons modeled using a skewed Gaussian operator. The NA, SA and SAF cratons could be equally well fit by both simple Gaussian (solid grey) and skewed Gaussian operator (dashed red). The red shaded area shows half the total velocity drop. The WAF, AUS and IND cratons could not be fit by a skewed Gaussian operator.

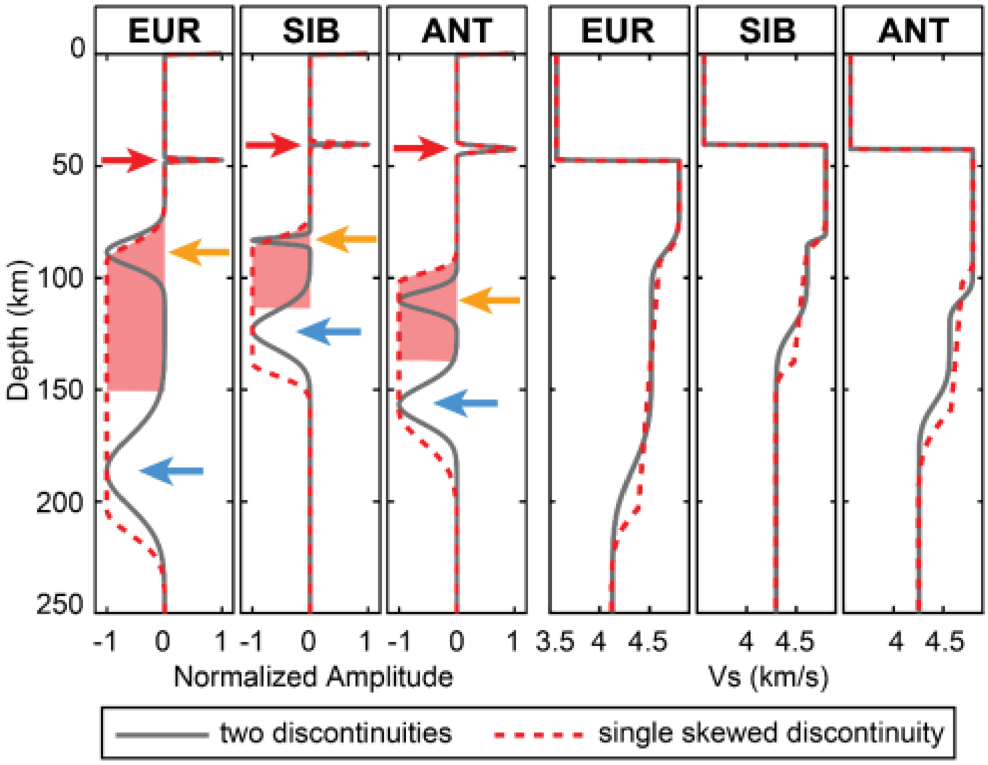

Figure 4.8: Cratons modeled using a skewed Gaussian operator. The double discontinuity (solid grey) beneath EUR, SIB and ANT cratons could be replaced by a single skewed Gaussian operator (dashed red). Velocity - depth structures corresponding to the Gaussian (grey) and skewed Gaussian (dashed red) functions for EUR, SIB and ANT are shown in right three panels. The red shaded area shows half the total velocity drop.

Our tests show that the two discontinuities beneath EUR, SIB and ANT could be replaced with a single skewed Gaussian operator (Figure 4.8). The two negative discontinuities beneath WAF, AUS and Hudson Bay – NA (not shown) stacks could not be resolved with a single skewed Gaussian operator. These craton stacks (EUR, SIB and ANT) are equally well fit by both a double discontinuity, i.e. two symmetric Gaussian operators, and a single skewed Gaussian operator (Figure 4.6, 4.8). The single skewed discontinuity is centered at ~150 km depth beneath EUR, ~115 km beneath SIB, and ~130 km beneath ANT. The discontinuity depth in this case is reported as the depth of half the total velocity drop. Beneath NA, SA and SAF cratons, both symmetric Gaussian and skewed Gaussian operators give similar results (Figure 4.7). A single skewed Gaussian operator could imply that the discontinuity could be varying in depth spatially across the entire craton. Overall the results for skewed and double discontinuity operator look very similar. This implies that while our constraints on discontinuity depths are robust, the exact shape of the velocity gradient is difficult to resolve (Figure 4.7).

4.5 Comparison to Previous Results

4.5.1 The Moho

The Moho depths estimated in our study are in excellent agreement, correlation coefficient of 0.87, with weighted average crustal thickness from CRUST1.0 (Laske et al., 2012) (Figure 4.9a). The large uncertainty in the SS depth, < ±4 km, likely reflects lateral variation in crustal thickness within the large craton bouncepoint bins, as evidenced in error bars based on variability in CRUST1.0 within the bouncepoint bins (Figure 4.9a). Our Moho depths are also in good agreement with receiver function studies. For example, we image a 45 km thick crust beneath NA and 49 km thick crust beneath Hudson Bay – NA craton stack compared to a Moho at 30 – 52 km beneath NA from *Ps* - *Sp* receiver functions (Abt et al., 2010; Rychert et al., 2007). Similarly, we image a Moho at 48 km compared to a Moho at 30 – 50 beneath EUR (Geissler et al., 2010). Beneath SIB receiver functions image a Moho at 40 – 48 km (Cherepanova et al., 2013) compared our result at 41 km depth. Receiver functions image a 38 ± 5 km Moho beneath SA (Assumpcao et al., 2013) compared to a Moho at 43 km that we image. We also image a Moho at 35 km compared to 30 – 43 km from *Ps* receiver functions beneath AUS (Ford et al., 2010). Finally, the Moho we image at 44 km depth beneath SAF is comparable to a Moho at 38 – 57 km from receiver functions (Nguuri et al., 2001).

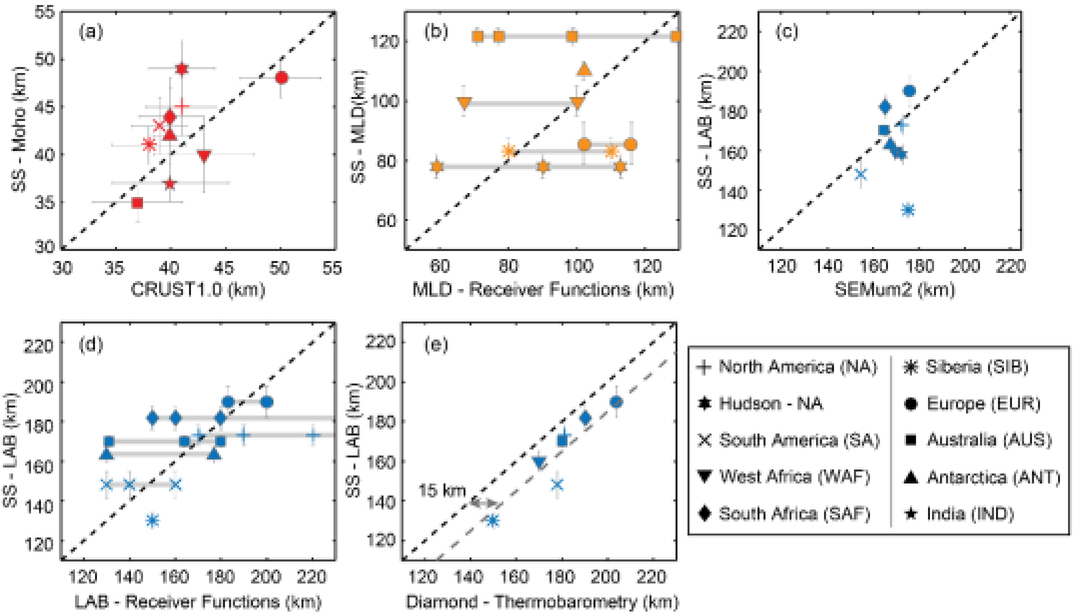

Figure 4.9: (a) Moho depths compared to average crustal thickness from CRUST1.0 (Laske et al., 2012) (b) MLD depths compared to receiver function studies (see text for references) (c) LAB depths compared to depth of the maximum negative gradient in Voigt average shear velocity in SEMum2 (French et al., 2013) (d) LAB depths compared to receiver function studies (see text for references) (e) LAB depths compared to depths estimated from diamond thermobarometry. The grey rectangular bars in (b, d) show the depth range of discontinuities observed using receiver functions.

4.5.2 Shallow Negative Discontinuity (80 – 121 km)

The negative discontinuities we image at 80 – 121 km depth, with an average velocity contrast of 4 – 6 ± 1% occurring over <15 km beneath 7 out of 10 cratons, are in general agreement with the depth and sharpness of negative discontinuities imaged by receiver functions beneath continental cratons globally and frequently termed MLDs (Abt et al., 2010; Ford et al., 2010; Foster et al., 2014; Kumar et al., 2013) (Figure 4.9b). we image a negative discontinuity at 83 ± 4 km beneath SIB in agreement with receiver functions that report a discontinuity at 80 – 110 km depth (Rychert and Shearer, 2009). We image a discontinuity at 100 ± 5 km depth beneath WAF in agreement with discontinuities at 67 – 100 km depth reported by receiver functions (Di Leo et al., 2015; Rychert and Shearer, 2009). We resolve a discontinuity at 110 ± 3 km depth beneath the ANT craton, just deeper than that from receiver function at 102 km depth (Kumar et al., 2007). We do not image a negative discontinuity beneath the entire NA craton but resolve a discontinuity at 78 ± 4 km in the Hudson Bay – NA craton stack (Figure 4.6). This is consistent with *Ps* and *Sp* receiver functions that image a sparse negative discontinuity at 59 – 113 km depth, primarily in the NE-E part of North America (Abt et al., 2010; Foster et al., 2014).

Beneath the EUR craton we image a discontinuity at 86 ± 7 km depth, ~10 km shallower than similar negative discontinuities reported by receiver functions at 102 – 116 km depth (Geissler et al., 2010). *Sp* receiver functions image a discontinuity at 69 ± 8 to 85 ± 14 (Ford et al., 2010) compared to the discontinuity we image at 121 ± 3 km depth beneath AUS (Figure 4.9b). Receiver functions report a negative discontinuity at 85 km beneath SAF (Sodoudi et al., 2013). However, we do not resolve a discontinuity internal to the lithosphere at 80 – 121 km depth beneath SAF in our SS waveforms. The discrepancy between our results and discontinuity depths from receiver functions beneath EUR, AUS and SAF is likely caused by a difference in sensitivity. Our SS waveforms represent a broad average for the craton, while receiver functions give information over a smaller area beneath seismic station locations. Receiver functions also image a discontinuity at 60 – 90 km depth beneath IND (Kumar et al., 2013; Saul et al., 2000). However, we have no resolution of the discontinuity structure of IND beneath the Moho, which may be due to less number of SS waveforms and/or noisy data.

4.5.3 Deep Negative Discontinuity (> 130 km)

Out results for the deeper discontinuity at 130 – 190 km depth are in general agreement with the depth of the sharpest negative gradient in Voigt average shear velocity (154 – 176 km) in a global surface-wave model (French et al., 2013) (hereafter referred to as SEMum2) (Figure 4.9c). There is poor correlation (0.21) between our depth estimates to those from SEMum2, but the correlation is stronger, 0.76, when SIB is excluded. The discontinuity we image at 130 km beneath SIB is ~50 km shallower than observed in SEMum2. Other surface-wave studies image seismically fast anomalies that extend to 200 – 300 km depth (Debayle et al., 2016; Kustowski et al., 2008; Nettles and Dziewonski, 2008; Schaeffer and Lebedev, 2013). However, the depth of the sharpest negative gradient in Voigt average shear velocity (150 – 200 km) from these studies is in general agreement with our results for the deeper discontinuity, except SIB where our result is consistent shallower by ~50 – 60 km depth.

Our discontinuity depth results are also in good agreement (correlation of 0.64) with receiver functions (Figure 4.9d) that image similar negative discontinuities at 150 km depth beneath SIB (Oreshin et al., 2002), 130 – 160 km beneath SA (Heit et al., 2007), 130 – 177 km beneath ANT (Kumar et al., 2007), and also with weak negative phases reported at 182 – 200 km depth beneath EUR (Geissler et al., 2010). We also image a discontinuity at 167 km depth beneath NA, just shallower than the LAB reported by *P*-to-*S* receiver functions at 170 – 230 km depth (Bostock, 1998; Snyder, 2008). Our result from SAF at 176 km depth is also comparable to most discontinuities reported by receiver function studies at 150 – 200 km (Hansen et al., 2009; Savage and

Silver, 2008; Sodoudi et al., 2013; Wittlinger and Farra, 2007; Wolbern et al., 2012). One study suggests a much deeper negative discontinuity at 257 – 293 km depth beneath SAF (Kumar et al., 2007), although our results do not evidence such a feature. Our result from AUS at 164 km depth agrees with one receiver function result at 164 – 180 km (Kumar et al., 2007), although not with another study that imaged a discontinuity at the edge of the AUS craton at 131 km depth, with no deeper discontinuity beneath the craton (Ford et al., 2010). The negative result was interpreted as a LAB velocity gradient that was too gradual, > 60 km, to be detected by receiver functions (Ford et al., 2010). Our result suggests a sharper discontinuity. One possibility is that the discontinuity is anisotropic; the sensitivity of receiver functions and SS phases to anisotropy is different. We do not image a negative discontinuity beneath IND, possibly due to too few waveforms from this cratonic region. IND has the lowest number of waveforms at 241.

The discontinuity we image is strong, 7 – 9 ± 2%, and strong, occurring over < 15 km. This is in contrast to some surface wave studies that suggest a low-velocity zone may not exist beneath some cratons, in other words, seismic velocity may not decrease with depth (Gaherty and Jordan, 1995; Pedersen et al., 2009). In addition, it is sharper than the gradient in surface wave studies that do image a velocity decrease with depth, e.g., 5% over ~110 km (French et al., 2013). In comparison, we image a 7 – 9% velocity drop, the majority of which occurs over < 15 km (±1σ Gaussian half-width), with 95% occurring over < 30 km (±2σ Gaussian half-width or 4σ Gaussian width). Only our EUR result is more gradual, over < 52 km. however, the apparent discrepancy in the sharpness between surface waves and our result could likely be explained by the broad depth sensitivity of the surface waves, which could also be satisfied with a sharper discontinuous structure with a similar average velocity (lithosphere averaged with asthenosphere) over the depth range.

4.6 Discussion

Overall, our SS precursors suggest a discontinuity that is consistently present beneath continental interiors in contrast to the sparse and sometimes discrepant detection by receiver function imaging. This is easily explained for certain discontinuity properties. For instance, the 150 – 200 km depth range is contaminated by Ps crustal reverberations for ~40 km thick cratonic Moho, which would mask true discontinuities in this range. In addition, the depth range over which this discontinuity occurs (~30 km) means that the strength of the discontinuity would be diminished by ~60 % in high frequency Ps and Sp imaging making it difficult to detect above the noise (Rychert and Shearer, 2010). Similarly, depth discrepancies are likely explained by the different sensitivities of the waveforms.

A gradual reduction in seismic velocity from 100 – 220 km occurs in some surface wave models beneath the cratons (French et al., 2013), which is likely where our SS imaging would detect the LAB discontinuity if it exists. Our result is well-correlated, 0.76, with the depth of the sharpest gradient in Voigt shear velocity when SIB (the outlier) is excluded, or 0.80 when we consider the possible deeper SIB discontinuity (Supplementary Information) (Figure 4.9c) (French et al., 2013). This agreement suggests that our results likely reflects the base of the continent detected by surface waves, but also that the transition is sharper (<30 km) than that of the surface wave models (~100 km) (Debayle et al., 2016; French et al., 2013; Nettles and Dziewonski, 2008; Schaeffer and Lebedev, 2013). This is in contrast to some surface wave studies that suggest a low-velocity zone may not exist beneath some cratons (Gaherty and Jordan, 1995; Pedersen et al., 2009).

Our LAB discontinuity is not defined by temperature or anisotropy alone. The sharpness of our discontinuity (<30 km depth) is inconsistent with thermal gradients between the lithosphere and asthenosphere in geodynamic models which generally occur over >70 km depth (Cooper et al., 2004; Korenaga and Jordan, 2002). Although anisotropy is likely important at the LAB (Yuan and Romanowicz, 2010) it does not likely define our observation on its own. A change in azimuthal anisotropy would be accompanied by a change in polarity with back-azimuth (Rychert et al., 2014), which is not observed. In addition, an increase in radial anisotropy with depth is not a likely explanation since recent surface wave models beneath the continents suggest decreasing radial anisotropy ($V_{SH} > V_{SV}$) with depth beneath the continents (Nettles and Dziewonski, 2008; Sebai et al., 2006; Yuan and Romanowicz, 2010).

Our LAB discontinuity is not defined by composition alone. Xenolith compositions suggest that the cratons are depleted at shallow depth with greater fertility deeper. However, our velocity drop is also too large to be explained by typical continental composition depletion, which might be up to ~1% (Schutt and Lesher, 2006). Additional effects from hydration as a defect in olivine (Hirth and Kohlstedt, 1996; Karato and Jung, 1998) are also likely small at the cold temperatures within a continent (Behn et al., 2009). Our discontinuity also occurs at deeper depths than proposed for elastically accommodated grain boundary sliding (~60 – 150 km) (Karato et al., 2015). It has also been suggested that the deep mantle beneath the continents has been metasomatized, with hydrated minerals and slower seismic velocities.

However, such enrichment in volatiles such as water and CO_2, which would effectively lower the melting temperature of the mantle, and likely facilitating the formation of carbonated melt.

To consider the possibility of melt in greater detail, we collated P-T estimates for xenoliths beneath three regions where textural information was available: Slave, South Africa and Siberia. Geothermobarometry indicates a geotherm consistent with steady conductive cooling down to depths of 150 – 200 km, with deeper xenoliths having higher temperatures significantly greater than the predicted geotherms. These deeper xenoliths also generally lie above the carbonate–silicate solidus. Therefore, if the deeper, higher temperature xenoliths are also more metasomatised, and more fertile, as they are for instance beneath Kaapvaal (Eaton et al., 2009), then they would also be melted.

Our deeper discontinuity depths are well correlated, 0.93, with the depth extent of the lithosphere from diamond thermobarometry suggesting it is closely related to the base of the plate (Figure 4.9e). We used the diamond bearing xenolith *PT* data to estimate the lithospheric thickness assuming crustal thicknesses from our SS Moho results, a crustal density of 2600 kg/m3 and a mantle density of 3330 kg/m3. In cratons where multiple diamond bearing xenoliths have been analyzed giving a range of pressures, we used the highest reported pressure, which likely represents the extent of the cold, stable, craton, assuming diamonds in the convecting mantle would cross the diamond-graphite transition. Our estimates of lithospheric thicknesses from diamond bearing xenoliths are 181 km – NA (Eaton et al., 2009), 204 km – EUR (Eaton et al., 2009), 150 km – SIB (Pearson et al., 1995), 178 km – SA (Tappert et al., 2006), 170 km – WAF (Hills and Haggerty, 1989), 190 km – SAF (Boyd and Gurney, 1986), and 180 km – AUS (Tappert et al., 2011). Diamonds that have erupted in recent geologic history, constrain the depth extent of the rigid lithosphere. Since diamonds are only stable at cold temperatures, their billion year ages suggest that the continents are rigid to the depths from which they originate. Indeed, xenoliths from shallow depths are typically coarse grained and less deformed than those from deeper depths, and this textural change has been interpreted as the transition between the stable continental lithosphere to the convecting mantle at depth (Figure 4.10). Our SS results are consistently shallower (~15 km) than the lithospheric thicknesses estimated from diamond thermobarometry (Figure 4.9e), suggesting that the rigid continents persist just beneath the discontinuity before the mantle beneath decouples and convects.

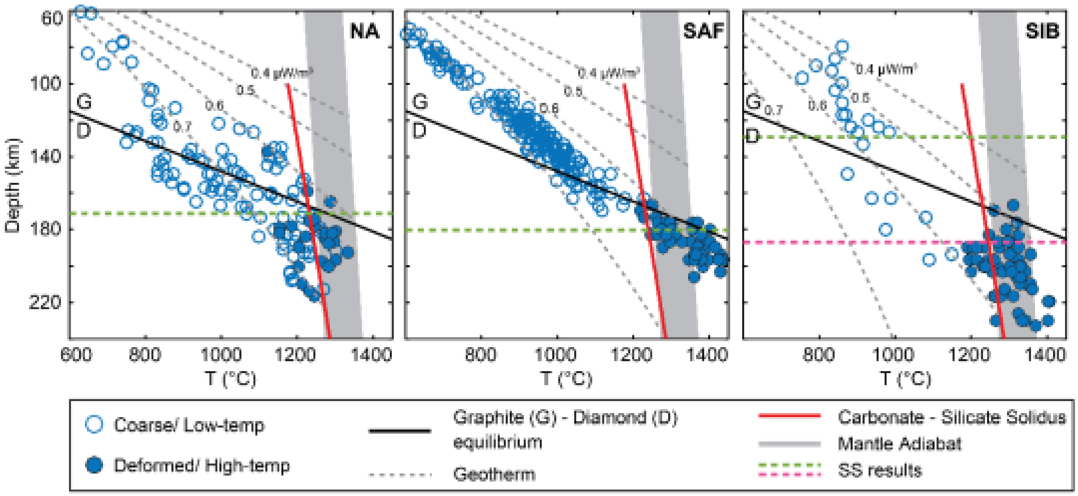

Figure 4.10: Depth–Temperature relations for xenoliths from NA, SAF and SIB. Continental conductive geotherm (dashed grey line), after Rudnick et al., 1998. Geotherms terminate in a mantle adiabat from 1200 – 1300 ˚C (shaded grey region). The graphite (G) – diamond (D) equilibrium (solid black line) is that of Kennedy and Kennedy, 1976. The carbonate – silicate solidus (solid red line) is that of Thompson et al, 2016. SS LAB results are indicated by dashed green and dashed magenta lines.

If small degrees of carbonated-silicate melts are present today beneath the continents it could explain both the seismic anomaly and also define the base of the continental lithosphere. Melt has a strong effect on shear velocity, potentially reducing the velocity by 7.9% for 1% partial melt (Hammond and Humphreys, 2000). The presence of partial carbonate-silicate melt, may enhance mantle deformation, effectively lowering the viscosity (Faul, 1997; Hirth and Kohlstedt, 1995). Greater melt percentages may exist with depth, as the geotherm becomes increasingly greater than the solidus. The systematic difference in depth between the deepest diamonds and the seismic discontinuity may be caused by a lag between the melt percentage needed to reduce the seismic velocity and that required to reduce mantle viscosity to the point where convection dominates.

4.7 Conclusions

Our SS precursor inversions constrain three seismic discontinuities within the cratonic lithosphere globally. We image a positive discontinuity at 35 – 50 km depth beneath all cratons, consistent with a thick continental crust. We image a sharp negative discontinuity, an average velocity contrast of 5 ± 1.5% occurring over <14 km, in the 80 – 121 km depth range beneath some cratons, likely an MLD (Figure 4.5, 4.6). Its depth, magnitude, sharpness and sparse detection are likely explained by compositional layering, possibly due to metasomatism. We image an ~8% velocity drop at 130 – 190 km depth globally beneath all well-resolved cratons. The depth is well correlated with the deepest reported, relatively undeformed diamond bearing xenoliths, i.e. a transition from coarse to deformed xenolith textures. This textural change has been interpreted as the transition between the stable continental lithosphere to the convecting mantle at depth (Figure 4.10). Small degrees of carbonated – silicate melts present today beneath the continents could explain both the seismic anomaly and also define the base of the continental lithosphere. In conclusion, our SS precursor results suggest the existence of partial melt beneath the chemical lithosphere defines the tectonic plate, and provides a unified petrological and seismic continental thickness.

Supplementary Information

S1. SS Modeling of Siberia

Beneath Siberia the deepest discontinuity we resolve is at ~130 km depth, significantly shallower than the deepest diamond bearing xenolith at ~150 km (Figure 4.9e) (Pearson et al., 1995) and the transition to coarse textured xenoliths at ~180 km (Figure 4.10).

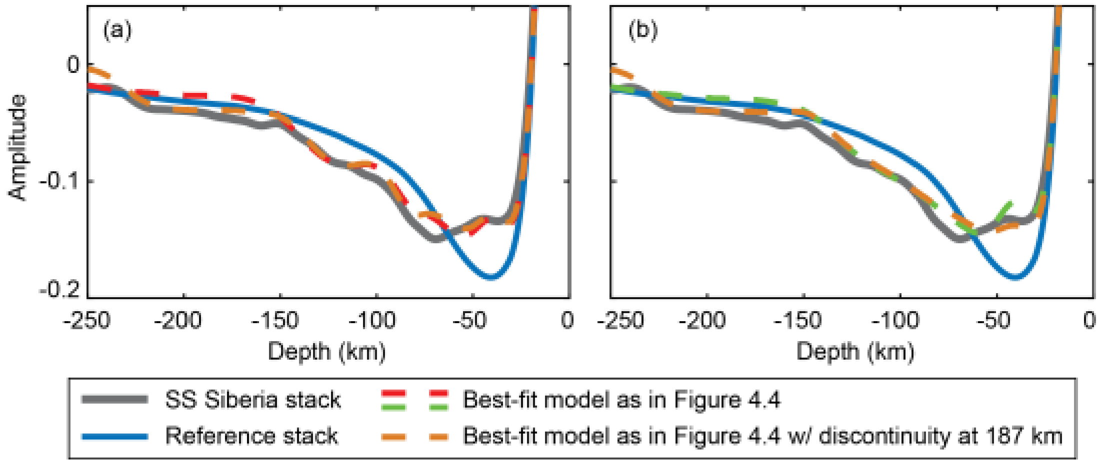

Figure 4.11: Waveform fits for SS Siberia stack (solid grey) modeled with an additional deeper discontinuity at 187 km. (a) Discontinuities at 83 km and 130 km modeled using two symmetric Gaussian operators. (b) Discontinuities at 83 km and 130 km modeled using a single skewed Gaussian operator centered at 115 km depth.

We also observe a much deeper negative discontinuity phase in our SS Siberia stack in comparison to the reference waveform. We model this negative phase using a symmetric Gaussian and a skewed Gaussian operator, discussed in previous sections. Our tests indicate that a discontinuity is required to fit the data at 187 ± 2 km depth with a velocity contrast of 3 – 4% occurring over < 20 km (±2σ Gaussian width) (Figure 4.11). Although we were able to fit the SS data better, we were not able to achieve a statistically significant fit. That is to say that adding a discontinuity at 187 km depth does not significantly improve the fit to the data in comparison to a model with a discontinuity at shallower depths (130 km), as determined by F-Test (Hosmer et al., 1997). However, this discontinuity at 187 km is in better agreement with the transition from coarse to deformed xenoliths beneath Siberia (dashed magenta line, Figure 4.10). One possible explanation is that the discontinuity at 187 km is laterally variable in depth over the large area sampled by our SS waveforms, resulting in a relatively low amplitude pulse in the SS stack. Thus the seismic discontinuity at 187 km likely represents the continental lithosphere-asthenosphere boundary beneath Siberia and the discontinuity at 130 km is internal to the lithosphere.

S2. Geotherms

The continental geotherms (Figure 4.10) are calculated after Rudnick et al., 1998. For our calculation we use a crustal thickness of 45 km for NA, 44 km for SAF, and 41 km for SIB based on our SS results. We use a constant crustal density of 2800 kg/m^3, crustal thermal conductivity of 2.6 W/m°C, crustal heat production of 0.6 μW/m^3, mantle density of 3300 kg/m^3, mantle thermal conductivity of 2.8 W/m°C, mantle heat production of 0.03 μW/m^3 (Rudnick et al., 1998). We use surface heat flow of 46 mW/m^2 for NA (Jaupart and Mareschal, 2015), 45 mW/m^2 for SAF (Jaupart and Mareschal, 2015), and 40 mW/m^2 for SIB (Mareschal and Jaupart, 2013).

S3. Xenolith Data Sources

The xenoliths *PT* and texture data was compiled from literature for NA, SAF and SIB cratons (Figure 4.10). Where possible we recalculated the *PT* of xenoliths using the method of *Nimis and Grutter, 2010* (Nimis and Grutter, 2010).

Siberia:

F. R. Boyd. *Geology* **12**, 528-530 (1984)

F. R. Boyd *et al. Contrib Mineral Petr* **128**, 228-246 (1997).

A. M. Agashev *et al. Dokl Earth Sci* **432**, 746-749 (2010).

N. S. Tychkov *et al. Dokl Earth Sci* **454**, 84-88 (2014).

South Africa:

H. Grutter, R. Moore. *Extended abstract, Eighth International Kimberlite Conference*, 272 (CD-ROM) (2003) and references therein.

D. W. Eaton *et al. Lithos* **109**, 1-22 (2009).

North America:

J. Kjarsgaard, T. D. Peterson. *Current Research, Geological Survey of Canada* **92-1B**, 6 (1992).

M. G. Kopylova *et al. J. Petrol.* **40**, 79-104 (1999).

S. S. Schmidberger, D. Francis. *Lithos* **48**, 195-216 (1999)

H. Grutter, R. Moore. *Extended abstract, Eighth International Kimberlite Conference*, 272 (CD-ROM) (2003) and references therein.

Page intentionally left blank.

Chapter 5

Conclusions

5.1 Summary of Observations

SS precursors were used to image the seismic discontinuity structure and velocity gradients beneath three unique tectonic environments, the Ontong Java Plateau, the Pacific Ocean, and the cratons.

Firstly, SS precursors image three discontinuities beneath northern OJP, a positive Moho discontinuity at 28 ± 4 km depth, a negative discontinuity at 80 ± 5 km discontinuity, and a deeper negative discontinuity at 282 ± 7 km depth. The Moho result suggests that thickened crust exists over a large lateral area of the northern OJP sampled by SS waveforms. The deeper negative discontinuity at ~282 km depth is not observed in the Pacific Ocean stacks (see chapter 3), which suggests that the region may be anomalous to these depths. The persistence of such anomalous structures to ~282 km depth beneath OJP, despite traversing for 1000s of kilometers since formation, suggests the existence of a viscous root. This deep discontinuity could potentially be related to its base. The shallower negative discontinuity at ~80 km is similar and may be related to discontinuities observed across the Pacific at 60 – 110 km depth (chapter 3). If it exists in a viscous root, the 80 km discontinuity bears some similarity to the MLDs observed beneath continents (chapter 4). The 80 km discontinuity beneath OJP may be a compositional boundary, a result of previous large melting events. The seismic structure of the OJP, together with its formation and evolution history, suggests that large plume melting events may cause discontinuities in the MLD depth range.

Secondly, a sharp pervasive discontinuity across the Pacific at 30 – 80 km depth with a 3 – 15 % shear velocity drop over < 21 km in depth was imaged. The discontinuity depth was found to increase with age from the ridge to 36 ± 9 My according to conductive cooling along the 1100 °C isotherm. Beneath older seafloor, > 36 My, the discontinuity was imaged at a mean depth of 60 ± 1.5 km with no apparent age dependence. The velocity contrast is sharper than expected from thermal models, suggesting that some other mechanism may be required along with temperature to explain this discontinuity. Accumulation of melt at a permeability boundary, controlled by the solidus depth, could explain the sharp discontinuity beneath young seafloor. The discontinuity beneath old seafloor could be explained by a compositional boundary from a strong pervasive frozen-in melt signature. In this case, the discontinuity may not necessarily be the LAB, but the pervasive compositional variation would probably influence mantle rheology and the LAB transition. Melt could also explain the discontinuity beneath older ages under special circumstances, i.e. if thin layers of carbonatitic melt form as in the "millefeuille" model, and/or coalesces at a permeability boundary. In this situation, the melt would likely weaken the mantle, and the boundary would then represent the LAB.

A second deeper, intermittent discontinuity at 80 – 120 km depth with a 4% shear velocity drop over < 11 km was imaged. This discontinuity had no apparent age – depth dependence. In many cases, it could represent continually decreasing velocity in concert with the shallower feature, although a distinct, velocity drop at depth is sometimes required. An anisotropic component related to complicated mantle flow could modulate the amplitude and shape of this feature, and explain its intermittency.

Finally, SS imaging constrains three seismic discontinuities beneath cratons; a Moho, an MLD and an LAB. All cratons are characterized by a positive discontinuity at 35 – 50 km depth, consistent with a thick continental crust. The ±4 km error bounds on the Moho depths suggest lateral variation in crustal thickness over a wide area sampled by the SS waveforms.

The results presented in chapter 4 suggest that MLD is not a global feature. The MLDs were observed beneath some cratons 80 – 121 km depth with an average shear velocity drop of 5 ± 1% occurring over <15 km depth. The depth, magnitude, sharpness and sparse detection of the MLD could be explained by compositional layering, possibly due to metasomatism, which likely causes lateral variation in radial anisotropy. All cratons are characterized by a deeper discontinuity at 130 – 190 km depth, with an average shear velocity drop of 8% occurring over < 30 km depth, in contrast to the sparse and sometimes discrepant detection by receiver function imaging. The only exception is India where no discontinuity structure was resolved beneath the Moho, possibly due to less and/or noisy waveforms in the stack. The SS results for the deep, > 130 km depth, discontinuity is well correlated with the depth extent of the lithosphere from diamond thermobarometry, suggesting it is closely related to the base of the plate. In addition, SS discontinuity depth results are also coincident with the transition from coarse to deformed xenolith textures. If small degrees of carbonated-silicate melts are present today beneath the continents, it could explain both the seismic anomaly and also define the base of the continental lithosphere, providing a unified petrological and seismic continental thickness.

In conclusion, the essence of the SS precursor imaging of the lithosphere presented in chapters 2 – 4 is to image the base of the lithosphere and estimate its thickness. The seismic base of the lithosphere imaged in this thesis is closely related to the thermal, mechanical, chemical, and electrical LAB described in chapter 1. However, directly connecting these LAB proxies is not straightforward. For example, it has been demonstrated in this thesis that the SS precursors image discontinuities in the Pacific that are in similar depth range to the discontinuities previously imaged using receiver functions (Kawakatsu et al., 2009; Kumar and Kawakatsu, 2011), converted waves (Gaherty et al., 1999; Tan and Helmberger, 2007), electrical resistivity / conductivity (Baba et al., 2006; Evans et al., 2005; Evans et al., 1999), and discontinuity depths estimated from experimental predictions of seismic velocities (Jackson and Faul, 2010). However, different causative mechanisms have been proposed to explain these discontinuities including compositional variation (Gaherty et al., 1999; Tan and Helmberger, 2007), elastically accommodated grain boundary siding (Karato, 2012), and partial melt (Kawakatsu et al., 2009; Kumar and Kawakatsu, 2011; Schmerr, 2012). Overall, seismic imaging using SS precursors provides tighter constraints on the depth, magnitude and sharpness of the lithospheric discontinuities beneath the Ontong Java Plateau, the Pacific Ocean and the cratons. The results presented here also provide constraints on the likely mechanisms that define these three unique tectonic environments, taking into perspective various ideas that have been proposed over the years, giving us an insight into the formation and evolution history of the Ontong Java Plateau, the Pacific Ocean and the cratons.

5.2 Future Work

The Ontong Java Plateau, the Pacific Ocean and the cratons represent only a fraction of the different tectonic environments that exist globally. Globally imaging the lithospheric and upper mantle seismic discontinuity structure beneath all tectonic settings, such as mid-ocean ridges, subduction zones, ocean basins and continents in a self-consistent way is required to fully understand the nature, evolution and defining mechanism of the lithosphere – asthenosphere system.

The next logical approach is to seismically image the discontinuity structure beneath the Atlantic and the Indian Oceans. Constraining the discontinuity structure beneath all the three ocean basins could give us an insight into the mechanisms that define and characterize them, and also help us better under mantle dynamics beneath these ocean basins.

As demonstrated in this study, SS precursors offer a powerful tool to self-consistently image the discontinuity structure beneath different tectonic environments. However, characterizing fine scale features is not straightforward due to the long periods used in this study. Although multiple discontinuities were imaged beneath the Ontong Java Plateau, the Pacific Ocean and the cratons, not all multiple discontinuities were unique. For example, some Pacific Ocean bins and craton bins could be equally well resolved by a single skewed Gaussian operator and a double discontinuity operator. Resolving the exact shape of the velocity gradient is not straightforward. One possible approach is to stack the SS waveforms in smaller bounce point bins and image the lithospheric discontinuity structure at shorter periods. This could possibly isolate the two discontinuities, if present, and help better characterize the shape of the velocity gradient. Further, stacking waveforms in smaller bouncepoint bins could likely constrain the lateral variation in discontinuity structure. The method could be improved by incorporating multi-taper deconvolution or simultaneous deconvolution, similar to receiver functions, to enhance the precursor phases.

Such a technique could provide better images of the global lithosphere and upper mantle discontinuity structure. Better constraints on the depth, magnitude and sharpness of these lithospheric and upper mantle discontinuities globally could help us better understand the formation, evolution of the ocean basins and continents. This can help us better understand mantle dynamics and possibly the evolution of Earth itself.

Appendix 1

Adaptive Difference Engine

A1.1 Introduction – Grid Search Algorithm

The goal of waveform modeling is to find the set of parameters that results in a synthetic that best fits the data. This becomes a problem of optimization, the objective of which is to maximize a systems desirable properties while simultaneously minimizing its undesirable characteristics. For SS waveform modeling, the desirable property or the objective function is to reduce the residual between the synthetic and the data. The simplest and most commonly used optimization technique is the Brute Force Search or Grid Search algorithm.

If a lithospheric operator is defined by a delta function, the objective is to find a set of depths (precursor arrival times) and amplitudes (velocity contrast) that best describes the data. The grid search algorithm visits all grid points in a bounded region and stores the points that give a statistically significant model and describes the data. Even though generating a sequence of grid points is trivial, the model suffers from the step-size problem. Deciding the grid size is subjective. If the grid is too coarse, the optimum may be missed. If the grid is too fine, computing time explodes exponentially because a grid with N points in one dimension will have N^D points in D dimensions. The problem is further aggravated if multiple discontinuities need to be resolved. This is called the "Curse of Dimensionality".

Various techniques have been developed to optimize the grid search algorithm including *Random Walk* (Gross et al., 2008) that samples the objective function value at randomly generated points; *Hooke – Jeeves* method (Hooke and Jeeves, 1961) also known as *direction* or *pattern search*; *Simulated Annealing* (Kirkpatrick et al., 1983) samples objective function surface by modifying the search criterion to accept some uphill moves while continuing to accept all downhill moves; and *Nelder – Mead Polyhedron search* (Nelder and Mead, 1965) allows the step size to expand or contract as needed. Although these techniques have evolved to be more effective than the grid search algorithm, they suffer from the "Curse of Dimensionality" when multiple parameters need to be optimized simultaneously.

A1.2 Differential Evolution and the Adaptive Difference Engine

An intuitive way of solving optimization problem is to use Evolution strategies (Rechenberg, 1973; Schwefel, 1994) that attempt to evolve better solutions through recombination, mutation and survival of the fittest. Differential Evolution, a numerical optimizer developed by *Price and Storn* (Price et al., 2005; Storn and Price, 1997), is a population – based optimizer that samples the objective function at multiple, randomly chosen initial points. Bounds of parameter space define the region from which this initial population (P_i) is chosen (Figure A1a), where $\boldsymbol{i}$ is the index of the population vector. The Population vector is represented by a set of number from 1 – 11 in figure A1a.

New points are generated that are perturbations of the existing points. But unlike other optimization strategies, these perturbations are neither reflections like those in Controlled Random Search and Nelder–Mead methods nor samples from a predefined probability density function like those in evolution strategies. Rather, perturbations are generated using a scaled difference of two randomly selected population vectors (z_1, z_2) (Figure A1 b). The scaled difference vector, $F.(z_1 - z_2)$, is added to a third randomly

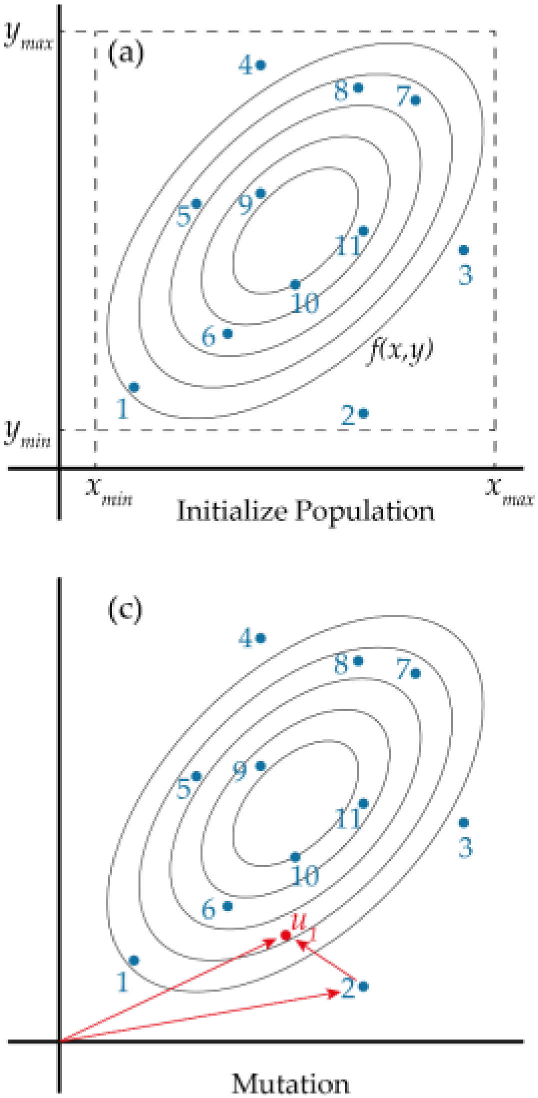

Figure A1: Graphical representation of the Differential Evolution Algorithm. Elliptical contours represent the function f(x,y) (a) population is generated from a bounded parameter space (b) two randomly selected population vectors (z_1, z_2) are used to generate a weighted difference vector, $F.(z_1 - z_2)$ (c) a trial or mutant vector (u_1) is created by adding the weighted difference vector to a third randomly selected population vector, z_3 (d) the mutant vector competes with the population vector of same index to achieve the lower objective function value. The survivors become parents for the next generation of the evolutionary cycle.

selected population vector (z_3) to generate a trial vector (Figure A1 c). F is the scaling factor. This stage is called Mutation and the trial or mutant vector (u_1) is given by $u_1 = z_3 + F.(z_1 - z_2)$. The trial vector ($u_1$) competes against the population vector of same index to achieve the lower objective function value. The survivors of the pairwise competition between the trial and the population vector become parents (population) for the next generation in the evolutionary cycle (Figure A1 d).

A1.2.1 Population Structure

The population vector for a differential evolution is initialized by defining the lower and upper bounds of a parameter. For example, a negative discontinuity operator, defined by a step function, can vary in depth and amplitude. Therefore, the population vector contains *Np* elements in 2- dimensions, of which one dimension is the depth and the other amplitude. A random number generator is used to assign each parameter of every vector a value from within the prescribed range. The initial population is defined by

$$\boldsymbol{z_{i,j,g} = rand_{i,j,g}(0,1)\,.\left(b_{i,U} - b_{i,L}\right) + b_{i,L}} \qquad (\boldsymbol{A1.E1})$$

Where, $\mathbf{z}$ is an element of the population vector ($\boldsymbol{P}$) and $\boldsymbol{b}$ is the bounds of a parameter. Subscripts $\boldsymbol{U}$ and $\boldsymbol{L}$ indicate upper and lower bounds. Index $\boldsymbol{i}$, $\boldsymbol{j}$, $\boldsymbol{g}$ indicates the $\boldsymbol{i}^{th}$ element, $\boldsymbol{j}^{th}$ parameter and the generation to which a vector belongs. Index $\boldsymbol{i}$ ranges from 0 to *Np*-1 and index $\boldsymbol{g}$ ranges from 0 – g_{max}. The random number generator, ***rand(0,1)***, returns a uniformly distributed random number from within the range [0,1) for each element of a parameter.

A1.2.2 Mutation

Once the population is initialized, the differential evolution algorithm mutates and recombines the population to produce a population of *Np* trial vectors. During mutation, a scaled, randomly sampled, vector difference is added to a third vector. The following equation is used to generate a mutant vector, $\mathbf{u}_{j,g}$.

$$\boldsymbol{u_{i,j,g} = z_{r0,j,g} + F\left(z_{r1,j,g} - z_{r2,j,g}\right)} \qquad \boldsymbol{(A1.E2)}$$

The scaling factor, $\boldsymbol{F} \in (\boldsymbol{0}, \boldsymbol{1+})$, is a positive real number that controls the rate at which the population evolves. While there is no upper limit on $\boldsymbol{F}$, trial and error was used to determine the best value of F for waveform modelling. Since the objective of waveform modeling is to find the best fitting operator in a dense parametric space, the optimum value of F is found to be < 1 through trial and error. The Adaptive Difference Engine has been designed to dynamically vary the scaling factor to increase its effectiveness in finding the optimum solution (Price et al., 2005). But for the purposes of SS waveform modelling, the scaling factor has been fixed to an optimum value of 0.3.

A1.2.3 Crossover

The Adaptive Difference Engine employs discrete recombination, also called uniform crossover, to complement evolution search strategy. The crossover probability, $Cr \in [0,1]$, is a user-defined value that controls the fraction of parameter values that are copied from the mutant. To determine which source contributed a given parameter, uniform crossover compares *Cr* to the output of a uniform random number generator. If the random number is less than or equal to *Cr*, the trial parameter is inherited from the mutant, $\mathbf{u}_{i,j,g}$. If the random number is greater than *Cr*, the parameter is copied from its current population ($\mathbf{z}_{i,j,g}$) to the mutant. Uniform crossover ensures that each parameter, regardless of its location in the trial vector, has the same probability of inheriting its value from a given vector (Syswerda, 1989). The crossover probability, *Cr*, can also be thought of as a mutation rate as it dictates the probability of inheritance of parameters from a mutant or parent vector in a trial vector. The crossover probability used in this study is 0.3, which is the optimum mutation rate based on numerous tests (Storn and Price, 1997).

A1.2.4 Selection – Survival Criteria

Once the trial vector is generated using the crossover probability, it is compared to the target vector which is the population vector for the current generation. If the trail vector has an equal or lower objective function value than that of its target vector, it replaces the target vector in the next generation; otherwise, the target retains its place in the population for at least one more generation. Once the new population is installed, the process of mutation, recombination and selection is repeated until the optimum is located, or a pre-specified termination criterion is satisfied.

$$\boldsymbol{x_{i,j,g+1}} = \begin{cases} \boldsymbol{u_{i,j,g}} & \boldsymbol{if\ f(u_{i,j,g}) \leq f(x_{i,j,g})} \\ \boldsymbol{x_{i,j,g}} & \boldsymbol{otherwise} \end{cases} \qquad (\boldsymbol{A1.E3})$$

References

Abt, D.L., Fischer, K.M., French, S.W., Ford, H.A., Yuan, H.Y., Romanowicz, B., 2010. North American lithospheric discontinuity structure imaged by Ps and Sp receiver functions. J. Geophys. Res. 115.

Agashev, A.M., Pokhilenko, N.P., Cherepanova, Y.V., Golovin, A.V., 2010. Geochemical evolution of rocks at the base of the lithospheric mantle: Evidence from study of xenoliths of deformed peridotites from kimberlite of the Udachnaya pipe. Dokl Earth Sci 432, 746-749.

Aizawa, Y., Barnhoorn, A., Faul, U.H., Fitz Gerald, J.D., Jackson, I., Kovacs, I., 2008. Seismic properties of anita bay dunite: An exploratory study of the influence of water. J. Petrol. 49, 841-855.

Aki, K., Richards, P.G., 2009. Quantative Seismology, Second ed. University Science Books, California. ISBN 978-1-891389-63-4

Allen, J.C., Boettcher, A.L., 1983. The Stability of Amphibole in Andesite and Basalt at High-Pressures. Am Mineral 68, 307-314.

Artemieva, I.M., 2006. Global 1 degrees x 1 degrees thermal model TC1 for the continental lithosphere: Implications for lithosphere secular evolution. Tectonophysics 416, 245-277.

Artemieva, I.M., Mooney, W.D., 2001. Thermal thickness and evolution of Precambrian lithosphere: A global study. J. Geophys. Res. 106, 16387.

Assumpcao, M., Feng, M., Tassara, A., Julia, J., 2013. Models of crustal thickness for South America from seismic refraction, receiver functions and surface wave tomography. Tectonophysics 609, 82-96.

Assumpcao, M., James, D., Snoke, A., 2002. Crustal thicknesses in SE Brazilian Shield by receiver function analysis: Implications for isostatic compensation. J. Geophys. Res. 107.

Auer, L., Becker, T.W., Boschi, L., Schmerr, N., 2015. Thermal structure, radial anisotropy, and dynamics of oceanic boundary layers. Geophys Res Lett 42, 9740-9749.

Baba, K., Chave, A.D., Evans, R.L., Hirth, G., Mackie, R.L., 2006. Mantle dynamics beneath the East Pacific Rise at 17 degrees S: Insights from the Mantle Electromagnetic and Tomography (MELT) experiment. J. Geophys. Res. 111.

Bagley, B., Revenaugh, J., 2008. Upper mantle seismic shear discontinuities of the Pacific. J. Geophys. Res. 113.

Barrell, J., 1914. The Strength of the Earth's Crust. The Journal of Geology 22, 537-555.

Bedard, J.H., 2006. A catalytic delamination-driven model for coupled genesis of Archaean crust and sub-continental lithospheric mantle. Geochim Cosmochim Ac 70, 1188-1214.

Beghein, C., Yuan, K.Q., Schmerr, N., Xing, Z., 2014. Changes in Seismic Anisotropy Shed Light on the Nature of the Gutenberg Discontinuity. Science 343, 1237-1240.

Behn, M.D., Hirth, G., Elsenbeck, J.R., 2009. Implications of grain size evolution on the seismic structure of the oceanic upper mantle. Earth Planet. Sci. Lett. 282, 178-189.

Bhattacharyya, J., Masters, G., Shearer, P., 1996. Global lateral variations of shear wave attenuation in the upper mantle. J. Geophys. Res. 101, 22273.

Bird, P., 2003. An updated digital model of plate boundaries. Geochemistry Geophysics Geosystems 4.

Bostock, M.G., 1998. Mantle stratigraphy and evolution of the Slave province. J. Geophys. Res. 103, 21183-21200.

Bostock, M.G., 1999. Seismic imaging of lithospheric discontinuities and continental evolution. Lithos 48, 1-16.

Boyd, F.R., 1984. Siberian Geotherm Based on Iherzolite Xenoliths from the Udachnaya Kimberlite, Ussr. Geology 12, 528-530.

Boyd, F.R., 1989. Compositional Distinction between Oceanic and Cratonic Lithosphere. Earth Planet. Sci. Lett. 96, 15-26.

Boyd, F.R., Gurney, J.J., 1986. Diamonds and the African Lithosphere. Science 232, 472-477.

Boyd, F.R., Gurney, J.J., Richardson, S.H., 1985. Evidence for a 150-200-Km Thick Archean Lithosphere from Diamond Inclusion Thermobarometry. Nature 315, 387-389.

Boyd, F.R., Pokhilenko, N.P., Pearson, D.G., Mertzman, S.A., Sobolev, N.V., Finger, L.W., 1997. Composition of the Siberian cratonic mantle: evidence from Udachnaya peridotite xenoliths. Contrib Mineral Petr 128, 228-246.

Burgos, G., Montagner, J.P., Beucler, E., Capdeville, Y., Mocquet, A., Drilleau, M., 2014. Oceanic lithosphere-asthenosphere boundary from surface wave dispersion data. J. Geophys. Res. 119, 1079-1093.

Burov, E., 2011. Lithosphere, Mechanical Properties, in: Gupta, H.K. (Ed.), Encyclopedia of Solid Earth Geophysics. Springer Netherlands, Dordrecht, pp. 693-701.

Burov, E.B., Diament, M., 1995. The effective elastic thickness (T e) of continental lithosphere: What does it really mean? J. Geophys. Res. 100, 3905-3927.

Calvert, A.J., Sawyer, E.W., Davis, W.J., Ludden, J.N., 1995. Archean Subduction Inferred from Seismic Images of a Mantle Suture in the Superior Province. Nature 375, 670-674.

Cammarano, F., Romanowicz, B., 2007. Insights into the nature of the transition zone from physically constrained inversion of long-period seismic data. P Natl Acad Sci USA 104, 9139-9144.

Chambers, K., Deuss, A., Woodhouse, J.H., 2005. Reflectivity of the 410-km discontinuity from PP and SS precursors. J. Geophys. Res. 110.

Chandler, M.T., Wessel, P., Sager, W.W., 2013. Analysis of Ontong Java Plateau palaeolatitudes: evidence for large-scale rotation since 123 Ma? Geophys. J. Int. 194, 18-29.

Cherepanova, Y., Artemieva, I.M., Thybo, H., Chemia, Z., 2013. Crustal structure of the Siberian craton and the West Siberian basin: An appraisal of existing seismic data. Tectonophysics 609, 154-183.

Coffin, M.F., Eldholm, O., 1994. Large Igneous Provinces - Crustal Structure, Dimensions, and External Consequences. Rev. Geophys. 32, 1-36.

Conder, J.A., Forsyth, D.W., Parmentier, E.M., 2002. Asthenospheric flow and asymmetry of the East Pacific Rise, MELT area. J. Geophys. Res. 107.

Condie, K.C., 1997. Plate Tectonics. Elsevier Science. 9780080514093

Cooper, C.M., Lenardic, A., Moresi, L., 2004. The thermal structure of stable continental lithosphere within a dynamic mantle. Earth Planet. Sci. Lett. 222, 807-817.

Cooper, P.A., Taylor, B., 1985. Polarity Reversal in the Solomon-Islands Arc. Nature 314, 428-430.

Covellone, B.M., Savage, B., Shen, Y., 2015. Seismic wave speed structure of the Ontong Java Plateau. Earth Planet. Sci. Lett. 420, 140-150.

Dalton, C.A., Ekstrom, G., Dziewonski, A.M., 2008. The global attenuation structure of the upper mantle. J. Geophys. Res. 113.

Dalton, C.A., Ekstrom, G., Dziewonski, A.M., 2009. Global seismological shear velocity and attenuation: A comparison with experimental observations. Earth Planet. Sci. Lett. 284, 65-75.

Daly, R.A., 1940. Strength and structure of the earth. Prentice-Hall, inc., New York.

Davy, B., Hoernle, K., Werner, R., 2008. Hikurangi Plateau: Crustal structure, rifted formation, and Gondwana subduction history. Geochemistry Geophysics Geosystems 9.

Davy, B., Wood, R., 1994. Gravity and Magnetic Modeling of the Hikurangi Plateau. Mar Geol 118, 139-151.

Debayle, E., Dubuffet, F., Durand, S., 2016. An automatically updated S-wavemodel of the upper mantle and the depth extent of azimuthal anisotropy. Geophys Res Lett 43, 674-682.

Debayle, E., Kennett, B., Priestley, K., 2005. Global azimuthal seismic anisotropy and the unique plate-motion deformation of Australia. Nature 433, 509-512.

Debayle, E., Kennett, B.L.N., 2000. Anisotropy in the Australasian upper mantle from Love and Rayleigh waveform inversion. Earth Planet. Sci. Lett. 184, 339-351.

Deuss, A., 2009. Global Observations of Mantle Discontinuities Using SS and PP Precursors. Surveys in Geophysics 30, 301-326.

Deuss, A., Woodhouse, J.H., 2002. A systematic search for mantle discontinuities using SS-precursors. Geophys Res Lett 29.

Di Leo, J.F., Wookey, J., Kendall, J.M., Selby, N.D., 2015. Probing the edge of the West African Craton: A first seismic glimpse from Niger. Geophys Res Lett 42, 1694-1700.

Draper, N.R., Smith, H., 1998. Applied Regression Analysis, 3rd ed. John Wiley & Sons, Inc. 0-471-17082-8

Dugda, M.T., Nyblade, A.A., Julia, J., Langston, C.A., Ammon, C.J., Simiyu, S., 2005. Crustal structure in Ethiopia and Kenya from receiver function analysis: Implications for rift development in eastern Africa. J. Geophys. Res. 110.

Dumoulin, C., Doin, M.P., Fleitout, L., 2001. Numerical simulations of the cooling of an oceanic lithosphere above a convective mantle. Phys. Earth Planet. Inter. 125, 45-64.

Dziewonski, A.M., Anderson, D.L., 1981. Preliminary Reference Earth Model. Phys. Earth Planet. Inter. 25, 297-356.

Eaton, D.W., Darbyshire, F., Evans, R.L., Grutter, H., Jones, A.G., Yuan, X.H., 2009. The elusive lithosphere-asthenosphere boundary (LAB) beneath cratons. Lithos 109, 1-22.

Efron, B., Tibshirani, R., 1986. Bootstrap methods for standard errors, confidence intervals, and other measures of statistical accuracy. Statistical Science 1, 23.

Evans, R.L., Hirth, G., Baba, K., Forsyth, D., Chave, A., Mackie, R., 2005. Geophysical evidence from the MELT area for compositional controls on oceanic plates. Nature 437, 249-252.

Evans, R.L., Tarits, P., Chave, A.D., White, A., Heinson, G., Filloux, J.H., Toh, H., Seama, N., Utada, H., Booker, J.R., Unsworth, M.J., 1999. Asymmetric electrical structure in the mantle beneath the East Pacific rise at 17 degrees S. Science 286, 752-756.

Faul, U.H., 1997. Permeability of partially molten upper mantle rocks from experiments and percolation theory. J. Geophys. Res. 102, 10299-10311.

Fischer, K.M., Ford, H.A., Abt, D.L., Rychert, C.A., 2010. The Lithosphere-Asthenosphere Boundary. Annu. Rev. Earth Planet. Sci. 38, 551-575.

Flanagan, M.P., Shearer, P.M., 1998. Topography on the 410-km seismic velocity discontinuity near subduction zones from stacking of sS, sP, and pP precursors. J. Geophys. Res. 103, 21165-21182.

Ford, H.A., Fischer, K.M., Abt, D.L., Rychert, C.A., Elkins-Tanton, L.T., 2010. The lithosphere-asthenosphere boundary and cratonic lithospheric layering beneath Australia from Sp wave imaging. Earth Planet. Sci. Lett. 300, 299-310.

Forsyth, D.W., 1992. Geophysical Constraints on Mantle Flow and Melt Generation beneath Midocean Ridges. Geoph Monog Series 71, 1-65.

Foster, K., Dueker, K., Schmandt, B., Yuan, H., 2014. A sharp cratonic lithosphere-asthenosphere boundary beneath the American Midwest and its relation to mantle flow. Earth Planet. Sci. Lett. 402, 82-89.

Frederiksen, A.W., Bostock, M.G., Cassidy, J.F., 2001. S-wave velocity structure of the Canadian upper mantle. Phys. Earth Planet. Inter. 124, 175-191.

French, S., Lekic, V., Romanowicz, B., 2013. Waveform Tomography Reveals Channeled Flow at the Base of the Oceanic Asthenosphere. Science 342, 227-230.

Frisch, W., Meschede, M., Blakey, R.C., 2010. Plate Tectonics: Continental Drift and Mountain Building. Springer Berlin Heidelberg. 9783540765042

Fukao, Y., Obayashi, M., 2013. Subducted slabs stagnant above, penetrating through, and trapped below the 660 km discontinuity. J. Geophys. Res. 118, 5920-5938.

Furumoto, A.S., Webb, J.P., Odegard, M.E., Hussong, D.M., 1976. Seismic studies on the Ontong Java Plateau, 1970. Tectonophysics 34, 71-90.

Gaherty, J.B., 2004. A surface wave analysis of seismic anisotropy beneath eastern North America. Geophys. J. Int. 158, 1053-1066.

Gaherty, J.B., Jordan, T.H., 1995. Lehmann Discontinuity as the Base of an Anisotropic Layer beneath Continents. Science 268, 1468-1471.

Gaherty, J.B., Kato, M., Jordan, T.H., 1999. Seismological structure of the upper mantle: a regional comparison of seismic layering. Phys. Earth Planet. Inter. 110, 21-41.

Geissler, W.H., Sodoudi, F., Kind, R., 2010. Thickness of the central and eastern European lithosphere as seen by S receiver functions. Geophys. J. Int. 181, 604-634.

Gladczenko, T.P., Coffin, M.F., Eldholm, O., 1997. Crustal structure of the Ontong Java Plateau: Modeling of new gravity and existing seismic data. J. Geophys. Res. 102, 22711-22729.

Gomer, B.M., Okal, E.A., 2003. Multiple-ScS probing of the Ontong-Java Plateau. Phys. Earth Planet. Inter. 138, 317-331.

Griffiths, R.W., Campbell, I.H., 1990. Stirring and Structure in Mantle Starting Plumes. Earth Planet. Sci. Lett. 99, 66-78.

Gross, D., Shortle, J.F., Thompson, J.M., Harris, C.M., 2008. Fundamentals of Queueing Theory, 4th ed. John Wiley & Sons, Inc., Hoboken, New Jersey. 978-0-471-79127-0

Grutter, H., Moore, R., 2003. Pyroxene Geotherms Revisited — an Empirical Approach Based on Canadian Xenoliths. Extended abstract, Eighth International Kimberlite Conference, 272 (CD-ROM).

Gu, Y.J., Dziewonski, A.M., 2002. Global variability of transition zone thickness. J. Geophys. Res. 107.

Gu, Y.J., Webb, S.C., Lerner-Lam, A., Gaherty, J.B., 2005. Upper mantle structure beneath the eastern Pacific Ocean ridges. J. Geophys. Res. 110.

Gung, Y.C., Panning, M., Romanowicz, B., 2003. Global anisotropy and the thickness of continents. Nature 422, 707-711.

Hacker, B.R., Abers, G.A., 2004. Subduction Factory 3: An Excel worksheet and macro for calculating the densities, seismic wave speeds, and H2O contents of minerals and rocks at pressure and temperature. Geochemistry Geophysics Geosystems 5.

Hales, A.L., 1969. A Seismic Discontinuity in the Lithosphere. Earth Planet. Sci. Lett. 7, 3.

Hammond, W.C., Humphreys, E.D., 2000. Upper mantle seismic wave velocity: Effects of realistic partial melt geometries. J. Geophys. Res. 105, 10975-10986.

Hansen, S.E., Nyblade, A.A., Julia, J., Dirks, P.H.G.M., Durrheim, R.J., 2009. Upper-mantle low-velocity zone structure beneath the Kaapvaal craton from S-wave receiver functions. Geophys. J. Int. 178, 1021-1027.

Harmon, N., Blackman, D.K., 2010. Effects of plate boundary geometry and kinematics on mantle melting beneath the back-arc spreading centers along the Lau Basin. Earth Planet. Sci. Lett. 298, 334-346.

Harmon, N., Forsyth, D.W., Weeraratne, D.S., 2009. Thickening of young Pacific lithosphere from high-resolution Rayleigh wave tomography: A test of the conductive cooling model. Earth Planet. Sci. Lett. 278, 96-106.

Harmon, N., Rychert, C.A., Becker, T.W., 2016. Constraints on the radially anisotropic component of seismic discontinuities at 60-100 km depth, American Geophysical Union Fall Meeting, San Francisco.

Havlin, C., Parmentier, E.M., Hirth, G., 2013. Dike propagation driven by melt accumulation at the lithosphere-asthenosphere boundary. Earth Planet. Sci. Lett. 376, 20-28.

Heit, B., Sodoudi, F., Yuan, X., Bianchi, M., Kind, R., 2007. An S receiver function analysis of the lithospheric structure in South America. Geophys Res Lett 34.

Heit, B., Yuan, X., Bianchi, M., Kind, R., Gossler, J., 2010. Study of the lithospheric and upper-mantle discontinuities beneath eastern Asia by SS precursors. Geophys. J. Int. 183, 252-266.

Hills, D.V., Haggerty, S.E., 1989. Petrochemistry of Eclogites from the Koidu Kimberlite Complex, Sierra-Leone. Contrib Mineral Petr 103, 397-422.

Hirschmann, M.M., 2000. Mantle solidus: Experimental constraints and the effects of peridotite composition. Geochemistry, Geophysics, Geosystems 1, n/a-n/a.

Hirschmann, M.M., 2010. Partial melt in the oceanic low velocity zone. Phys. Earth Planet. Inter. 179, 60-71.

Hirth, G., Evans, R.L., Chave, A.D., 2000. Comparison of continental and oceanic mantle electrical conductivity: Is the Archean lithosphere dry? Geochemistry Geophysics Geosystems 1.

Hirth, G., Kohlstedt, D.L., 1995. Experimental Constraints on the Dynamics of the Partially Molten Upper-Mantle - Deformation in the Diffusion Creep Regime. J. Geophys. Res. 100, 1981-2001.

Hirth, G., Kohlstedt, D.L., 1996. Water in the oceanic upper mantle: Implications for rheology, melt extraction and the evolution of the lithosphere. Earth Planet. Sci. Lett. 144, 93-108.

Hooke, R., Jeeves, T.A., 1961. `` Direct Search'' Solution of Numerical and Statistical Problems. J. ACM 8, 212-229.

Hosmer, D.W., Hosmer, T., leCessie, S., Lemeshow, S., 1997. A comparison of goodness-of-fit tests for the logistic regression model. Stat Med 16, 965-980.

Houser, C., Masters, G., Flanagan, M., Shearer, P., 2008. Determination and analysis of long-wavelength transition zone structure using SS precursors. Geophys. J. Int. 174, 178-194.

Huang, J.S., Zhong, S.J., 2005. Sublithospheric small-scale convection and its implications for the residual topography at old ocean basins and the plate model. J. Geophys. Res. 110.

Ito, G., Clift, P.D., 1998. Subsidence and growth of Pacific Cretaceous plateaus. Earth Planet. Sci. Lett. 161, 85-100.

Ito, G., Taira, A., 2000. Compensation of the Ontong Java Plateau by surface and subsurface loading. J. Geophys. Res. 105, 11171-11183.

Jackson, I., Faul, U.H., 2010. Grainsize-sensitive viscoelastic relaxation in olivine: Towards a robust laboratory-based model for seismological application. Phys. Earth Planet. Inter. 183, 151-163.

Jaupart, C., Mareschal, J.-C., 2015. Heat Flow and Thermal Structure of the Lithosphere, in: Schubert, G. (Ed.), Treatise on Geophysics, 2 ed. Elsevier, p. 5604.

Jha, K., Parmentier, E.M., Morgan, J.P., 1994. The Role of Mantle-Depletion and Melt-Retention Buoyancy in Spreading-Center Segmentation. Earth Planet. Sci. Lett. 125, 221-234.

Jones, A.G., 1999. Imaging the continental upper mantle using electromagnetic methods. Lithos 48, 57-80.

Jones, A.G., Ferguson, I.J., Chave, A.D., Evans, R.L., McNeice, G.W., 2001. Electric lithosphere of the Slave craton. Geology 29, 423-426.

Jordan, T.H., 1975. The Continental Tectosphere. Rev. Geophys. 13, 12.

Jordan, T.H., 1978. Composition and development of the continental tectosphere. Nature 274, 5.

Jordan, T.H., 1988. Structure and Formation of the Continental Tectosphere. J. Petrol., 28.

Karato, S., 1987. Scanning Electron-Microscope Observation of Dislocations in Olivine. Phys Chem Miner 14, 245-248.

Karato, S., Jung, H., 1998. Water, partial melting and the origin of the seismic low velocity and high attenuation zone in the upper mantle. Earth Planet. Sci. Lett. 157, 193-207.

Karato, S., Wu, P., 1993. Rheology of the Upper Mantle - a Synthesis. Science 260, 771-778.

Karato, S.I., 2012. On the origin of the asthenosphere. Earth Planet. Sci. Lett. 321, 95-103.

Karato, S.I., Olugboji, T., Park, J., 2015. Mechanisms and geologic significance of the mid-lithosphere discontinuity in the continents. Nat Geosci 8, 509-514.

Katz, R.F., 2010. Porosity-driven convection and asymmetry beneath mid-ocean ridges. Geochemistry Geophysics Geosystems 11.

Katz, R.F., Spiegelman, M., Langmuir, C.H., 2003. A new parameterization of hydrous mantle melting. Geochemistry Geophysics Geosystems 4.

Kawakatsu, H., Kumar, P., Takei, Y., Shinohara, M., Kanazawa, T., Araki, E., Suyehiro, K., 2009. Seismic evidence for sharp lithosphere-asthenosphere boundaries of oceanic plates. Science 324, 499-502.

Kennedy, C.S., Kennedy, G.C., 1976. The equilibrium boundary between graphite and diamond. J. Geophys. Res. 81, 2467-2470.

Kennett, B.L.N., Engdahl, E.R., 1991. Traveltimes for global earthquake location and phase identification. Geophys. J. Int. 105, 429-465.

King, S.D., 2005. Archean cratons and mantle dynamics. Earth Planet. Sci. Lett. 234, 1-14.

King, S.D., Anderson, D.L., 1998. Edge-driven convection. Earth Planet. Sci. Lett. 160, 289-296.

Kirkpatrick, S., Gelatt, C.D., Vecchi, M.P., 1983. Optimization by Simulated Annealing. Science 220, 671-680.

Kjarsgaard, J., Peterson, T.D., 1992. Kimberlite-derived ultramafic xenoliths from the diamond stability field: a new Cretaceous geotherm for Somerset Island, Northwest Territories. Current Research, Geological Survey of Canada 92-1B, 6.

Klosko, E.R., Russo, R.M., Okal, E.A., Richardson, W.P., 2001. Evidence for a rheologically strong chemical mantle root beneath the Ontong-Java Plateau. Earth Planet. Sci. Lett. 186, 347-361.

Kohlstedt, D.L., Evans, B., Mackwell, S.J., 1995. Strength of the lithosphere: Constraints imposed by laboratory experiments. J. Geophys. Res. 100, 17587-17602.

Kopylova, M.G., Russell, J.K., Cookenboo, H., 1999. Petrology of peridotite and pyroxenite xenoliths from the Jericho kimberlite: Implications for the thermal state of the mantle beneath the Slave craton, Northern Canada. J. Petrol. 40, 79-104.

Korenaga, J., 2015. Seafloor topography and the thermal budget of Earth. Geological Society of America Special Papers 514, 167-185.

Korenaga, J., Jordan, T.H., 2002. On the state of sublithospheric upper mantle beneath a supercontinent. Geophys. J. Int. 149, 179-189.

Korenaga, T., Korenaga, J., 2008. Subsidence of normal oceanic lithosphere, apparent thermal expansivity, and seafloor flattening. Earth Planet. Sci. Lett. 268, 41-51.

Kumar, P., Kawakatsu, H., 2011. Imaging the seismic lithosphere-asthenosphere boundary of the oceanic plate. Geochemistry, Geophysics, Geosystems 12, n/a-n/a.

Kumar, P., Kind, R., Yuan, X.H., Mechie, J., 2012a. USArray Receiver Function Images of the Lithosphere-Asthenosphere Boundary. Seismol Res Lett 83, 486-491.

Kumar, P., Kumar, M.R., Srijayanthi, G., Arora, K., Srinagesh, D., Chadha, R.K., Sen, M.K., 2013. Imaging the lithosphere-asthenosphere boundary of the Indian plate using converted wave techniques. J. Geophys. Res. 118, 5307-5319.

Kumar, P., Yuan, X., Kind, R., Mechie, J., 2012b. The lithosphere-asthenosphere boundary observed with USArray receiver functions. Solid Earth 3, 149-159.

Kumar, P., Yuan, X.H., Kind, R., Ni, J., 2006. Imaging the colliding Indian and Asian lithospheric plates beneath Tibet. J. Geophys. Res. 111.

Kumar, P., Yuan, X.H., Kumar, M.R., Kind, R., Li, X.Q., Chadha, R.K., 2007. The rapid drift of the Indian tectonic plate. Nature 449, 894-897.

Kustowski, B., Ekstrom, G., Dziewonski, A.M., 2008. Anisotropic shear-wave velocity structure of the Earth's mantle: A global model. J. Geophys. Res. 113.

Laske, G., Masters, G., Ma, Z., Pasyanos, M., 2012. CRUST1.0: An updated global model of Earth's crust, European Geoscience Union. Geophysical Research Abstracts, Vienna, Austria.

Lawrence, J.F., Shearer, P.M., 2008. Imaging mantle transition zone thickness with SdS-SS finite-frequency sensitivity kernels. Geophys. J. Int. 174, 143-158.

Lee, C.T.A., 2003. Compositional variation of density and seismic velocities in natural peridotites at STP conditions: Implications for seismic imaging of compositional heterogeneities in the upper mantle. J. Geophys. Res. 108.

Lee, C.T.A., Lenardic, A., Cooper, C.M., Niu, F.L., Levander, A., 2005. The role of chemical boundary layers in regulating the thickness of continental and oceanic thermal boundary layers. Earth Planet. Sci. Lett. 230, 379-395.

Lee, C.T.A., Luffi, P., Chin, E.J., 2011. Building and Destroying Continental Mantle. Annu Rev Earth Pl Sc 39, 59-90.

Lehmann, I., 1955. The times of P and S in Northeastern America. Annals of Geophysics 8, 20.

Li, A.B., Burke, K., 2006. Upper mantle structure of southern Africa from Rayleigh wave tomography. J. Geophys. Res. 111.

Li, X.Q., Kind, R., Yuan, X.H., Wolbern, I., Hanka, W., 2004. Rejuvenation of the lithosphere by the Hawaiian plume. Nature 427, 827-829.

Lin, P.-Y.P., Gaherty, J.B., Jin, G., Collins, J.A., Lizarralde, D., Evans, R.L., Hirth, G., 2016. High-resolution seismic constraints on flow dynamics in the oceanic asthenosphere. Nature advance online publication.

Lizarralde, D., Chave, A., Hirth, G., Schultz, A., 1995. Northeastern Pacific mantle conductivity profile from long-period magnetotelluric sounding using Hawaii-to-California submarine cable data. J. Geophys. Res. 100, 17837-17854.

Maggi, A., Debayle, E., Priestley, K., Barruol, G., 2006. Azimuthal anisotropy of the Pacific region. Earth Planet. Sci. Lett. 250, 53-71.

Mann, P., Taira, A., 2004. Global tectonic significance of the Solomon Islands and Ontong Java Plateau convergent zone. Tectonophysics 389, 137-190.

Mareschal, J.C., Jaupart, C., 2013. Radiogenic heat production, thermal regime and evolution of continental crust. Tectonophysics 609, 524-534.

Masters, G., Johnson, S., Laske, G., Bolton, H., 1996. A shear-velocity model of the mantle. Philos T R Soc A 354, 1385-1410.

McNutt, M.K., 1984. Lithospheric flexure and thermal anomalies. J. Geophys. Res. 89, 11180-11194.

Megnin, C., Romanowicz, B., 2000. The three-dimensional shear velocity structure of the mantle from the inversion of body, surface and higher-mode waveforms. Geophys. J. Int. 143, 709-728.

Miura, S., Suyehiro, K., Shinohara, M., Takahashi, N., Araki, E., Taira, A., 2004. Seismological structure and implications of collision between the

Ontong Java Plateau and Solomon Island Arc from ocean bottom seismometer–airgun data. Tectonophysics 389, 191-220.

Moorkamp, M., Jones, A.G., Fishwick, S., 2010. Joint inversion of receiver functions, surface wave dispersion, and magnetotelluric data. J. Geophys. Res. 115.

Müller, R.D., Dutkiewicz, A., Seton, M., Gaina, C., 2013. Seawater chemistry driven by supercontinent assembly, breakup, and dispersal. Geology 41, 907-910.

Nair, S.K., Gao, S.S., Liu, K.H., Silver, P.G., 2006. Southern African crustal evolution and composition: Constraints from receiver function studies. J. Geophys. Res. 111.

Nataf, H.C., Ricard, Y., 1996. 3SMAC: An a priori tomographic model of the upper mantle based on geophysical modeling. Phys. Earth Planet. Inter. 95, 101-122.

Nelder, J.A., Mead, R., 1965. A Simplex Method for Function Minimization. The Computer Journal 7, 308-313.

Nettles, M., Dziewonski, A.M., 2008. Radially anisotropic shear velocity structure of the upper mantle globally and beneath North America. J. Geophys. Res. 113.

Nguuri, T.K., Gore, J., James, D.E., Webb, S.J., Wright, C., Zengeni, T.G., Gwavava, O., Snoke, J.A., Grp, K.S., 2001. Crustal structure beneath southern Africa and its implications for the formation and evolution of the Kaapvaal and Zimbabwe cratons. Geophys Res Lett 28, 2501-2504.

Nicolas, A., Christensen, N.I., 1987. Formation of Anisotropy in Upper Mantle Peridotites - A Review, Composition, Structure and Dynamics of the Lithosphere-Asthenosphere System. American Geophysical Union, pp. 111-123.

Nimis, P., Grutter, H., 2010. Internally consistent geothermometers for garnet peridotites and pyroxenites. Contrib Mineral Petr 159, 411-427.

Nishimura, C.E., Forsyth, D.W., 1989. The anisotropic structure of the upper mantle in the Pacific. Geophys. J. Int. 96, 24.

Niu, F.L., Solomon, S.C., Silver, P.G., Suetsugu, D., Inoue, H., 2002. Mantle transition-zone structure beneath the South Pacific Superswell and evidence for a mantle plume underlying the Society hotspot. Earth Planet. Sci. Lett. 198, 371-380.

Olugboji, T.M., Karato, S., Park, J., 2013. Structures of the oceanic lithosphere-asthenosphere boundary: Mineral-physics modeling and seismological signatures. Geochemistry Geophysics Geosystems 14, 880-901.

Olugboji, T.M., Park, J., Karato, S.-i., Shinohara, M., 2016. Nature of the seismic lithosphere-asthenosphere boundary within normal oceanic mantle from high-resolution receiver functions. Geochemistry, Geophysics, Geosystems 17, 1265-1282.

Oreshin, S., Vinnik, L., Makeyeva, L., Kosarev, G., Kind, R., Wentzel, F., 2002. Combined analysis of SKS splitting and regional P traveltimes in Siberia. Geophys. J. Int. 151, 393-402.

Owens, T.J., Crotwell, H.P., Groves, C., Oliver-Paul, P., 2004. SOD: Standing order for data. Seismol Res Lett 75, 515-520.

Parsons, B., Mckenzie, D., 1978. Mantle Convection and Thermal Structure of Plates. J. Geophys. Res. 83, 4485-4496.

Parsons, B., Sclater, J.G., 1977. Analysis of Variation of Ocean-Floor Bathymetry and Heat-Flow with Age. J. Geophys. Res. 82, 803-827.

Pearson, D.G., Shirey, S.B., Carlson, R.W., Boyd, F.R., Pokhilenko, N.P., Shimizu, N., 1995. Re-Os, Sm-Nd, and Rb-Sr Isotope Evidence for Thick Archean Lithospheric Mantle beneath the Siberian Craton Modified by Multistage Metasomatism. Geochim Cosmochim Ac 59, 959-977.

Pedersen, H.A., Fishwick, S., Snyder, D.B., 2009. A comparison of cratonic roots through consistent analysis of seismic surface waves. Lithos 109, 81-95.

Pollack, H.N., 1986. Cratonization and Thermal Evolution of the Mantle. Earth Planet. Sci. Lett. 80, 175-182.

Price, K.V., Storn, R.M., Lampinen, J.A., 2005. Differential Evolution: A Practical Approach to Global Optimization Springer, Heidelberg, Germany. 978-3-540-31306-9

Rechenberg, I., 1973. Evolutionsstrategie: Optimierung technischer Systeme und Prinzipien der biologischen Evolution. Frommann-Holzboog, Stuttgart.

Regan, J., Anderson, D.L., 1984. Anisotropic Models of the Upper Mantle. Phys. Earth Planet. Inter. 35, 227-263.

Revenaugh, J., Jordan, T.H., 1991. Mantle Layering from Scs Reverberations .3. The Upper Mantle. J. Geophys. Res. 96, 19781-19810.

Richardson, W.P., Okal, E.A., Van der Lee, S., 2000. Rayleigh-wave tomography of the Ontong-Java Plateau. Phys. Earth Planet. Inter. 118, 29-51.

Ritsema, J., van Heijst, H.J., Woodhouse, J.H., 1999. Complex shear wave velocity structure imaged beneath Africa and Iceland. Science 286, 1925-1928.

Ritzwoller, M.H., Shapiro, N.M., Zhong, S.J., 2004. Cooling history of the Pacific lithosphere. Earth Planet. Sci. Lett. 226, 69-84.

Rudnick, R.L., McDonough, W.F., O'Connell, R.J., 1998. Thermal structure, thickness and composition of continental lithosphere. Chem Geol 145, 395-411.

Rychert, C.A., 2015. The slippery base of a tectonic plate. Nature 518, 39-40.

Rychert, C.A., Fischer, K.M., Abers, G.A., Plank, T., Syracuse, E., Protti, J.M., Gonzalez, V., Strauch, W., 2008. Strong along-arc variations in attenuation in the mantle wedge beneath Costa Rica and Nicaragua. Geochemistry Geophysics Geosystems 9.

Rychert, C.A., Fischer, K.M., Rondenay, S., 2005. A sharp lithosphere-asthenosphere boundary imaged beneath eastern North America. Nature 436, 542-545.

Rychert, C.A., Harmon, N., 2016. Stacked P-to-S and S-to-P receiver functions determination of crustal thickness, V-p, and V-s: The H-V stacking method. Geophys Res Lett 43, 1487-1494.

Rychert, C.A., Harmon, N., 2017. Constraints on the anisotropic contributions to velocity discontinuities at ~60 km depth beneath the Pacific. Geochemistry Geophysics Geosystems (submitted).

Rychert, C.A., Harmon, N., Ebinger, C., 2014a. Receiver function imaging of lithospheric structure and the onset of melting beneath the Galapagos Archipelago. Earth Planet. Sci. Lett. 388, 156-165.

Rychert, C.A., Harmon, N., Schmerr, N., 2014b. Synthetic waveform modelling of SS precursors from anisotropic upper-mantle discontinuities. Geophys. J. Int. 196, 1694-1705.

Rychert, C.A., Laske, G., Harmon, N., Shearer, P.M., 2013. Seismic imaging of melt in a displaced Hawaiian plume. Nat Geosci 6, 657-660.

Rychert, C.A., Rondenay, S., Fischer, K.M., 2007. P-to-S and S-to-P imaging of a sharp lithosphere-asthenosphere boundary beneath eastern North America. J. Geophys. Res. 112.

Rychert, C.A., Schmerr, N., Harmon, N., 2012. The Pacific lithosphere-asthenosphere boundary: Seismic imaging and anisotropic constraints from SS waveforms. Geochemistry Geophysics Geosystems 13.

Rychert, C.A., Shearer, P.M., 2009. A Global View of the Lithosphere-Asthenosphere Boundary. Science 324, 495-498.

Rychert, C.A., Shearer, P.M., 2010. Resolving crustal thickness using SS waveform stacks. Geophys. J. Int. 180, 1128-1137.

Rychert, C.A., Shearer, P.M., 2011. Imaging the lithosphere-asthenosphere boundary beneath the Pacific using SS waveform modeling. J. Geophys. Res. 116.

Rychert, C.A., Shearer, P.M., Fischer, K.M., 2010. Scattered wave imaging of the lithosphere–asthenosphere boundary. Lithos 120, 173-185.

Sakamaki, T., Suzuki, A., Ohtani, E., Terasaki, H., Urakawa, S., Katayama, Y., Funakoshi, K., Wang, Y.B., Hernlund, J.W., Ballmer, M.D., 2013. Ponded melt at the boundary between the lithosphere and asthenosphere. Nat Geosci 6, 1041-1044.

Saul, J., Kumar, M.R., Sarkar, D., 2000. Lithospheric and upper mantle structure of the Indian Shield, from teleseismic receiver functions. Geophys Res Lett 27, 2357-2360.

Savage, B., Silver, P.G., 2008. Evidence for a compositional boundary within the lithospheric mantle beneath the Kalahari craton from S receiver functions. Earth Planet. Sci. Lett. 272, 600-609.

Schaeffer, A.J., Lebedev, S., 2013. Global shear speed structure of the upper mantle and transition zone. Geophys. J. Int. 194, 417-449.

Schmerr, N., 2012. The Gutenberg Discontinuity: Melt at the Lithosphere-Asthenosphere Boundary. Science 335, 1480-1483.

Schmerr, N., Garnero, E., 2006. Investigation of upper mantle discontinuity structure beneath the central Pacific using SS precursors. J. Geophys. Res. 111.

Schmidberger, S.S., Francis, D., 1999. Nature of the mantle roots beneath the North American craton: mantle xenolith evidence from Somerset Island kimberlites. Lithos 48, 195-216.

Schubert, G., Froidevaux, C., Yuen, D.A., 1976. Oceanic lithosphere and asthenosphere: Thermal and mechanical structure. J. Geophys. Res. 81, 3525-3540.

Schutt, D.L., Lesher, C.E., 2006. Effects of melt depletion on the density and seismic velocity of garnet and spinel lherzolite. J. Geophys. Res. 111.

Schwefel, H.-P., 1994. Evolution and Optimum Seeking, 6th ed. Wiley-Blackwell, New York. 0471571482

Sebai, A., Stutzmann, E., Montagner, J.P., Sicilia, D., Beucler, E., 2006. Anisotropic structure of the African upper mantle from Rayleigh and Love wave tomography. Phys. Earth Planet. Inter. 155, 48-62.

Selway, K., Ford, H., Kelemen, P., 2015. The seismic mid-lithosphere discontinuity. Earth Planet. Sci. Lett. 414, 45-57.

Shearer, P.M., 1991a. Constraints on Upper Mantle Discontinuities from Observations of Long-Period Reflected and Converted Phases. J. Geophys. Res. 96, 36.

Shearer, P.M., 1991b. Imaging Global Body Wave Phases by Stacking Long-Period Seismograms. J. Geophys. Res. 96, 12.

Shearer, P.M., 1993. Global Mapping of Upper-Mantle Reflectors from Long-Period Ss Precursors. Geophys. J. Int. 115, 878-904.

Shearer, P.M., 1996. Transition zone velocity gradients and the 520-km discontinuity. J. Geophys. Res. 101, 14.

Shearer, P.M., 2009. Introduction to Seismology, 2 ed. Cambridge University Press. 9780521708425

Shearer, P.M., Flanagan, M.P., Hedlin, M.A.H., 1999. Experiments in migration processing of SS precursor data to image upper mantle discontinuity structure. J. Geophys. Res. 104, 7229-7242.

Shearer, P.M., Masters, T.G., 1992. Global Mapping of Topography on the 660-Km Discontinuity. Nature 355, 791-796.

Shirey, S.B., Richardson, S.H., 2011. Start of the Wilson Cycle at 3 Ga Shown by Diamonds from Subcontinental Mantle. Science 333, 434-436.

Sifre, D., Gardes, E., Massuyeau, M., Hashim, L., Hier-Majumder, S., Gaillard, F., 2014. Electrical conductivity during incipient melting in the oceanic low-velocity zone. Nature 509, 81-+.

Smith, W.H.F., Sandwell, D.T., 1997. Global sea floor topography from satellite altimetry and ship depth soundings. Science 277, 1956-1962.

Smolarkiewicz, P.K., 1984. A fully multidimensional positive definite advection transport algorithm with small implicit diffusion. Journal of Computational Physics 54, 325-362.

Snyder, D.B., 2008. Stacked uppermost mantle layers within the Slave craton of NW Canada as defined by anisotropic seismic discontinuities. Tectonics 27.

Sodoudi, F., Yuan, X.H., Kind, R., Lebedev, S., Adam, J.M.C., Kastle, E., Tilmann, F., 2013. Seismic evidence for stratification in composition and anisotropic fabric within the thick lithosphere of Kalahari Craton. Geochemistry Geophysics Geosystems 14, 5393-5412.

Sparks, D.W., Parmentier, E.M., 1991. Melt Extraction from the Mantle beneath Spreading Centers. Earth Planet. Sci. Lett. 105, 368-377.

Stein, C.A., Stein, S., 1992. A Model for the Global Variation in Oceanic Depth and Heat-Flow with Lithospheric Age. Nature 359, 123-129.

Stern, T.A., Henrys, S.A., Okaya, D., Louie, J.N., Savage, M.K., Lamb, S., Sato, H., Sutherland, R., Iwasaki, T., 2015. A seismic reflection image for the base of a tectonic plate. Nature 518, 85-88.

Storn, R., Price, K., 1997. Differential evolution - A simple and efficient heuristic for global optimization over continuous spaces. J Global Optim 11, 341-359.

Takeo, A., Nishida, K., Isse, T., Kawakatsu, H., Shiobara, H., Sugioka, H., Kanazawa, T., 2013. Radially anisotropic structure beneath the Shikoku Basin from broadband surface wave analysis of ocean bottom seismometer records. J. Geophys. Res. 118, 2878-2892.

Tan, Y., Helmberger, D.V., 2007. Trans-Pacific upper mantle shear velocity structure. J. Geophys. Res. 112.

Tappert, R., Foden, J., Muehlenbachs, K., Wills, K., 2011. Garnet Peridotite Xenoliths and Xenocrysts from the Monk Hill Kimberlite, South Australia: Insights into the Lithospheric Mantle beneath the Adelaide Fold Belt. J. Petrol. 52, 1965-1986.

Tappert, R., Stachel, T., Harris, J.W., Muehlenbachs, K., Brey, G.F., 2006. Placer diamonds from Brazil: Indicators of the composition of the Earth's mantle and the distance to their kimberlitic sources. Econ Geol 101, 453-470.

Taylor, B., 2006. The single largest oceanic plateau: Ontong Java-Manihiki-Hikurangi. Earth Planet. Sci. Lett. 241, 372-380.

Taylor, S.R., Mclennan, S.M., 1995. The Geochemical Evolution of the Continental-Crust. Rev. Geophys. 33, 241-265.

Tharimena, S., Rychert, C.A., Harmon, N., 2016. Seismic imaging of a mid-lithospheric discontinuity beneath Ontong Java Plateau. Earth Planet. Sci. Lett. 450, 9.

Thomson, A.R., Walter, M.J., Kohn, S.C., Brooker, R.A., 2016. Slab melting as a barrier to deep carbon subduction. Nature 529, 76-79.

Tommasi, A., Ishikawa, A., 2014. Microstructures, composition, and seismic properties of the Ontong Java Plateau mantle root. Geochemistry Geophysics Geosystems 15, 4547-4569.

Tychkov, N.S., Agashev, A.M., Malygina, E.V., Nikolenko, E.I., Pokhilenko, N.P., 2014. Thermal perturbations in the lithospheric mantle as evidenced from P-T equilibrium conditions of xenoliths from the Udachnaya kimberlite pipe. Dokl Earth Sci 454, 84-88.

Walker, R.J., Carlson, R.W., Shirey, S.B., Boyd, F.R., 1989. Os, Sr, Nd, and Pb isotope systematics of southern African peridotite xenoliths:

implications for the chemical evolution of subcontinental mantle. Geochim Cosmochim Ac 53, 12.

Walter, M.J., 1999. Melting residues of fertile peridotite and the origin of cratonic lithosphere. The Geochemical Society 6, 14.

Watts, A.B., 1978. Analysis of Isostasy in the Worlds Oceans .1. Hawaiian-Emperor Seamount Chain. J. Geophys. Res. 83, 5989-6004.

Watts, A.B., Bodine, J.H., Steckler, M.S., 1980. Observations of flexure and the state of stress in the oceanic lithosphere. J. Geophys. Res. 85, 6369-6376.

Weeraratne, D.S., Forsyth, D.W., Fischer, K.M., Nyblade, A.A., 2003. Evidence for an upper mantle plume beneath the Tanzanian craton from Rayleigh wave tomography. J. Geophys. Res. 108.

Weeraratne, D.S., Forsyth, D.W., Yang, Y., Webb, S.C., 2007. Rayleigh wave tomography beneath intraplate volcanic ridges in the South Pacific. J. Geophys. Res. 112, n/a-n/a.

White, R.S., 1988. The Earth's Crust and Lithosphere. J. Petrol. Special_Volume, 1-10.

Wittlinger, G., Farra, V., 2007. Converted waves reveal a thick and layered tectosphere beneath the Kalahari super-craton. Earth Planet. Sci. Lett. 254, 404-415.

Wolbern, I., Rumpker, G., Link, K., Sodoudi, F., 2012. Melt infiltration of the lower lithosphere beneath the Tanzania craton and the Albertine rift inferred from S receiver functions. Geochemistry Geophysics Geosystems 13.

Yuan, H., Romanowicz, B., 2010. Lithospheric layering in the North American craton. Nature 466, 1063-1068.